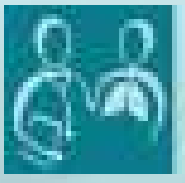

diagnostics

# Optical Diagnostics in Human Diseases

Edited by

Andrey Dunaev

Printed Edition of the Special Issue Published in *Diagnostics*

www.mdpi.com/journal/diagnostics

# Optical Diagnostics in Human Diseases

# Optical Diagnostics in Human Diseases

Editor

**Andrey Dunaev**

MDPI • Basel • Beijing • Wuhan • Barcelona • Belgrade • Manchester • Tokyo • Cluj • Tianjin

*Editor*
Andrey Dunaev
Orel State University
Russia

*Editorial Office*
MDPI
St. Alban-Anlage 66
4052 Basel, Switzerland

This is a reprint of articles from the Special Issue published online in the open access journal *Diagnostics* (ISSN 2075-4418) (available at: https://www.mdpi.com/journal/diagnostics/special_issues/Optical_Diagnostics_Diseases).

For citation purposes, cite each article independently as indicated on the article page online and as indicated below:

LastName, A.A.; LastName, B.B.; LastName, C.C. Article Title. *Journal Name* **Year**, *Volume Number*, Page Range.

**ISBN 978-3-0365-1617-2 (Hbk)**
**ISBN 978-3-0365-1618-9 (PDF)**

# Contents

# About the Editor

**Andrey Dunaev** received his M.Sc. and Ph.D. degrees in instrument engineering from Orel State University (Orel, Russia) in 1999 and 2002, respectively. From 2005 to 2011, he was Associate Professor at the Department of Instrument Engineering, Metrology and Certification. From 2011 to 2013, he was a Postdoctoral Researcher (Marie Curie Research Fellow) at Photonics and Nanoscience Group, University of Dundee (Dundee, UK). Since 2014, he has been the Head of Research and Development Center of Biomedical Photonics, Orel State University. He is the author of 5 books, more than 60 papers in peer-reviewed journals, and over 10 patents. His research interests include the development of multimodal optical non-invasive diagnostic methods for microcirculatory-tissue systems. He is the leader and executor of a number of projects supported by various Russian and international foundations (RSF, RFBR, and Academy of Finland, among others).

# Preface to "Optical Diagnostics in Human Diseases"

This Special Issue is devoted to the multidisciplinary studies in the field of optical non-invasive diagnostics for identifying and evaluating various diseases and pathological conditions. The purpose was to show the possibilities of using modern optical technologies in clinical practice as well as highlight the challenges, advantages, and unique aspects of optical diagnostic methods. This Special Issue is intended for medical physicists and doctors interested in the development and application of optical diagnostic techniques in medical research and practice.

**Andrey Dunaev**
*Editor*

*diagnostics*

MDPI

*Editorial*

# Optical Diagnostics in Human Diseases

**Andrey Dunaev**

Research and Development Center of Biomedical Photonics, Orel State University, 302026 Orel, Russia; dunaev@bmecenter.ru; Tel.: +7-4862-419806

**Keywords:** biophotonics; optics; spectroscopy; imaging; diagnostics

Light-based technologies provide unique opportunities for the diagnosis of various pathological disorders of biological tissues. With the advancement of modern science, they allow for the non-invasive identification of diseases at early stages. The optical technologies for obtaining information on the biochemical state and morphological structure of the investigated area are based on the assessment of light-tissue interaction (including laser radiation). For this purpose, a patient's tissues and organs are probed with optical radiation, and reflected (scattered, passed through the tissue, re-emitted as fluorescence, etc.) light is recorded. The range of optical technologies applications in clinical practice is considerably wide since the optical properties of biological tissues are subject to significant changes in the course of the disease. Optical non-invasive diagnostics uses many spectroscopic and imaging techniques, including near infrared spectrophotometry, fluorescence spectroscopy (FS) and imaging, optical coherence tomography (OCT), confocal spectroscopy, optoacoustic tomography, laser Doppler flowmetry (LDF), laser speckle contrast imaging, and a number of other methods. However, despite the rapid development of optical methods in medical diagnostics, it should be borne in mind that most of them have not yet become the gold standard in clinical practice. They are mostly used in scientific research or as an additional clarifying method, increasingly using the so-called multimodal approach, where one diagnostic technology combines various optical and other physical research methods, which makes it possible to provide early diagnosis of functional changes before clinical manifestations of the disease based on the measurement results. In addition, the wider introduction of these methods into routine clinical practice is hindered by the insufficient elaboration of their methodological and technical support. This Special Issue of Diagnostics is devoted to the ideas regarding a solution to these problems.

The Special Issue highlights the challenges, advantages, and unique aspects of optical diagnostic methods for identifying and evaluating various diseases and pathological conditions. Articles focus on certain technologies, diseases, and various aspects of spectroscopy and imaging application in clinical practice.

Several studies in this Special Issue present new information relevant to surgical procedures, especially in oncology and gynecology. Zherebtsov and colleagues, according to the multimodal approach, described the development of the technical implementation and assessment of machine learning methods' efficiency for the real-time diagnosis of tumors in hepatoduodenal organs by FS and LDF. This approach is aimed at improving the effectiveness of minimally invasive surgical operations by providing additional diagnostic information online [1]. Two articles are devoted to the topical problem of breast cancer's early detection, including during surgery. Gubarkova and colleagues compared two types of optical coherence tomography–cross-polarization OCT (CP OCT) and a novel type of compressional optical coherence elastography. They confirmed the high potential of OCT-based examinations for rapid and accurate diagnostics during breast conservation surgery [2]. Iida and colleagues conducted Monte Carlo simulation of shortwave-infrared (SWIR) fluorescence photon migration in voxelized media for breast cancer detection. The obtained results showed that it is possible to predict the presence of early-stage breast



**Citation:** Dunaev, A. Optical Diagnostics in Human Diseases. *Diagnostics* **2021**, *11*, 873. https://doi.org/10.3390/diagnostics11050873

Received: 30 March 2021
Accepted: 10 May 2021
Published: 12 May 2021

cancer with high spatial resolution using SWIR and the phantom model in which the optical parameters are implemented in the breast structure [3]. Huang and colleagues proposed a promising method based on the gray level co-occurrence matrix (GLCM) image processing model to achieve a rapid technique with a more reliable diagnostic performance for various types of chemoresistance for the cisplatin of human ovarian adenocarcinoma cells by feature extraction of GLCM [4].

The problem of chronic or recurrent episodic pain in the urethra with unchanged urinalysis, the absence of any other clinical manifestations or somatically explainable causes, is complex and ultimately remains unresolved since the exact pathogenetic mechanisms are not yet fully understood. The article by Streltsova and colleagues is dedicated to the targeted study of female urethral tissues (their elasticity and the condition of the epithelial and connective tissue layers) in urethral pain syndrome (UPS). The results showed that the introduction of new CP OCT technology in conjunction with transvaginal compression ultrasound will allow for in vivo verification of structural changes in lower urinary tract tissues at their architectonics level and will provide more information about basic elements of the UPS pathogenesis [5].

Several studies in this Special Issue are devoted to otolaryngology and dentistry. Bryanskaya and colleagues developed a basis for instrument implementation of digital diaphanoscopy technology for the diagnosis of maxillary sinus inflammatory diseases, taking into account the anatomical, age, and gender features of patients. Their approach may be promising as a screening method for assessing the condition of maxillary sinuses both in hospitals and medical institutions, as well as remotely in the absence of otolaryngologists and diagnosticians [6].

Timchenko and colleagues studied the changes in tooth tissues in periodontitis using Raman spectroscopy for early and rapid diagnosis and the correction of treatment. The obtained results are a prerequisite for creating a device for rapid in vivo assessment of periodontitis based on changes in tooth enamel spectral values [7].

Savchenko and colleagues developed an experimental optical device for diagnosing liver diseases. The main advantages of the proposed device are its usability and fast presentation of results in real time. The device is based on optical densitometry. To determine the functional reserves of the liver, the researchers used indocyanine green. It is a non-toxic dye that binds well to blood proteins and is delivered to the liver through the bloodstream. The dye was administered intravenously to a patient, and then it was observed how long it took the liver to eliminate it from blood plasma. The concentration of indocyanine green in the blood was measured using the developed optical setup [8].

A number of articles are devoted to the study of alterations caused by diabetes mellitus (DM) and cardiovascular diseases. Kozlov and colleagues developed a new method of signal processing and data analysis in digital LDF. The main result of the study is the development of a set of classifiers that allow one to identify typical patterns of microcirculation in healthy volunteers and DM patients based on the presented diagnostic algorithm [9]. Fedorovich and colleagues studied the changes in microcirculation parameters in different body positions using a distributed system of wearable LDF devices. They demonstrated the significance of a body position influence during the monitoring of microcirculatory parameters. The results obtained may be of particular interest for further integration of an LDF channel into wearable devices for monitoring the state of cardiovascular systems [10]. Maslianitsyna and colleagues found the correspondence between in vivo and in vitro optical methods by studying the aggregation parameters in patients with cardiovascular and concomitant pathologies. Understanding the link between red blood cells (RBC) aggregation and widespread cardiovascular diseases is vital to creating new methods of diagnosis and treatment. In this work, the aggregation of RBC was studied using different optical in vivo and in vitro measurement techniques. In vivo and in vitro methods yielded correlated results: the faster the cells moved in the capillaries, the less cells aggregated in vitro. DM had an additional significant effect on the aggregation properties of coronary heart disease patients. These findings are prominent for diagnosing and monitoring the state of

patients with pathologies that affect blood properties [11]. Machikhin and colleagues reported on an in vivo stain-free blood vessel imaging technique for the analysis of zebrafish embryonic development. The developed algorithm for processing bright-field microscopy images enables detection, mapping, and quantitative characterization of cardiac activity across the whole embryo. To validate the proposed approach, the blood flow velocity and heart rate dynamics were evaluated for multiple embryos at pre-larval stages. This non-invasive technique may shed light on the mechanism of vessels' activity initiation as well as the cardiovascular system resistance to environmental stresses [12].

Finally, Batool and colleagues reviewed and compiled the optical properties of human tissues and the circulatory system, especially blood. One of the main conclusions of this review is that there are numerous physical and methodological factors important for optical properties research and that one should be aware of them before performing their own measurements. The authors pointed out the main factors that affect absorption spectra of whole blood and hence influence optical properties. Revision of available polarimetric techniques can be helpful for readers who practice biomedical optics methods [13].

Thus, the presented Special Issue reflects novel innovative research and emerging ideas in optical non-invasive diagnostics for their wider translation into clinical practice, e.g., for the development of wearable technologies, personalized medicine, and robotic surgery.

**Funding:** This research received no external funding.

**Institutional Review Board Statement:** Not applicable.

**Informed Consent Statement:** Not applicable.

**Data Availability Statement:** Not applicable.

**Conflicts of Interest:** The author declares no conflict of interest.

## References

1. Zherebtsov, E.; Zajnulina, M.; Kandurova, K.; Potapova, E.; Dremin, V.; Mamoshin, A.; Sokolovski, S.; Dunaev, A.; Rafailov, E.U. Machine Learning Aided Photonic Diagnostic System for Minimally Invasive Optically Guided Surgery in the Hepatoduodenal Area. *Diagnostics* **2020**, *10*, 873. [CrossRef] [PubMed]
2. Gubarkova, E.V.; Kiseleva, E.B.; Sirotkina, M.A.; Vorontsov, D.A.; Achkasova, K.A.; Kuznetsov, S.S.; Yashin, K.S.; Matveyev, A.L.; Sovetsky, A.A.; Matveev, L.A.; et al. Diagnostic Accuracy of Cross-Polarization OCT and OCT-Elastography for Differentiation of Breast Cancer Subtypes: Comparative Study. *Diagnostics* **2020**, *10*, 994. [CrossRef] [PubMed]
3. Iida, T.; Kiya, S.; Kubota, K.; Jin, T.; Seiyama, A.; Nomura, Y. Monte Carlo Modeling of Shortwave-Infrared Fluorescence Photon Migration in Voxelized Media for the Detection of Breast Cancer. *Diagnostics* **2020**, *10*, 961. [CrossRef] [PubMed]
4. Huang, C.-L.; Lian, M.-J.; Wu, Y.-H.; Chen, W.-M.; Chiu, W.-T. Identification of Human Ovarian Adenocarcinoma Cells with Cisplatin-Resistance by Feature Extraction of Gray Level Co-Occurrence Matrix Using Optical Images. *Diagnostics* **2020**, *10*, 389. [CrossRef] [PubMed]
5. Streltsova, O.; Kuyarov, A.; Molvi, M.S.; Zubova, S.; Lazukin, V.; Tararova, E.; Kiseleva, E. New Approaches in the Study of the Pathogenesis of Urethral Pain Syndrome. *Diagnostics* **2020**, *10*, 860. [CrossRef] [PubMed]
6. Bryanskaya, E.O.; Novikova, I.N.; Dremin, V.V.; Gneushev, R.Y.; Bibikova, O.A.; Dunaev, A.V.; Artyushenko, V.G. Optical Diagnostics of the Maxillary Sinuses by Digital Diaphanoscopy Technology. *Diagnostics* **2021**, *11*, 77. [CrossRef] [PubMed]
7. Timchenko, E.; Timchenko, P.; Volova, L.; Frolov, O.; Zibin, M.; Bazhutova, I. Raman Spectroscopy of Changes in the Tissues of Teeth with Periodontitis. *Diagnostics* **2020**, *10*, 876. [CrossRef] [PubMed]
8. Savchenko, E.; Kolokolnikov, I.; Velichko, E.; Osovskikh, V.; Kiseleva, L.; Musakulova, Z. Design of Liver Functional Reserve Estimation Technique Based on Optical Densitometry. *Diagnostics* **2020**, *10*, 599. [CrossRef] [PubMed]
9. Kozlov, I.; Zherebtsov, E.; Masalygina, G.; Podmasteryev, K.; Dunaev, A. Laser Doppler Spectrum Analysis Based on Calculation of Cumulative Sums Detects Changes in Skin Capillary Blood Flow in Type 2 Diabetes Mellitus. *Diagnostics* **2021**, *11*, 267. [CrossRef] [PubMed]
10. Fedorovich, A.A.; Loktionova, Y.I.; Zharkikh, E.V.; Mikhailova, M.A.; Popova, J.A.; Suvorov, A.V.; Zherebtsov, E.A. Body Position Affects Capillary Blood Flow Regulation Measured with Wearable Blood Flow Sensors. *Diagnostics* **2021**, *11*, 436. [CrossRef] [PubMed]
11. Maslianitsyna, A.; Ermolinskiy, P.; Lugovtsov, A.; Pigurenko, A.; Sasonko, M.; Gurfinkel, Y.; Priezzhev, A. Multimodal Diagnostics of Microrheologic Alterations in Blood of Coronary Heart Disease and Diabetic Patients. *Diagnostics* **2021**, *11*, 76. [CrossRef] [PubMed]

12. Machikhin, A.S.; Volkov, M.V.; Burlakov, A.B.; Khokhlov, D.D.; Potemkin, A.V. Blood Vessel Imaging at Pre-Larval Stages of Zebrafish Embryonic Development. *Diagnostics* **2020**, *10*, 886. [CrossRef] [PubMed]
13. Batool, S.; Nisar, M.; Mangini, F.; Frezza, F.; Fazio, E. Scattering of Light from the Systemic Circulatory System. *Diagnostics* **2020**, *10*, 1026. [CrossRef] [PubMed]

diagnostics

MDPI

*Article*

# Body Position Affects Capillary Blood Flow Regulation Measured with Wearable Blood Flow Sensors

**Andrey A. Fedorovich [1,2], Yulia I. Loktionova [3,†], Elena V. Zharkikh [3,†], Maria A. Mikhailova [1], Julia A. Popova [2], Alexander V. Suvorov [2] and Evgeny A. Zherebtsov [3,4,*]**

[1] National Medical Research Center for Therapy and Preventive Medicine of the Ministry of Healthcare of the Russian Federation, Petroverigsky 10, 101990 Moscow, Russia; faa-micro@yandex.ru (A.A.F.); marya.filina-2015@yandex.ru (M.A.M.)
[2] Russian Federation State Research Center, Institute of Biomedical Problems of the Russian Academy of Sciences, Khoroshevskoe Highway 76A, 123007 Moscow, Russia; julija.popova@gmail.com (J.A.P.); suvalex@inbox.ru (A.V.S.)
[3] Orel State University, Komsomolskaya 95, 302026 Orel, Russia; julya-loktionova@mail.ru (Y.I.L.); ev.zharkikh@gmail.com (E.V.Z.)
[4] Optoelectronics and Measurement Techniques, University of Oulu, Erkki Koiso-Kanttilankatu 3, 90014 Oulu, Finland
* Correspondence: evgenii.zherebtsov@oulu.fi
† These authors contributed equally to this work.

check for updates

**Citation:** Fedorovich, A.A.; Loktionova, Y.I.; Zharkikh, E.V.; Mikhailova, M.A.; Popova, J.A.; Suvorov, A.V.; Zherebtsov, E.A. Body Position Affects Capillary Blood Flow Regulation Measured with Wearable Blood Flow Sensors. *Diagnostics* **2021**, *11*, 436. https://doi.org/10.3390/diagnostics11030436

Academic Editor: Xavier Muñoz-Berbel

Received: 31 January 2021
Accepted: 24 February 2021
Published: 4 March 2021

**Publisher's Note:** MDPI stays neutral with regard to jurisdictional claims in published maps and institutional affiliations.



**Abstract:** In this study we demonstrate what kind of relative alterations can be expected in average perfusion and blood flow oscillations during postural changes being measured in the skin of limbs and on the brow of the forehead by wearable laser Doppler flowmetry (LDF) sensors. The aims of the study were to evaluate the dynamics of cutaneous blood perfusion and the regulatory mechanisms of blood microcirculation in the areas of interest, and evaluate the possible significance of those effects for the diagnostics based on blood perfusion monitoring. The study involved 10 conditionally healthy volunteers (44 ± 12 years). Wearable laser Doppler flowmetry monitors were fixed at six points on the body: two devices were fixed on the forehead, on the brow; two were on the distal thirds of the right and left forearms; and two were on the distal thirds of the right and left lower legs. The protocol was used to record three body positions on the tilt table for orthostatic test for each volunteer in the following sequence: (a) supine body position; (b) upright body position (+75°); (c) tilted with the feet elevated above the head and the inclination of body axis of 15° (−15°, Trendelenburg position). Skin blood perfusion was recorded for 10 min in each body position, followed by the amplitude–frequency analysis of the registered signals using wavelet decomposition. The measurements were supplemented with the blood pressure and heart rate for every body position analysed. The results identified a statistically significant transformation in microcirculation parameters of the average level of skin blood perfusion and oscillations of amplitudes of neurogenic, myogenic and cardiac sensors caused by the postural changes. In paper, we present the analysis of microcirculation in the skin of the forehead, which for the first time was carried out in various positions of the body. The area is supplied by the internal carotid artery system and can be of particular interest for evaluation of the sufficiency of blood supply for the brain.

**Keywords:** wearable blood flow sensors; blood perfusion; laser Doppler flowmetry; ortostatic test; postural changes; body position; blood perfusion in forehead; blood perfusion in wrists; blood perfusion in shins; blood perfusion oscillations; vasomotions

## 1. Introduction

The functional state and balance in regulation mechanisms of the cardiovascular system are some of the main factors determining the robustness in a living organism. The evolutionary development of vertebrates in a field of gravitational attraction has led to

series of adaptations in the blood supply system. Changes in hemodynamic parameters depending on the position of the body significantly assist the homeostasis in the limbs and essentially in the sufficiency of blood supply for the brain [1]. For the last two decades, laser Doppler perfusion monitoring has become an established technique capable of providing useful diagnostic information about parameters of regulation of the skin blood perfusion. The recent emergence of laser Doppler flowmetry (LDF) as a wearable device has allowed for detailed assessments of individual adaptive capabilities of the blood flow circulation system and can be of particular interest for diagnostics and sport medicine. The next decade is likely to witness a considerable rise of novel optical sensor technologies in wearable sensors, not only to be used as fitness trackers, but to provide clinicians with diagnostic information with better sensitivity and specificity.

Earlier studies have shown significant variability of the cardiovascular system's parameters (in particular, heart rate and blood pressure) associated with posture and body position [2–4]. It has also been shown that parameters of gender and age significantly affect the reactivity of blood flow in response to postural change [5]. It is known that different anatomical parts of the human body demonstrate differences in the blood flow regulation mechanisms [6]. In that respect, regional variability of the effects in microcirculation should also be taken into account. Previous studies reported that the low-frequency mechanisms of microcirculation regulation (endothelial, neurogenic and myogenic) measured with the LDF technique differ between the arm and leg regions under thermoneutral conditions [7,8]. It has also been shown that regulation of microcirculation differs in the leg and forearm under local heating [8]. The regions of glabrous and nonglabrous skin are also reported to have different responses of different types in the parameters of blood perfusion under the type of functional loading [9].

In the study of I. Tikhonova et al., it was found that a postural test (change of supine position to sitting) did not influence the forearm skin blood flow oscillations; they noted a remarkable increase in the respiratory flow and a decrease in the cardiac oscillations in the blood microcirculation in the skin of the legs [10]. The work [11] presents the results of a study of the effects of body position on oxygen consumption ($VO_2$) and hemodynamics. It was found that the heart rate, the blood pressure and the product of velocity pressure and oxygen consumption were highest in the sitting position compared to the lying position, and lowest in the lying position on the left side. Narayanan et al. [12] published results on a study of changes in the parameters of blood pressure (BP) and the speed of cerebral blood flow (CBFV) when changing the body position from sitting to vertical in young and old people. It is noted that in young people the linear relationship between blood pressure and the blood flow rate of the middle cerebral artery in stationary sitting conditions changes with orthostatic stress in a wide range of physiological frequencies. Nevertheless, the effects in the parameters of skin microcirculation during changes of the posture and body position were not studied comprehensively, so a lack of systematically conducted research can be identified in this area.

Multi-point measurements using recently developed wearable laser Doppler flowmetry devices [13] can be effectively used for simultaneous recordings of blood perfusion signals from arbitrary anatomical skin sites, thereby providing great potential for finding multiple applications in physiological measurements and medial diagnostics in the near future. One of the challenges that can be mitigated by the use of the distributed measuring system is the difficulty of the high spatial heterogeneity of the LDF signal. Recently, the prototypes of the measuring system have been validated by authors of the work demonstrating the effectiveness of using laser wearable Doppler analyzers for measurements of the parameters of skin blood microcirculation. It has been demonstrated that the sensitivity of the wearable 850 nm VCSEL-basedblood perfusion sensors is sufficient to reliably register physiological changes in skin blood perfusion [14–16], including high coherence of blood flow oscillation in the contralateral limbs of healthy volunteers in the basal state and during functional tests [17].

The wireless LDF sensors have been tested in the realm of pre-clinical trials in healthy volunteers of different ages and patients with type 2 diabetes [14,16,18,19]. Additionally, the dynamical changes in the blood perfusion evaluated by LDF and laser speckle contrast imaging techniques were compared, demonstrating that both techniques can be used for the recording of the blood perfusion oscillations [20].

Thus, the use of wearable LDF sensors is promising for both health monitoring, and for evaluating the effectiveness of treatment and monitoring its dynamics. While the multi-point recordings of blood perfusion have demonstrated great promise for the diagnostics of vascular complications, there is a significant gap of knowledge on the effects of the body position during measurements, which introduce systematic impact and additional variability to the recorded signals, which requires accurate systematic studies for the main cases such as measurements while standing upright and in supine position.

Thus far, to the best of our knowledge, no one has systematically studied the effects of postural changes on the skin blood flow by use of wearable LDF sensors as a prime measuring technique. A review identified only one study that used a miniaturized LDF device for the measurements of hemodynamic changes in response to changes of body position [21]. The authors reported a decrease in earlobe microcirculation in response to the squat–standing and the footstool standing tests synchronized with the decrease in blood pressure in subjects. Nevertheless, the mentioned research lacks systematic studies of the effects taking place during the transition of body position from lying supine to standing upright. Thus, the overall aim of this work was to study the reaction of the microcirculation system in skin to changes in body position using the newest wireless wearable measuring platform for the multi-point blood perfusion recordings.

## 2. Material and Methods

The technique of laser Doppler flowmetry (LDF) measurements with a prototyping system consisting of 6 wireless compact sensors manufactured by SPE "LAZMA" Ltd. (Moscow, Russia) has been applied in this study for the registration of the skin blood perfusion. The LDF method is based on the coherent techniques with the analysis of the laser radiation scattered by moving red blood cells in the living tissue. The output signal of blood perfusion with the LDF method (Figure 1) is a time sequence of an integral parameter that depends on the speed of red blood cells and their concentration in the diagnosed volume.

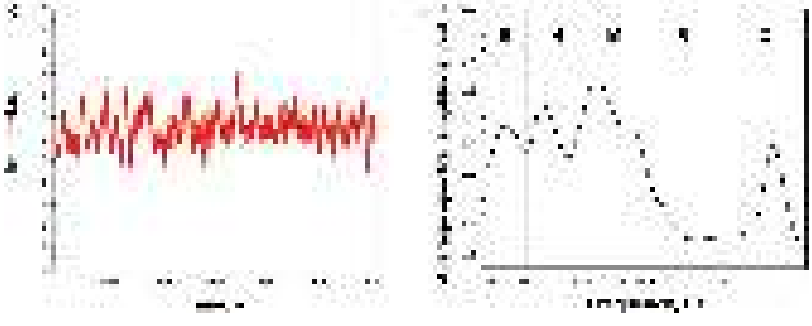

**Figure 1.** Representative trace of laser Doppler flowmetry (LDF) recordings by the employed measuring system (**a**), the wavelet analysis of the LDF signal with the highlighted frequency ranges for E—endothelial (e, 0.095–0.021 Hz), N—neurogenic (n, 0.021–0.052 Hz), M—myogenic (m, 0.052–0.145 Hz), R—respiratory (r, 0.145–0.6 Hz) and C—cardiac (c, 0.6–2 Hz) regions of blood flow modulation (**b**).

The distributed measuring system has built-in channels for recording microcirculation blood flow and allows for simultaneous measurements at multiple points of the human body. Every measuring device of the system employs compact VCSELs with an

emission wavelength of 850 nm and the power of output of the laser radiation of about 1 mW. Apart from the blood flow measurements, the analyzers were also equipped with a built-in accelerometer to monitor and eliminate possible motion artifacts and a skin temperature sensor.

The object of the study was a cohort of 10 conditionally healthy male volunteers, whose average age was 44 ± 12 years, height 177 ± 6 cm, weight 77 ± 6 kg, BMI 24.5 ± 1.9. All participants were staff testers of the Institute of Biomedical Problems of the Russian Academy of Sciences (IBMP RAS); twice a year they undergo a comprehensive clinical examination for admission to participate in the physiological studies. The main areas of scientific activity of the Institute are research in the fields of space biology, physiology and medicine, which is the reason for the high requirements for the physiological state of the testers. The IBMP RAS Biomedical Ethics Commission has approved the experimental studies, min number 483 dated 3 August 2018, following the rules of the Declaration of Helsinki of 1975, revised in 2013. All volunteers signed informed consent prior to the study. The LDF sensors were located at 6 points on the body: 2 devices were fixed on the forehead above the eyebrows; 2 on the distal third of the outer surface of the forearm (each arm), 2–3 cm proximal to the wrist joint; and 2-in the distal third of the shins along the anterior surface of the tibia, 10 cm proximal to the medial malleolus.

The studies were carried out in a laboratory with a maintained microclimate (air temperature $+23 \pm 1$ °C; humidity 40–60%) in the morning (from 09:00 to 12:00). The studies were carried out in the same order on all subjects (Figure 2)—(1) horizontal position; (2) orthostasis ($+75°$); (3) head-down position of the body ($-15°$, Trendelenburg position). The study was carried out on a turntable, which was developed and manufactured by the Special Design Bureau of the Institute of Biomedical Problems of the Russian Academy of Sciences. The table has a mechanical drive that allows one to change and fix the angle of inclination of the surface with a step size of 5° in the range from $-30°$ to $+90°$ with a maximum speed of position change of up to 20 °/s. The table is equipped with a leg rest, and chest and knee safety belts. Transfer of subjects from horizontal position to orthostasis took 7–10 s, from orthostasis to Trendelenburg position—9–12 s. Cutaneous perfusion was recorded for 10 min at each body position. The adaptation of the subjects to the horizontal position lasted 10–15 min, during which time the sensors were fixed and the research equipment was adjusted. During the transition to orthostasis and the Trendelenburg position, the registration of cutaneous perfusion began after 2 min of adaptation to the new body position. Immediately before the change in body position, hemodynamic parameters were recorded with an automatic tonometer "OMRON M10-IT" (OMRON HEALTHCARE Co, Ltd., Kyoto, Japan) on the right hand, due to the design features of the turntable—a technical "pocket" for placing additional research equipment is located on the right. The temperature of the skin in each area of the study was monitored continuously throughout the entire study by built-in thermal sensors. The protocol was used for recordings in three body positions for each volunteer (Figure 2): (a) horizontal body position; (b) vertical position of the body (head at the top); (c) head tilted down (15° from the horizontal, Trendelenburg position).

The applied combination of the Trendelenburg position and orthostatic probe makes it possible to characterize the functional reserve of the blood circulatory system for the volunteers, and to correlate the adaptations of peripheral hemodynamics to the body position changes. The Trendelenburg position is known to be an effective method to change cerebral perfusion, and to fill and stretch the upper central veins and the external jugular vein [22].

The measuring procedure was composed of several stages. One basal recording of blood perfusion for every body position took 10 min; then the blood pressure was measured. Thus, for each spatial position, three pairs of measurements were recorded at the corresponding symmetrical points on the forehead, wrists and shins.

**Figure 2.** The measurements have been conducted and compared for three distinct body positions on a tilt table: (**A**) supine; (**B**) upright; (**C**) tilted with the feet elevated above the head and an inclination of body axis of 15 °(Trendelenburg position).

The amplitude–frequency characteristics of the skin perfusion oscillations were calculated using the mathematical apparatus of the wavelet transform. The wavelet spectrum of the signal was calculated according to the following expression:

$$W(s,\tau) = \frac{1}{\sqrt{s}} \int_{-\infty}^{\infty} x(t)\psi^*\left(\frac{t-\tau}{s}\right) \quad (1)$$

where $x(t)$ is a sample of the signal, $\tau$ is time index, $s$ is scaling factor, * means complex conjugation. As a core wavelet, Morlet wavelet function $\psi(t) = e^{2\pi i t} \cdot e^{-t^2/\sigma}$ was choosen with decay parameter $\sigma = 1$.

The time-averaged amplitude of vasomotions was assessed by the maximum values (Ai) in the corresponding frequency ranges for endothelial (e, 0.095–0.021 Hz), neurogenic (n, 0.021–0.052 Hz), myogenic (m, 0.052–0.145 Hz), respiratory (r, 0.145–0.6 Hz) and cardiac (c, 0.6–2 Hz) regions of blood flow modulation [23] (Figure 1b). The level of cutaneous perfusion (Im) and the amplitude of the units of modulation of microcirculation (Ai) were assessed as quantitative parameters measured in arbitrary (perfusion) units (p.u.). The wavelet analysis has been implemented in the MATLAB software environment. The LDF signals in this particular study were not a subject of pre-processing or filtering before the analysis. The statistical analysis was performed in Origin Pro 2019b (vers. 9.65) software. Due to the limited size of the sample, a non-parametric Mann–Whitney U test was used for the check of statistical significance of differences.

## 3. Results

### *3.1. Measurements Conducted on Wrists*

The results of the amplitude analysis of cutaneous perfusion in the skin of the wrists are shown in Figure 3.

From the data obtained, it can be seen that during the transition from the horizontal position to orthostasis, the level of cutaneous perfusion has an insignificant tendency to decrease, which is accompanied by significant decreases in the amplitude of cardiac oscillations in blood flow and the amplitude of vasomotions of all tone-forming mechanisms of microcirculation—endothelial, neurogenic and myogenic. During the transition from orthostasis to the Trendelenburg position, the level of skin perfusion significantly increased, which was accompanied by significant increases in the amplitudes of cardiac and myogenic oscillations. There were no significant differences between the Trendelenburg position and the horizontal position for any of the analyzed parameters. The level of perfusion and the amplitude of the cardiac fluctuations both have a clear tendency to increase, but we did not find significant differences.

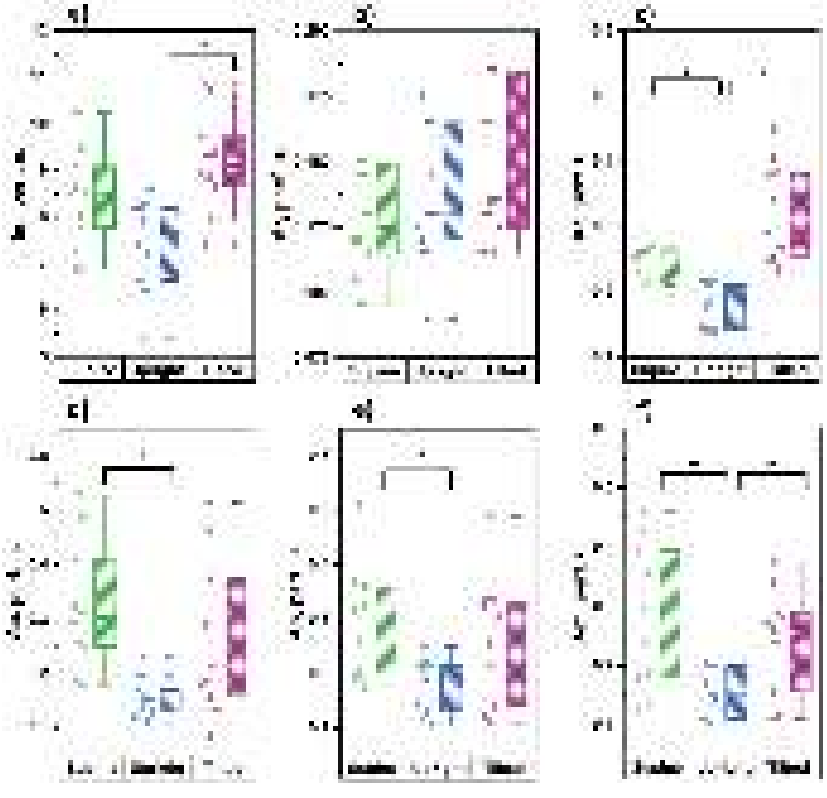

**Figure 3.** Analysis of average blood perfusion parameters on the wrists for three tested body positions: supine, upright and tilted (Trendelenburg position): (**a**) average blood perfusion; (**b**) cardiac oscillations; (**c**) respiratory oscillations; (**d**) endotelial oscillations; (**e**) neurogenic oscillations; (**f**) myogenic oscillations (* the significance of a difference between values was confirmed with $p < 0.05$ using the the Mann–Whitney test).

### *3.2. Measurements on Lower Legs*

Figure 4 demonstrates the distribution of the studied parameters during measurements in the lower third of shin.

The parameters of microcirculatory blood flow demonstrated a significant decrease in the average level of tissue perfusion and the amplitude of cardiac oscillations during the transition to orthostasis. During the change from orthostasis to the Trendelenburg position, these parameters significantly increased and were comparable with those measured in the horizontal position. In contrast to the measurements conducted in forearms, the functional state of the tone-forming mechanisms of microcirculation modulation in shins (parameters Ae, An and Am) did not demonstrate any significant changes during all three stages of the study.

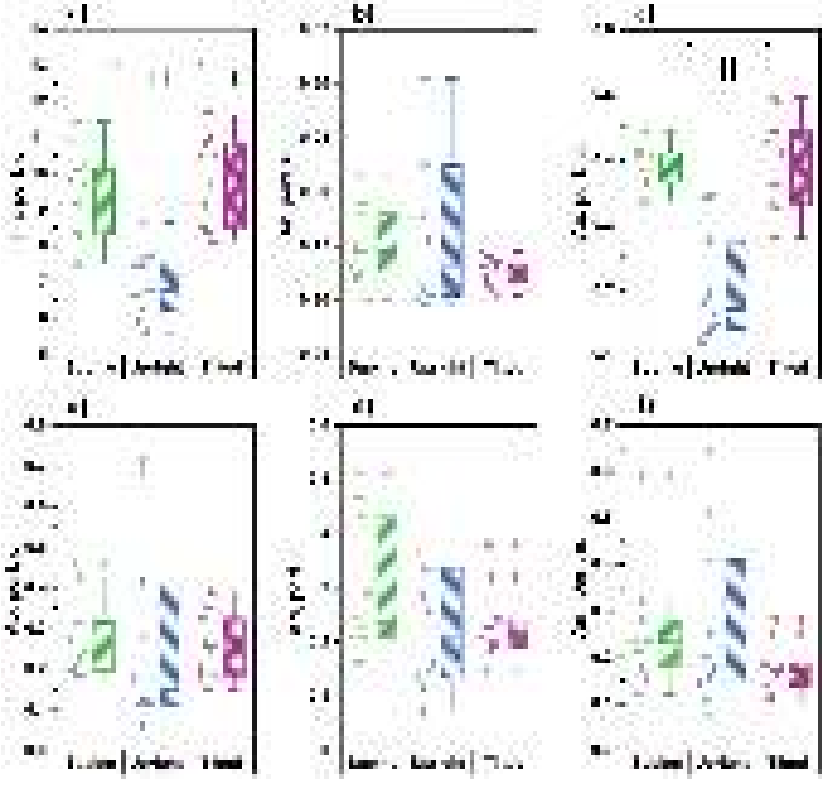

**Figure 4.** Analysed blood perfusion parameters measured on the shins for three body positions: supine, upright and tilted (Trendelenburg position): (**a**) average blood perfusion; (**b**) cardiac oscillations; (**c**) respiratory oscillations; (**d**) endotelial oscillations; (**e**) neurogenic oscillations; (**f**) miogenic oscillations (* the significance of a difference between values was confirmed with $p < 0.05$ using the Mann–Whitney test)

### *3.3. Measurements on the Forehead*

Figure 5 shows the results of the measurements of the cutaneous blood perfusion dynamics on the forehead.

During measurements on the forehead, we did not register any significant changes in the index of microcirculation caused by postural changes. With unchanged tissue perfusion, however, significant increases in the amplitudes of neurogenic and myogenic oscillations were recorded when changing from a supine to an upright position, which is the opposite of the results obtained in the shins. Despite the presence of a tendency towards moderate increases in the amplitudes of endothelial and neurogenic oscillations in the Trendelenburg position, these changes did not reach statistically significant levels.

### *3.4. Blood Pressure and Heart Rate*

Before each stage of the study, for every tested subject the parameters of blood pressure and heart rate were recorded via the right arm. The results of these measurements are shown in Figure 6.

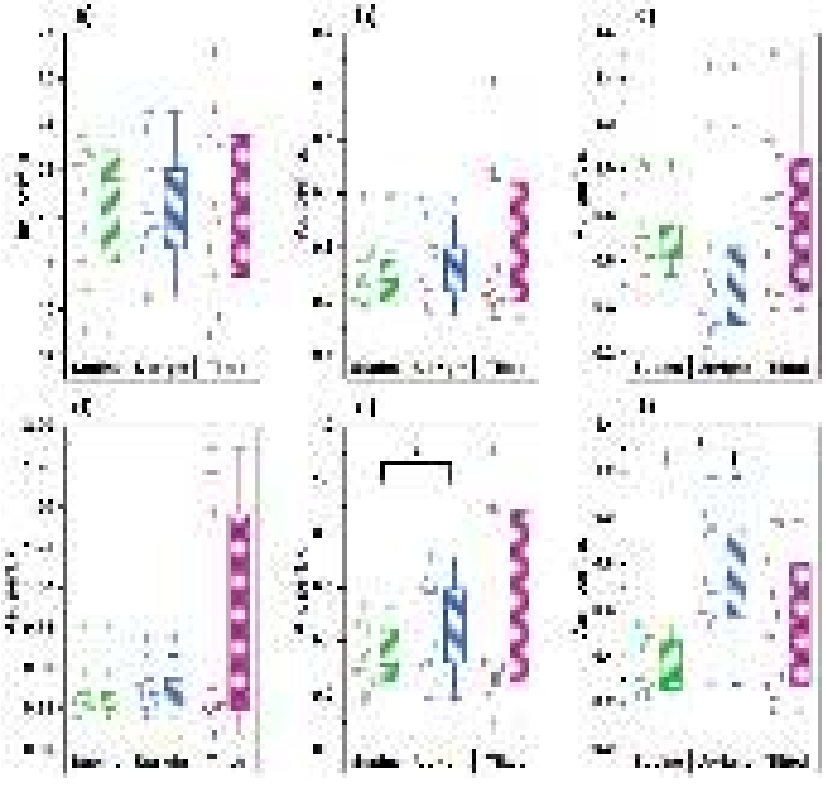

**Figure 5.** Analysis of blood perfusion parameters in the skin of the brow of the forehead for three tested body positions: supine, upright and tilted (Trendelenburg position): (**a**) average blood perfusion; (**b**) cardiac oscillations; (**c**) respiratory oscillations; (**d**) endotelial oscillations; (**e**) neurogenic oscillations; (**f**) miogenic oscillations (* the significance of a difference between values was confirmed with $p < 0.05$ using the Mann–Whitney test).

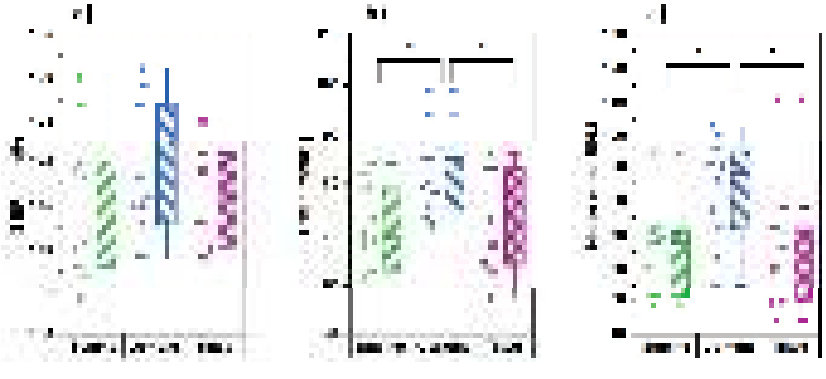

**Figure 6.** Analysis of parameters of blood pressure and hear rate measured in the tested body positions: supine, upright and tilted (Trendelenburg position): (**a**) systolic blood pressure; (**b**) diastolic blood pressure; (**c**) heart rate (* the significance of a difference between the values was confirmed with $p < 0.05$ using the Mann–Whitney test).

From the data obtained, it can be seen that in the position of orthostasis, significantly higher values of diastolic pressure and heart rate were observed compared to the supine and the Trendelenburg positions. At the same time, the values of systolic blood pressure did not undergo significant changes during postural changes.

## 4. Discussion

The value of the skin microvascular bed as an object of research for identifying the patterns of the cardiovascular system functioning is under discussion nowadays. In a review work, based on the results of LDF amplitude–frequency wavelet analysis, Martini R. and Bagno A. showed that changes in the parameters of the skin microcirculation are detected in the widest range of diseases [24]. This includes studies of diabetes complications [25], peripheral arterial disease [26] and arterial hypertension [27] among other conditions.

It is known that the microvascular bed of the skin is not subject to baroreflex regulation [28,29], and the results we obtained on the forearm are very interesting. During the transition to orthostasis, when the measurement area was below the height of the heart, we noted decreases in the amplitudes of endothelial, neurogenic and myogenic vasomotions. A decrease in the vasomotions' amplitude indicates a decrease in the lumen size of resistive precapillary arterioles, which can be regarded as an increase in the vascular tone. It can be assumed that a decrease in the lumen of resistive precapillary arterioles leads to a decrease in the amplitude of cardiac oscillations in microvessels, which, in turn, indicates a decrease in arterial blood flow to the capillaries. A decrease in the amplitude of cardiac oscillations at the level of precapillary arterioles can be caused by several mechanisms: (1) An increase in hydrostatic pressure in the venular link of the vascular bed amidst the difficulty in the blood outflow from the capillaries leads to an increase in the capacitive vessels tone, which, through the mechanisms of venulo-arteriolar communication, can lead to an increase in the tone of the bringing arterioles [30]. (2) Activation of the sympathoadrenal system due to weakening of the depressor effects on it from the baroreceptors of the carotid sinus. Amidst that, the subjects showed a significant increase in diastolic blood pressure and heart rate. We did not find a significant correlation between these parameters, which may have been due to a small sample size, but it can be assumed that there is a relationship between the amplitude of vasomotions of the tone-forming mechanisms of skin microvessels and the level of blood pressure. If this hypothesis is correct, then the LDF technique can be a useful additional tool for interpreting the results of 24-h blood pressure monitoring when patients are in an upright position for most of the day, and for monitoring the functional state of resistive skin microvessels when prescribing antihypertensive therapy.

When the head is lowered 15° below the horizontal line, the measurement point on the forearms is slightly above the heart level, which does not affect the functional state of the tone-forming regulatory mechanisms of skin microcirculation in the upper extremities. Amidst this, there is a significant increase in the amplitude of the cardiac oscillations, which can be explained by the opposite mechanisms observed in orthostasis: (1) the precapillary arterioles' tone is restored through the mechanisms of venulo-arteriolar communication against the background of a decrease in pressure in the venous vessels; (2) a decrease in the activity of the sympathoadrenal system amidst the restoration of the depressor activity of the carotid sinuses. An increase in the arterial blood inflow into the microvasculature is accompanied by a significant increase in the level of tissue perfusion (Figure 3a). For the lower extremities, a change in body position leads to a decrease in the amplitude of cardiac oscillations (a decrease in inflow), and a corresponding decrease in the level of tissue perfusion without changing the activity of tone-forming mechanisms at the level of resistive precapillary arterioles. This is most likely due to regional features of the tissue perfusion regulation of the skin in the legs and is of a compensatory nature aimed at maintaining nutritive blood flow in conditions of decreased tissue perfusion. In a non-physiological position for the legs, when they are above the heart, the outflow of venous blood is significantly facilitated, but the perfusion pressure decreases. Amidst this, we see an insignificant tendency towards a decrease in the amplitude of neurogenic and myogenic

vasomotions (increased tone), which can also be regarded as a compensatory response aimed at maintaining perfusion pressure in the skin capillaries.

The results of the study of skin perfusion in the forehead can be of particular interest in connection with the brain's blood supply. It is known that the scalp receives nutrition from the external carotid artery system, and only the skin of the forehead is supplied with blood from the a.supratrochlearis and a.supraorbitalis, which are the final branches of the supraorbital arteries that are part of the internal carotid artery system [31]. The researchers' interest in the basin of the a.supraorbitalis is due to the fact that disorders of microcirculatory blood flow in the eye area (fundus and bulbar conjunctiva) are associated with various variants of cerebral circulatory disorders [32–34]. As was shown in the pilot study [35], the nature of skin microcirculation in the forehead significantly differs in the level of skin perfusion and in the activity of regulatory mechanisms, depending on the side and volume of ischemic brain damage, and during thrombolytic therapy, these parameters showed significant changes.

The higher level of average blood perfusion in skin of the forehead, relative to the skin of the upper and lower extremities, and the stability of cutaneous blood perfusion in any position of the body (Figure 5a), draw attention. This may indicate a high potential of the mechanisms of autoregulation of cerebral blood flow. Significant changes in the regulatory mechanisms at the level of precapillary arterioles are observed only in orthostasis and are expressed in an increase of amplitude of neurogenic and myogenic vasomotations. When the head is higher than the heart, the neurogenic and myogenic mechanisms of microvascular tone-forming are reduced.

In the Trendelenburg position, when not only the outflow of venous blood from the head is hindered, but also the pressure in the arterial bed increases, the functional state of the tone-forming mechanisms changes in a very wide range. We assume that this is due to the high potential of the mechanisms of regulation of cerebral hemodynamics. For the tone-forming mechanisms of microcirculation regulation (Ae, An and Am), changing their functional activity according to the principle of positive and negative responses, modulates the volume and speed of arterial blood flowing to the capillaries (Ac) to the optimal values for transcapillary exchange in the vascular volume at the time, and in our study—depending on the position of the body in space.

The facial skin, as an object of research, is also interesting due to its features of innervation. The system of innervation of skin microvessels is mainly represented by somatic sensitive (afferent) and vegetative sympathetic (efferent) systems of regulation. The direct involvement of the parasympathetic nervous system in the regulation of cutaneous microvessels is considered proven only for the skin of the face [32,36]. Thus, the study of microcirculatory blood flow in the area of the facial skin opens up opportunities for studying almost all mechanisms of neurogenic control of the vasomotor activity of resistive microvessels at the opposite end to the heart pole of the great circle of blood circulation [37].

## 5. Conclusions

The novel wearable sensors implementing the measuring principles of laser Doppler and dynamic light scattering techniques for blood perfusion monitoring significantly extend the capabilities of researchers and practical clinicians in terms of monitoring parameters of skin blood perfusion. The analysis of signals recorded by the wearable LDF devices can be effectively realized using machine learning algorithms. Nevertheless, practical applications of the sensors for medical diagnostics require taking into account a considerable number of details. Some of the factors greatly influencing the patterns of the blood perfusion behavior are the posture and body position. In this study, we demonstrate what kind of relative changes can be expected in average perfusion and blood flow oscillations during postural changes being measured on skin of the limbs and on the brow of forehead. We show the importance of taking into account the position of the body in space during the monitoring of physiological parameters interrelated with blood perfusion. Presented findings of the amplitude–frequency analysis of LDF signals measured in different body

positions confirm the early promise of the measurement technique for the orthostatic test and diagnostic procedures based on it, and more specifically, for the use of this particular type of wearable device together with the physiological tests. The results obtained can be of particular interest for the development of new protocols for the study of microcirculation, including those related to daily monitoring. The vast majority of modern fitness trackers use the method of photoplethysmography to record physiological parameters. In this and previous works, we have shown that the LDF method can also be of significant interest for wearable applications, opening up new opportunities for the diagnostics of the microcirculation and cardiovascular systems.

## 6. Patents

1. E.A. Zherebtsov, I.O. Kozlov, A.I. Zherebtsova, E.V. Zharkikh, Y.I. Loktionova and A.V. Dunaev, "Software for data analysis of multi-channel wearable device for recording the level of capillary blood flow." Software patent RU 2019665950 (2019).
2. I.O. Kozlov and E.A. Zherebtsov, "Software for recording the distribution of blood perfusion by Doppler shift frequencies." Software patent RU 2019616389 (2019).

**Author Contributions:** Conceptualization, methodology, investigation, discussion, writing—review and editing, A.A.F.; writing—original draft preparation, formal analysis, Y.I.L.; writing—original draft preparation, discussion, E.V.Z.; investigation, data curation, M.A.M.; investigation, J.A.P.; methodology, investigation, A.V.S.; discussion, funding acquisition, project administration, formal analysis, E.A.Z. All authors edited the manuscript. All authors have read and agreed to the published version of the manuscript.

**Funding:** The reported study was funded by the Russian Foundation for Basic Research (RFBR), grant number 20-08-01153. A. Fedorovich, J. Popova and A. Suvorov were funded in the framework of the research topic 64.1 by the Russian Academy of Science (RAS). E. Zherebtsov acknowledges the funding from the Academy of Finland, grant number 318281.

**Institutional Review Board Statement:** The study was conducted according to the guidelines of the Declaration of Helsinki, and approved by the Ethics Committee of Institute of Biomedical Problems of the Russian Academy of Sciences (protocol code 483, 3 August 2018).

**Informed Consent Statement:** Informed consent was obtained from all subjects involved in the study.

**Data Availability Statement:** The data presented in this study are available on request from the corresponding author.

**Acknowledgments:** The authors express their acknowledgements to all the volunteers who contributed to the present study.

**Conflicts of Interest:** The authors declare no conflict of interest. The funders had no role in the design of the study; in the collection, analyses, or interpretation of data; in the writing of the manuscript, or in the decision to publish the results.

## References

1. Cooke, W.H.; Pellegrini, G.L.; Kovalenko, O.A. Dynamic cerebral autoregulation is preserved during acute head-down tilt. *J. Appl. Physiol.* **2003**, *95*, 1439–1445. [CrossRef]
2. Borst, C.; Wieling, W.; Van Brederode, J.; Hond, A.; De Rijk, L.; Dunning, A. Mechanisms of initial heart rate response to postural change. *Am. J. Physiol. Heart Circ. Physiol.* **1982**, *243*, H676–H681. [CrossRef] [PubMed]
3. Borst, C.; Van Brederode, J.; Wieling, W.; Van Montfrans, G.; Dunning, A. Mechanisms of initial blood pressure response to postural change. *Clin. Sci.* **1984**, *67*, 321–327. [CrossRef] [PubMed]
4. Klijn, E.; Niehof, S.; Groeneveld, A.J.; Lima, A.P.; Bakker, J.; van Bommel, J. Postural change in volunteers: Sympathetic tone determines microvascular response to cardiac preload and output increases. *Clin. Auton. Res.* **2015**, *25*, 347–354. [CrossRef]
5. Barantke, M.; Krauss, T.; Ortak, J.; Lieb, W.; Reppel, M.; Burgdorf, C.; Pramstaller, P.P.; Schunkert, H.; Bonnemeier, H. Effects of gender and aging on differential autonomic responses to orthostatic maneuvers. *J. Cardiovasc. Electrophysiol.* **2008**, *19*, 1296–1303. [CrossRef]
6. Thiriet, M. *Biology and Mechanics of Blood Flows: Part II: Mechanics and Medical Aspects*; Springer: New York, NY, USA, 2008. [CrossRef]

7. Del Pozzi, A.T.; Carter, S.J.; Collins, A.B.; Hodges, G.J. The regional differences in the contribution of nitric oxide synthase to skin blood flow at forearm and lower leg sites in response to local skin warming. *Microvasc. Res.* **2013**, *90*, 106–111. [CrossRef] [PubMed]
8. Hodges, G.J.; Del Pozzi, A.T. Noninvasive examination of endothelial, sympathetic, and myogenic contributions to regional differences in the human cutaneous microcirculation. *Microvasc. Res.* **2014**, *93*, 87–91. [CrossRef]
9. Sorelli, M.; Stoyneva, Z.; Mizeva, I.; Bocchi, L. Spatial heterogeneity in the time and frequency properties of skin perfusion. *Physiol. Meas.* **2017**, *38*, 860. [CrossRef] [PubMed]
10. Tikhonova, I.V.; Grinevich, A.A.; Guseva, I.E.; Tankanag, A.V. Effect of orthostasis on the regulation of skin blood flow in upper and lower extremities in human. *Microcirculation* **2020**, e12655. [CrossRef]
11. Alice Y.M.; Jones, E.D. Body position change and its effect on hemodynamic and metabolic status. *Heart Lung* **2004**, *33*, 281–290. [CrossRef]
12. Narayanan, K.; James, J.C.; Hamner, J.; Mukai, S.; Lipsitz, L.A. Predicting cerebral blood flow response to orthostatic stress from resting dynamics: Effects of healthy aging. *Am. J. Physiol. Regul. Integr. Comp. Physiol.* **2001**, *281*, 716–722. [CrossRef] [PubMed]
13. Zherebtsov, E.; Sokolovski, S.; Sidorov, V.; Rafailov, I.; Dunaev, A.; Rafailov, E. Novel wearable VCSEL-based blood perfusion sensor. *Proc. SPIE* **2018**, 564. [CrossRef]
14. Zherebtsov, E.; Zharkikh, E.; Kozlov, I.; Loktionova, Y.; Zherebtsova, A.; Rafailov, I.; Sokolovski, S.; Sidorov, V.; Dunaev, A.; Rafailov, E. Wearable sensor system for multipoint measurements of blood perfusion: Pilot studies in patients with diabetes mellitus. *Proc. SPIE* **2019**, 62. [CrossRef]
15. Loktionova, Y.; Zharkikh, E.; Kozlov, I.; Zherebtsov, E.; Bryanskaya, S.; Zherebtsova, A.; Sidorov, V.; Sokolovski, S.; Dunaev, A.; Rafailov, E. Pilot studies of age-related changes in blood perfusion in two different types of skin. *Proc. SPIE* **2019**, 37. [CrossRef]
16. Loktionova, Y.; Zherebtsov, E.; Zharkikh, E.; Kozlov, I.; Zherebetsova, A.; Sidorov, V.; Sokolovski, S.; Rafailov, I.; Dunaev, A.; Rafailov, E. Studies of age-related changes in blood perfusion coherence using wearable blood perfusion sensor system. *Proc. SPIE* **2019**, *11075*, 1107507. [CrossRef]
17. Zherebtsov, E.; Zharkikh, E.; Kozlov, I.; Zherebtsova, A.; Loktionova, Y.; Chichkov, N.; Sidorov, V.; Dunaev, A.; Rafailov, E.; Sokolovski, S.; et al. Novel wearable VCSEL-based sensors for multipoint measurements of blood perfusion. *Proc. SPIE* **2019**, 6. [CrossRef]
18. Loktionova, Y.; Zharkikh, E.; Zherebtsov, E.; Kozlov, I.; Sidorov, V.; Zherebtsova, A.; Sokolovski, S.; Dunaev, A.; Rafailov, E. Wearable laser Doppler sensors for evaluating the nutritive and shunt blood flow. *Proc. SPIE* **2020**. [CrossRef]
19. Zharkikh, E.; Loktionova, Y.; Kozlov, I.; Zherebtsova, A.; Sidorov, V.; Zherebtsov, E.; Dunaev, A.; Rafailov, E. Wearable Laser Doppler Flowmetry for the Analysis of Microcirculatory Changes during Intravenous Infusion in Patients with Diabetes Mellitus. *Proc. SPIE* **2020**, 57. [CrossRef]
20. Mizeva, I.; Dremin, V.; Potapova, E.; Zherebtsov, E.; Kozlov, I.; Dunaev, A. Wavelet Analysis of the Temporal Dynamics of the Laser Speckle Contrast in Human Skin. *IEEE Trans. Biomed. Eng.* **2020**. [CrossRef]
21. Goma, M.; Kimura, Y.; Shimura, H.; Kaneshige, M.; Kobayashi, T.; Kikuchi, M.; Terada, N. Orthostatic response of cephalic blood flow using a mini laser Doppler blood flowmeter and hemodynamics of a new active standing test. *Eur. J. Appl. Physiol.* **2015**, *115*, 2167–2176. [CrossRef] [PubMed]
22. Bivins, H.; Knopp, R.; dos Santos, P.A. Blood volume distribution in the Trendelenburg position. *Ann. Emerg. Med.* **1985**, *14*, 641–643. [CrossRef]
23. Shiogai, Y.; Stefanovska, A.; McClintock, P.V.E. Nonlinear dynamics of cardiovascular ageing. *Phys. Rep.* **2010**, *488*, 51–110. [CrossRef] [PubMed]
24. Martini, R.; Bagno, A. The wavelet analysis for the assessment of microvascular function with the laser Doppler fluxmetry over the last 20 years. Looking for hidden informations. *Clin. Hemorheol. Microcirc.* **2018**, *70*, 213–229. [CrossRef] [PubMed]
25. Hu, H.F.; Hsiu, H.; Sung, C.J.; Lee, C.H. Combining laser-Doppler flowmetry measurements with spectral analysis to study different microcirculatory effects in human prediabetic and diabetic subjects. *Lasers Med. Sci.* **2017**, *32*, 327–334. [CrossRef]
26. Schabauer, A.M.; Rooke, T.W. Cutaneous laser Doppler flowmetry: Applications and findings. In *Mayo Clinic Proceedings*; Elsevier: Amsterdam, The Netherlands, 1994; Volume 69, pp. 564–574. [CrossRef]
27. Farkas, K.; Kolossváry, E.; Járai, Z.; Nemcsik, J.; Farsang, C. Non-invasive assessment of microvascular endothelial function by laser Doppler flowmetry in patients with essential hypertension. *Atherosclerosis* **2004**, *173*, 97–102. [CrossRef] [PubMed]
28. Ninomiya, I.; Fujita, S. Reflex effects of thermal stimulation on sympathetic nerve activity to skin and kidney. *Am. J. Physiol. Leg. Content* **1976**, *230*, 271–278. [CrossRef] [PubMed]
29. Malpas, S.C. Neural influences on cardiovascular variability: Possibilities and pitfalls. *Am. J. Physiol. Heart Circ. Physiol.* **2002**, *282*, H6–H20. [CrossRef] [PubMed]
30. Tigno, X.T.; Ley, K.; Pries, A.R.; Gaehtgens, P. Venulo-arteriolar communication and propagated response. *PflÜGers Arch.* **1989**, *414*, 450–456. [CrossRef]
31. Goltsov, A.; Anisimova, A.V.; Zakharkina, M.; Krupatkin, A.I.; Sidorov, V.V.; Sokolovski, S.G.; Rafailov, E. Bifurcation in blood oscillatory rhythms for patients with ischemic stroke: A small scale clinical trial using laser doppler flowmetry and computational modeling of vasomotion. *Front. Physiol.* **2017**, *8*, 160. [CrossRef]
32. Ikram, M.K.; De Jong, F.J.; Van Dijk, E.J.; Prins, N.D.; Hofman, A.; Breteler, M.M.B.; De Jong, P.T.V.M. Retinal vessel diameters and cerebral small vessel disease: The Rotterdam Scan Study. *Brain* **2006**, *129*, 182–188. [CrossRef]

33. Sharrett, A.R. A Review of Population-Based Retinal Studies of the Microvascular Contribution to Cerebrovascular Diseases. *Ophthalmic Epidemiol.* **2007**, *14*, 238–242. [CrossRef] [PubMed]
34. Cheung, N.; Mosley, T.; Islam, A.; Kawasaki, R.; Sharrett, A.R.; Klein, R.; Coker, L.H.; Knopman, D.S.; Shibata, D.K.; Catellier, D.; et al. Retinal microvascular abnormalities and subclinical magnetic resonance imaging brain infarct: A prospective study. *Brain* **2010**, *133*, 1987–1993. [CrossRef] [PubMed]
35. Anisimova, A.; Krupatkin, A.; Sidorov, V.; Zacharkina, M.; Yutskova, E.; Galkin, S. Laser Doppler flowmetry in the assessment of the microcirculation in patients with acute and chronic cerebrovascular insufficiency. *Reg. Blood Circ. Microcirc.* **2014**, *13*, 31–37. [CrossRef]
36. Izumi, H. Nervous control of blood flow in the orofacial region. *Pharmacol. Ther.* **1999**, *81*, 141–161. [CrossRef]
37. Fedorovich, A.A. Functional State of the Microvascular Bed of the Skin in Essential Arterial Hypertension Assessed by Laser Doppler Flowmetry with Amplitude-Frequency Wavelet Analysis of Blood Flow Oscillations. In *Basic and Clinical Understanding of Microcirculation*; IntechOpen: London, UK, 2019.

diagnostics

MDPI

*Article*

# Laser Doppler Spectrum Analysis Based on Calculation of Cumulative Sums Detects Changes in Skin Capillary Blood Flow in Type 2 Diabetes Mellitus

**Igor Kozlov [1,*], Evgeny Zherebtsov [1,2], Galina Masalygina [3], Konstantin Podmasteryev [1] and Andrey Dunaev [1]**

[1] Research and Development Center of Biomedical Photonics, Orel State University, 302026 Orel, Russia; evgenii.zherebtsov@oulu.fi (E.Z.); asms-orel@mail.ru (K.P.); inohvat@yandex.ru (A.D.)
[2] Optoelectronics and Measurement Techniques Unit, University of Oulu, 90570 Oulu, Finland
[3] Orel Regional Clinical Hospital, 302028 Orel, Russia; kovalina68@ya.ru
* Correspondence: igor57_orel@mail.ru; Tel.: +7-(4862)-41-98-06

**Abstract:** In this article, we introduce a new method of signal processing and data analysis for the digital laser Doppler flowmetry. Our approach is based on the calculation of cumulative sums over the registered Doppler power spectra. The introduced new parameter represents an integral estimation for the redistribution of moving red blood cells over the range of speed. The prototype of the device implementing the technique is developed and tested in preliminary clinical trials. The methodology was verified with the involvement of two age groups of healthy volunteers and in a group of patients with type 2 diabetes mellitus. The main practical result of the study is the development of a set of binary linear classifiers that allow the method to identify typical patterns of the microcirculation for the healthy volunteers and diabetic patients based on the presented diagnostic algorithm.

**Keywords:** laser Doppler flowmetry; non-invasive optical diagnostics; cumulative sum; power spectrum; heating test; diabetes mellitus type 2



**Citation:** Kozlov, I.; Zherebtsov, E.; Masalygina, G.; Podmasteryev, K.; Dunaev, A. Laser Doppler Spectrum Analysis Based on Calculation of Cumulative Sums Detects Changes in Skin Capillary Blood Flow in Type 2 Diabetes Mellitus. *Diagnostics* **2021**, *11*, 267. https://doi.org/10.3390/diagnostics11020267

Academic Editor: Xavier Muñoz-Berbel
Received: 1 December 2020
Accepted: 3 February 2021
Published: 9 February 2021



## 1. Introduction

The blood microcirculation (BM) performs a crucial role for the life support of every type of living tissue in the human body. The BM supports gases and nutrients exchange, delivering of immune cells, and temperature regulation. The BM makes a major contribution to the overall flow resistance of the blood vessels, being the main actor in the regulation of the blood pressure. The functional state of human tissues directly depends on the state of elementary BM units (capillaries, plexus, minor arterioles, and venules). It is well-known [1] that the microcirculatory bed is composed of blood vessels of the certain types with a particular specialisation: arterioles, capillaries, venules and arterio-venular anastomoses (AVA). AVA, together with the smooth muscle structures acts as a physiological valve that redirects the micro blood flow either through the capillary plexus or bypassing one. The process orchestrated by the physiological regulation from the endothelium, neural activity, myogenic contraction and relaxation, as well as by the modulation from the breathing and heart activity creates characteristic patterns of the blood perfusion fluctuations [2,3].

The disruptions in BM significantly contribute to the development of many diseases and syndromes. One of the most common and widespread diseases with a plethora of severe complications affecting BM is diabetes mellitus type 2 (T2DM). According to forecasts, the number of patients with T2DM is projected to constantly grow in the near future to achieve 500 million people by 2030 [4,5]. Common complications of T2DM are ulcers and lesions on the feet and toes, as well as the development of necrosis due to the trophic disorders of the affected tissues. Optical, non-invasive diagnostics offer a good

range of methods for the evaluation of the functional insufficiency in the components of tissue vitality including blood microcirculation system. The methods are based on such approaches as fluorescence spectroscopy [6], diffuse reflectance spectrocopy [7–9], speckle contrast imaging [10], photopletismography [11], videocapillaroscopy [12] and methods based on coherent light scattering and optical coherence tomography [13,14].

One well-established method for the non-invasive measurements of the blood perfusion in vivo is the laser Doppler flowmetry (LDF). The theoretical basis for the technique is based on the statistical analysis of the laser radiation scattered in the scattering medium with the moving light-scattering elements. For the case of the measurements in the living tissue, the static scattering structures are the cells and static tissue layers, whereas the moving particles are the locomotive blood cells in the flowing capillaries and blood microvessels. The subtle frequency shift caused by an optical Doppler effect is usually detected by the couple of photodiodes operating in the photomixing regime [15,16]. This method has a sufficient time resolution and depth of probing (about 1 mm [17]) to register the blood microflow fluctuations of different origin, as well as the average level of blood perfusion. The range of applications of the non-invasive diagnostics by the LDF method covers the topics of relationship between oxygen saturation and blood flow [18], dental pulp blood flow [19], blood flow analysis in cases of type 1 diabetes mellitus [20] and rheumatic diseases [21], combining LDF and endoscopy during surgery interventions [22,23], nonlinear blood flow dynamics analysis in a various application [24,25], analysis of transdermal transport of drugs [26] and registration of arterial hypertension associated changes in microcirculation [27]. Numerically, the resulting value for the blood perfusion in the LDF technique is commonly given by the expression:

$$PU = \int_{f_{min}}^{f_{max}} f \cdot S(f) df, \tag{1}$$

where $S(f)$ is the power spectrum of the photocurrent given as a function of the frequency, $f$; $f_{min}$, $f_{max}$ are the limits of integration over the region of the power spectrum corresponding to the physiological range of the RBC speed in the blood capillaries. In several recent studies, more advanced techniques on the LDF signal processing were presented [28,29]. The power spectrum analysis within selected ranges of integration allowed Fredriksson et al., to estimate the three ranges of RBC speed in the diagnostic volume of a fibre optical probe. Taking into account the RBC speed distribution and light scattering phase function, a similar approach has been applied for the laser Doppler spectrum decomposition [30,31].

From the very early studies on the LDF technique development, it has been revealed that the distribution of the power spectrum amplitudes over the dimension of frequency changes to a considerable degree, and represents the frequency distribution of intensities for the Doppler shifted optical components scattered on moving RBC [32,33]. In many clinical studies, it has been demonstrated that the information is of substantial diagnostic value for the quantitative characterisation of the microcirculation disorders [34–38]. As an example, the LDF signal recorded with the power spectrum integration up to the frequency of 3000 Hz demonstrated a better signal-to-noise ratio and presented overall quality of diagnostics of the dental pulp vitality than using the full range of the bandwidth [39]. The power spectrum properties for the purposes of the verification of the LDF technique were also studied in liquid phantoms where the interrelation between the distribution of the speed of scattering particles with the registered power spectrum of photocurrent from the detector was also confirmed [40]. Also, the effects of local pressure on the optical probe to the skin surface [34] and breath-holding test [41] on the broadening of the Doppler spectra were studied. Despite the recent interest several research groups on the diagnostic potential of LDF measurements with a more sophisticated analysis of the detector power spectrum, the topic has still not been well understood and dealt with in depth.

In that respect, the aim of this study was to elaborate the concept of a new feature space extracted from the Doppler power spectrum that will increase the diagnostic capability of the LDF method for analysis of blood microcirculation disorders in patients with T2DM.

## 2. Materials and Methods

To implement the LDF signal registration, an in-house built setup was designed and tested (Figure 1). The block diagram of the device is shown in Figure 2. Infra-red laser diode (LPS-785-FC, Thorlabs, USA) (1) with a central radiation wavelength of 785 nm was used for the local illumination of the area of interest (AOI) with 2 mW of output light power. The channel of the electronic signal processing consisted of light-to-current converting and amplifying modules (2, 3), low-frequency (4, 5) and high-frequency (6, 7) filters and a unit for the stabilised power supply.

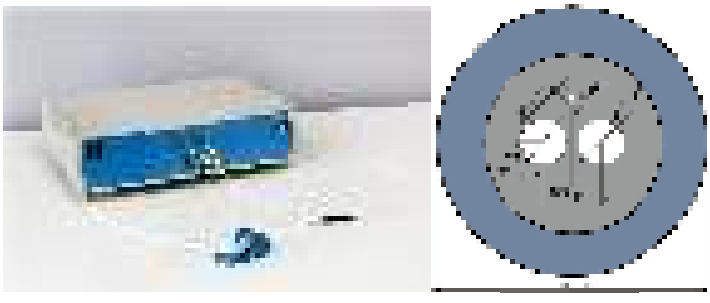

(**a**) (**b**)

**Figure 1.** In-house built prototype of laser Doppler flowmeter with 2 mW of output light power, a signal amplifying, filtration unit, 50 kHz sample rate per channel (**a**) and fibre geometrical configuration (**b**).

The analog-to-digital conversion was implemented by a USB 6211 (National Instruments™,Austin, Texas, USA) data acquisition board (8) with a sampling rate of 50 kHz per channel. LabVIEW™-based PC application (9) was developed for the device control, data acquisition and pre-processing. The period of cycle with the recording of time series containing 2500 data points of photocurrent and the power spectrum calculation was set to be 0.05 s, with the corresponding sampling rate of 20 Hz for the output calculated perfusion. The cut-off frequency for the calculation of the power spectrum was set to 12,800 Hz with the possible increase of this parameter up to the Nyquist frequency limit.

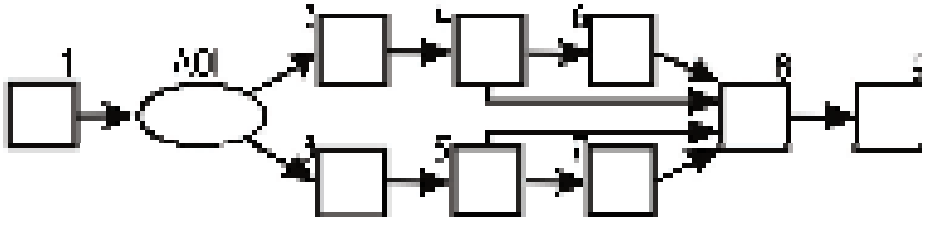

**Figure 2.** The schematic diagram of the developed laser Doppler flowmetry measuring setup. 1— infrared laser diode; 2, 3—light-to-current conversion and amplification modules; 4, 5—low-frequency filters; 6, 7—high-frequency filters; 8—data acquisition board; 9—PC with LabVIEW-based application.

For the blood perfusion calculations over the sub-regions of the power spectrum, the following expression has been used:

$$PU = \frac{K}{i_{dc}^2} \int_{f_{min}}^{f_{max}} f \cdot S(i_{ac2}(t) - i_{ac1}(t))df, \tag{2}$$

where $K$—the static coefficient of gain; $i_{dc}(t)$—the d.c. component of the photocurrent; $i_{ac1}(t)$, $i_{ac2}(t)$—the a.c. components of the photocurrents in the two input photo-detecting sub-channels (the implementation of the differential measuring technique with the subtraction of $i_{ac1}(t)$ and $i_{ac2}(t)$ significantly reduces the motion artefacts from the fibre optical probe); $S$—the procedure of the power spectrum calculation from the accumulated array of the subtracted values of $i_{ac1}(t)$ and $i_{ac2}(t)$. The key functionality of the developed software was the ability to save on disk the calculated power spectra for every sample for further post-processing.

In addition to conventional perfusion units, an estimation of the blood cell speed $\langle v \rangle$ [42] was conducted during the data analysis. The parameters were calculated according to the following equation:

$$\langle v \rangle = \frac{\int_{f_{min}}^{f_{max}} f \cdot S(i_{ac2}(t) - i_{ac1}(t))df}{\int_{f_{min}}^{f_{max}} S(i_{ac2}(t) - i_{ac1}(t))df}. \tag{3}$$

Parameter $\langle v \rangle$ is described as the ratio of conventional perfusion parameter to concentration of moving red blood cells (CMBC) [43] estimated by the Doppler power spectrum, and is general expressed in arbitrary units.

For the validation of the experimental setup, preliminary measurements have been done with the participation of healthy volunteers. The developed and implemented signal processing approach allowed us to reliably register and visualise (Figure 3) the effect of redistribution of the power spectrum signal due to the changes in the distribution of the RBCs speed in blood capillaries during a breath-holding test (BHT) [44]. In the middle of a deep breath, the level of the skin blood perfusion evaluated in the low-frequency range (60–400 Hz) increased prominently, while the overall blood perfusion figured out by the integration in the range of 60–6400 Hz decreased. The result is explained by the slowing down of the bulk of RBC during the procedure of the deep breath-holding causing the shift of the power spectrum to the region of the lower frequencies.

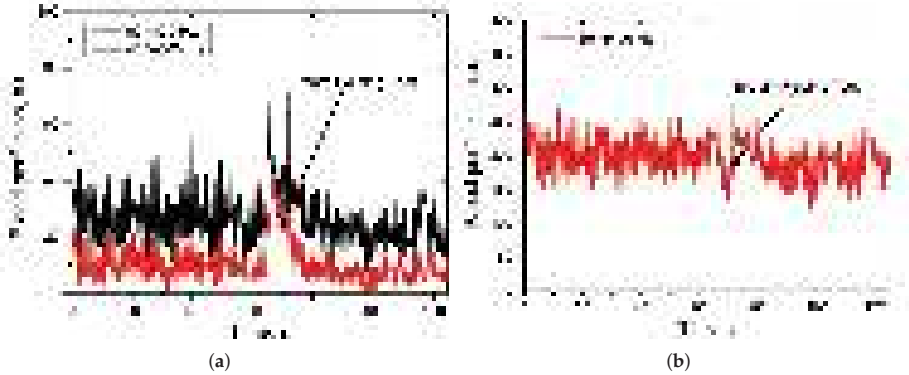

(**a**) (**b**)

**Figure 3.** Registered skin blood perfusion during the breath-holding test evaluated by the integration in the sub-ranges of the photocurrent power spectrum. (**a**): blood perfusion from the low frequency range (60–400 Hz: red; 400–800 Hz-black); (**b**): blood perfusion from the broader frequency range (60–6400 Hz).

### *2.1. Research Protocol*

The developed measuring setup has been validated in the frame of limited clinical studies with the involvement of patients with diabetic disorders. Thermal stimuli applied to the skin has been used to implement a study protocol, benefiting the most from the developed signal processing approach. The heat test is widely used in diagnostics of disorders associated with the regulation of blood perfusion. Moderate heating of the skin to the temperatures between 41–43 °C provokes activation of nociceptive C-fibres [45] and induces the release of nitric oxide [46] from the endothelial layer of vessels. The effect of the stimuli results in the increase of the skin blood perfusion and modulation of its oscillations. T2DM is often associated with an impairment in the response of blood perfusion on the thermal stimuli. The provocation test can also be applied together with a multi-modal approach that combines several measuring techniques such as laser Doppler flowmetry, diffuse reflectance measurements, or fluorescence spectroscopy [6]. Skin temperature dynamics during the skin heating has a significant diagnostic value, being supplemented with the blood perfusion measurements [47]. The fibre optic probe of the developed prototype of laser Doppler flowmeter with the bespoke signal processing algorithm was placed on the dorsal surface of the foot, and coaxially combined with attachment Figure 4 for the heating and cooling tests containing Peltier element with water cooling.

Reliable fixation on the probe on the foot was carried out using several mesh bandages. The measurements were taken 2 h after a meal and caffeine intake. The volunteers were acclimatised for at least 15 min to the conditions of the room where the measurements were conducted.

At the first stage (further on referred as stage 1), blood perfusion was recorded at a temperature of 33 °C for 10 min, to equalise the temperature conditions of the experiment for all subjects. At the second stage (in the text referred to as stage 2), the temperature was increased sequentially at a rate of 2 °C per min to 42 °C for 5 min. At the third stage (referred to below as stage 3), blood perfusion and effects occurring in the capillary blood flow due to heating were recorded for 3 min (Figure 5).

**Figure 4.** Allocation of the fibre optical probe combined with the attachment for the heat and cooling tests on the dorsal surface of foot. 1—fibre optical probe; 2—the attachment for the heating and cooling tests (contains Peltier element with water cooling).

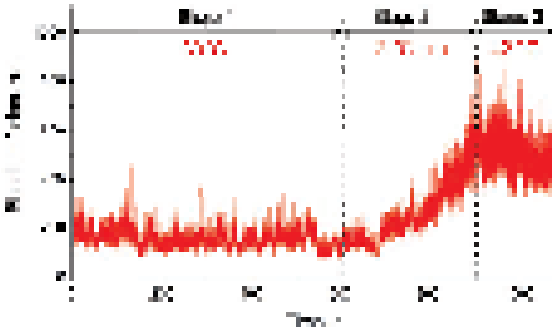

**Figure 5.** An exemplary trace of the blood perfusion during the implemented research protocol.

The cohort of conditionally healthy volunteers was divided into two groups consisting of 7 non-smoking volunteers aged 22 ± 0.5 years and (referred to as group 1) 6 volunteers (with 1 smoking person) aged 51 ± 6 (referred to as group 2), respectively. The group of patients comprised of 10 non-smoking volunteers aged 61 ± 7 with type 2 diabetes confirmed during for at least 5 years , but without diabetic foot, necrosis and visible lesions and characteristics described in Table 1.

All experiments were carried out at a temperature of 21–23 degrees, at a distance of 1 m from heat sources. Studies in patients and volunteers were conducted with the mandatory obtaining of informed consent for the participation in the study. The research protocol was approved by the Institutional ethical committee of Orel State University (Minutes No. 15 dated 21 February 2019).

**Table 1.** Characteristics of T2DM patients and volunteers.

| Parameters | Patients | Group 1 | Group 2 |
|---|---|---|---|
| Age (y) | 61 ± 7 * | 22 ±0.5 * | 51 ± 6 * |
| Sex (M/F) | 3/7 | 2/5 | 3/3 |
| Systolic BP (mmHg) | 125 ± 11 | 122 ± 8 | 120 ± 5 |
| Diastolic BP (mmHg) | 75 ± 7 | 70 ± 3 | 77 ± 4 |
| Body mass index (kg/m$^2$) | 31 ± 4.5 * | 24 ± 3.5 | 25 ± 3.8 |
| Fasting glucose (mmol/L) | 10.4 ± 3 | - | - |
| Diabetes duration (y) | 11.5 ± 4 | - | - |
| HbA1c (%) | 7.1 ± 0.2 | - | - |
| Total cholesterol (mmol/L) | 5.2 ± 0.8 | - | - |
| Creatinine (μmol/L) | 78.6 ± 7.6 | - | - |
| Urea (mmol/L) | 6 ± 0.9 | - | - |
| ALT (IU/L) | 24.9 ± 5.4 | - | - |
| AST (IU/L) | 19.9 ± 4.3 | - | - |

Note: Data in the columns is represented as mean ± SD except Sex parameter. Reference values of the laboratory: HbA1c 4.0% to 6.0%, total cholesterol 3.5 to 5.0 mmol/L, urea 2.5 to 7.5 mmol/L, creatinine 70 to 110 μmol/L, ALT 10 to 38 IU/L, and AST 10 to 40 IU/L. *—denotes a statistical difference identified by Mann-Whitney test between two other groups, $p < 0.05$.

### *2.2. Data Processing*

For the study, a novel approach was applied that previously was not used for signal processing in LDF. The implemented LDF channel (Figure 1) during the measuring procedure recorded the raw data with the power spectra from the photodiodes and performed blood perfusion calculation based on those measurements. To analyse the changes in a response to the applied functional tests, cumulative sum curves were calculated at the stage of post-processing by the following steps. Firstly, power spectra weighted by the

frequency were calculated. Secondly, cumulative sum curves for every weighted power spectrum in samples were calculated according to the following recursive expression:

$$C_n = C_{n-1} + \frac{f_n \cdot S(f_n)}{\sum f_i \cdot S(f_i)}, \tag{4}$$

where $C_n$—a cumulative sum of the series from one to $n$; $C_0 = 0$; $f_n \cdot S(f_n)$—perfusion calculated for the frequency bin $n$; $\sum f_i \cdot S(f_i)$—perfusion calculated over all frequencies; $n$ is changed in range from 1 to 640 that equals a frequency range from 0 to 12,800 Hz. Thirdly, the average cumulative sum curve is calculated for a specified period of the perfusion recording. $C_n$ is a value that represents what part of the signal is localised before the certain frequency. The shape of the cumulative sum curve depends on the distribution of the signal over the frequencies of Doppler broadening. The expression (3) can be expressed in an integral form that resembles Equation (1):

$$C_n = \frac{\int_{f_{min}}^{f_n} f \cdot S(f) df}{\int_{f_{min}}^{f_{max}} f \cdot S(f) df}, \tag{5}$$

where $f_n$ is the frequency of the $n$-th frequency bin. The processing of the data obtained in the standard occlusion test demonstrates the sensitivity of the calculated $C_n$ parameter to the changes in skin blood perfusion during the occlusion stage and stage of post-occlusive reactive hyperaemia (Figure 6).

The cumulative sum curve for the signal recording when occlusion is applied is growing faster. During the occlusion, there is a shift of the localisation of the signal to the low frequency band. Also the overall shape of the cumulative sum curve changes. To quantify the redistribution of the signal over the frequency subbands before and after provocative test, we calculate the parameter of the area enclosed between the two cumulative sum curves.

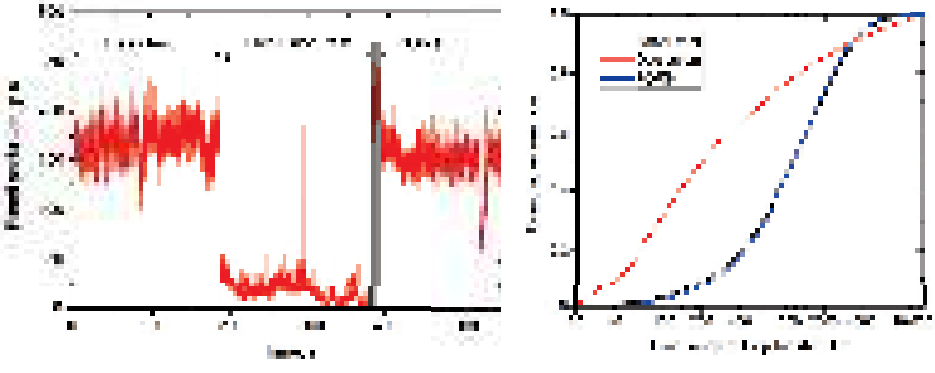

(**a**) (**b**)

**Figure 6.** Cumulative sum curves calculated for the main stages of occlusion test. (**a**)—representative trace of the evaluated blood perfusion during the occlusion test; (**b**)—cumulative sum curves calculated for the stages of the occlusion test.

An example of the two curves calculated for stage 1 and stage 3 of the described protocol (Figure 5) implemented in patients is shown in Figure 7, where the purple highlighted area represents the introduced parameter, further called Area between Curves (AbC). The AbC parameter is calculated for the area between the curves from starting frequency

to the first intersection of the curves. The area after the intersection is not included in the calculation.

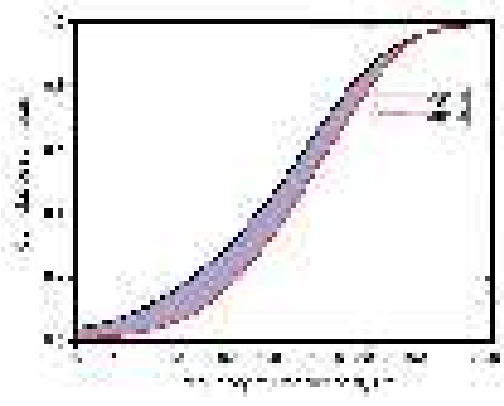

**Figure 7.** Representative example of cumulative sum curves and analysed area between them (highlighted in purple) for the stages 1 and 3 of the implemented research protocol with thermal stimuli applied to the skin

It is known that the shape of a first moment of the power spectrum depends on the speed of moving red blood cells. However, it remains unclear which mechanisms are more responsible for perfusion alterations during functional tests—a proportional increase in amplitude or changes in the shape of weighted power spectra.

The second informative parameter used in the data analysis was the difference between averaged blood perfusion values calculated for stage 3 and stage 1 (subsequently called the DBP parameter):

$$DBP = \langle PU \rangle_{stage3} - \langle PU \rangle_{stage1}, \tag{6}$$

where $\langle \dots \rangle$—symbol of averaging by time. The DBP parameter is often used in studies as a parameter characterising functional state of the microvascular regulation [20,48]. Also, the average RBC speed calculated according the expression (4) was estimated for the analysed stages 1 and 3:

$$\langle v \rangle_{31} = \langle v \rangle_3 - \langle v \rangle_1, \tag{7}$$

where $\langle v \rangle_1$ and $\langle v \rangle_3$ — average estimation of blood cell speed calculated by whole duration of stage 1 and stage 3 correspondingly.

## 3. Results

The approach of the cumulative sum curve analysis is intended to demonstrate that mean perfusion changes under thermal stimuli may have different characteristics from volunteer to volunteer in the context of power spectral distribution. Using the two parameters AbC and DBP as a feature space, two binary linear classifiers based on linear discriminant analysis (LDA) were implemented to distinguish the group of patients and the group of volunteers 2, ($Y1$) as well as the groups of volunteers 1 and 2 ($Y2$) (Figure 8).

The calculated discriminant functions have been identified to have the following form:

$$Y1 = -5.0622 + 0.84 \cdot X1_{2p} + 0.0177 \cdot X2_{2p}$$
$$Y2 = -4.28022 + 0.86 \cdot X1_{12} + 0.0076 \cdot X2_{12}$$

Table 1 shows the area under curve (AUC) values for the classifiers based on the discriminant functions calculated using only one of the two input parameters and for their combined use.

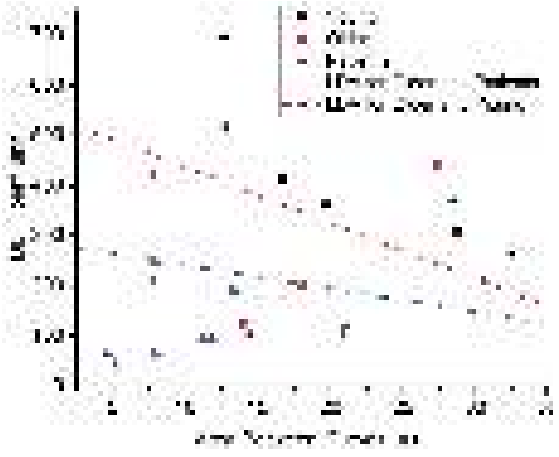

**Figure 8.** Scatter plots for analysed groups of patients and volunteers with the dividing lines of the LDA classifiers.

The scatter plots for the collected data in Figure 8 are divided into three areas. The first one, the lower-left corner of Figure 8 is represented by the group of patients. Group 1 and group 2 occupied the intermediate position and the upper-right corner, respectively. Group 2 and some individuals from the patient group are characterised by a high DPB parameter. Other individuals showed a relatively high value of the AbC parameter.

## 4. Discussion

The observed effects are potentially connected with the presence of two ways of mean blood perfusion increase. One of them occurs when the value of the AbC parameter is relatively high. Apparently, the increase in mean blood perfusion is connected with the redistribution of the spectrum amplitude to higher frequencies of Doppler broadening. Whereas, if the DBP parameter increases and the AbC parameter is small, then the blood perfusion changes due to a proportional amplification in the spectrum amplitudes, which will not drastically change the shape of the cumulative sum curves. Thus, the shape of the cumulative sum curve calculated during stage 3 is changed weakly. Consequently, the AbC parameter does not substantially increase. Group 1 is characterised by both mechanisms: a sufficient broadening of the spectrum, and a significant DBP parameter. In the case of group 2, the trend is not recognised. However, group 2 is characterised by reduced values of the DBP and significantly high scattering values relative to the AbC parameter. As for the patient group, both parameters are significantly reduced.

Variations in the AbC parameter can be associated with various factors. The article [49] presents the results of modelling the distribution of photons over the Doppler shift frequencies taking into account changes in both the speed of scattering particles and their concentration. The simulation results show that both of these parameters simultaneously influence the shape of the Doppler spectra. Indeed, during the thermal test, both an increase in the RBC concentration and a change in their average rate can occur. Moreover, article [30] described that the shape of power spectra depends on a distribution characteristic of RBC speed. It is difficult to say with complete certainty which of the described factors is decisive for a particular functional test in healthy volunteers.Further research and modelling is required since Figure 8 shows a substantial variation of the results from healthy volunteers. However, for patients with type 2 diabetes mellitus, it is important to note that changes in the shape of the power spectra in response to the heat test are weak in comparison with cohorts of healthy volunteers, which is demonstrated by the AbC.

Power spectrum shape-changing (consequently, changes in cumulative sum curves) can occur for several reasons. It was previously described that severe geometric shape

changing in capillary loops happens in patients with T2DM [50]. On the example of nailfold capillaroscopy, giant capillaries, and an increase of the distance between capillaries, the appearance of convoluted and intersecting capillaries are shown. The article [51] described the speed of distribution in a healthy capillary loop. To the best of our knowledge, such a numerical experiment for pathological capillaries did not perform. However, in the presence of sharp turns, bends and intersections in a capillary loop, the blood flow will differ substantially from laminar flow. The diameter of capillaries and its influence on power spectra is also considered by Fredriksson et al. [52]. Possibly, the cross-section of capillary loops in patients with T2DM is larger than in healthy volunteers. Thus, a change in the geometric shape of the capillaries, the cross-section and a decrease in their number [53] lead to phenomena where an increase in blood perfusion occurs only due to a proportional increase in the power spectrum amplitudes with relatively constant overall shape of the function. From a clinical point of view, the low-values of parameters AbC and DBP in the cohort of patients can be observed due to the decreasing of capillary loop quantity and pathological changes in the capillaries where the RBC speed profile changes slightly during the applied thermal stimuli.

Thus, introduced in this study, AbC parameter is a novel approach for LDF signal processing. As seen for group 1 and 2 in Table 2, combined use of the parameters significantly increases the prediction value in comparison with the classifiers built using the parameters separately.

To date, there are several methods for recording speed-resolved blood perfusion. For example, PeriFlux 6000 EPOS (Perimed, Järfälla, Sweden) enable simultaneously registering blood perfusion in the frame of three speed ranges. This approach is based on a mathematical model that takes into account the concentration of RBC, blood oxygenation, the potential geometric shapes of capillaries, as well as the optical properties of biological tissues under study. These capabilities are achieved by combining the LDF with the diffuse reflectance spectroscopy measuring channel. A series of studies were made using that technique, for example by Wang et al. [54]. Nevertheless, the current study approach can be implemented using hardware of both classical LDF devices and ones implementing more advanced techniques with recording speed-resolved blood perfusion, supplementing the present arsenal of the signal processing methods in the field.

Calculated AUC-scores of $\langle v \rangle$-based classifiers and classifier with extended feature space for three involved parameters for group 2 vs. patients and group 1 vs. group 2 is shown in Table 2. The combined use of the three parameters augmented with parameter of blood perfusion improves the classification between the compared groups. The proposed estimates represent different aspects of blood perfusion and complement each other.

Thus, the introduced AbC parameter can be used for the interpretation of the origin of observing alterations in mean blood perfusion indicating whether the changes are due to the RBC speed redistribution, or due to the proportional increase in all components of blood perfusion. The AUC-score for the classifier between aged healthy volunteers and patients is of almost the same value as for using a single DBP parameter, which can also be explained by the limited size of the tested cohort of volunteers. Identification of factors, which affect the shape of perfusion distribution by Doppler frequencies, can be of particular interest in the diagnostics of disorders characterised by changes in blood perfusion. It is important to note that the cumulative sum-based estimations such as Area between Curves can be combined with conventional perfusion measurements (CMBC and blood cell speed $\langle v \rangle$). As is shown on Table 2, the combination of the proposed and conventional parameters is better suited for classification for both considered pairs.

The proposed approach can find applications in clinical practice and diagnostics without significant modifications of the standard configuration of LDF channel, facilitating the translation of the study results in routine diagnostics procedures.

**Table 2.** AUC-scores for the tested classifiers for the groups of volunteers and patients.

| Classifiers | AUC |
|---|---|
| Group 1 vs. Group 2 | |
| DBP classifier | 0.76 |
| AbC classifier | 0.64 |
| $\langle v \rangle_{31}$ classifier | 0.79 |
| Linear classifier (DBP and AbC together) | 0.86 |
| Linear classifier (DBP and $\langle v \rangle_{31}$ together) | 0.91 |
| Complex classifier (DBP, AbC, $\langle v \rangle_{31}$) | 0.928 |
| Group 2 vs. Patients | |
| DBP classifer | 0.92 |
| AbC classifer | 0.65 |
| $\langle v \rangle_{31}$ classifier | 0.71 |
| Linear classifier (DBP and AbC together) | 0.9 |
| Linear classifier (DBP and $\langle v \rangle_{31}$ together) | 0.91 |
| Complex classifier (DBP, AbC, $\langle v \rangle_{31}$) | 0.933 |

## 5. Conclusions

In the study, the measurement of perfusion is complemented by a new parameter based on the calculation of cumulative sums from the power spectrum of the photodetector signals. The described diagnostic approach allows for revising the known protocols for characterising blood microcirculation parameters based on LDF measurements. In the context of the proposed signal processing technique, a new feature space can be added to the set of known diagnostic parameters expanding the range of applications for the LDF. The translation of the study results suggests that routine diagnostics procedures do not require significant modifications of the standard configuration of LDF channel. Also, the method does not involve any additional measurement channels (fluorescence, diffuse reflectance spectroscopy, and others) that still demonstrate relatively high accuracy of classification for the diagnostics of impaired blood microcirculation, even being tested in a limited size of the cohort of patients with T2DM.

**Author Contributions:** I.K.: experimental studies, data processing, signal processing, drafting the manuscript. E.Z.: co-supervising, the concept and implementation of the measuring setup, drafting the manuscript, data analysis, funding acquisition. G.M.: the research protocol, experimental studies in hospital. K.P.: finalizing the article; A.D.: supervising, study conceptualisation, discussion, funding acquisition. All authors edited manuscript. All authors have read and agreed to the published version of the manuscript.

**Funding:** The reported study was funded by the Russian Foundation for Basic Research (RFBR), project numbers 19-32-90253. E. Zherebtsov acknowledges the funding from the Academy of Finland (grant number 318281, data analysis) and Russian Science Foundation (grant number 20-75-00123, development of the experimental setup).

**Institutional Review Board Statement:** The study was conducted according to the guidelines of the Declaration of Helsinki, and approved by the Ethics Committee of Orel State University (Minutes No. 15 dated 21 February 2019).

**Informed Consent Statement:** Informed consent was obtained from all subjects involved in the study.

**Conflicts of Interest:** The authors declare no conflict of interest.

## References


1. Braverman, I.M. The Cutaneous Microcirculation: Ultrastructure and Microanatomical Organization. *Microcirculation* **1997**, *4*, 329–340. [CrossRef]
2. Stefanovska, A.; Bracic, M.; Kvernmo, H.D. Wavelet analysis of oscillations in the peripheral blood circulation measured by laser Doppler technique. *IEEE Trans. Biomed. Eng.* **1999**, *46*, 1230. [CrossRef]
3. Kvandal, P.; Landsverk, S.; Bernjak, A.; Stefanovska, A.; Kvernmo, H.; Kirkebøen, K. Low-frequency oscillations of the laser Doppler perfusion signal in human skin. *Microvasc. Res.* **2006**, *72*, 120. [CrossRef]
4. Rowley, W.R.; Bezold, C.; Arikan, Y.; Byrne, E.; Krohe, S. Diabetes 2030: Insights from Yesterday, Today, and Future Trends. *Popul. Health Manag.* **2017**, *20*, 6–12. [CrossRef]
5. Ogurtsova, K.; da Rocha Fernandes, J.D.; Huang, Y.; Linnenkamp, U.; Guariguata, L.; Cho, N.H.; Cavan, D.; Shaw, J.E.; Makaroff, L.E. IDF Diabetes Atlas: Global estimates for the prevalence of diabetes for 2015 and 2040. *Diabetes Res. Clin. Pract.* **2017**, *128*, 40–50. [CrossRef]
6. Dremin, V.V.; Zherebtsov, E.A.; Sidorov, V.V.; Krupatkin, A.I.; Makovik, I.N.; Zherebtsova, A.I.; Zharkikh, E.V.; Potapova, E.V.; Dunaev, A.V.; Doronin, A.A.; et al. Multimodal optical measurement for study of lower limb tissue viability in patients with diabetes mellitus. *J. Biomed. Opt.* **2017**, *22*, 1–10. [CrossRef]
7. Potapova, E.V.; Dremin, V.V.; Zherebtsov, E.A.; Makovik, I.N.; Zherebtsova, A.I.; Dunaev, A.V.; Podmasteryev, K.V.; Sidorov, V.V.; Krupatkin, A.I.; Khakhicheva, L.S.; et al. Evaluation of microcirculatory disturbances in patients with rheumatic diseases by the method of diffuse reflectance spectroscopy. *Hum. Physiol.* **2017**, *43*. [CrossRef]
8. Jonasson, H.; Fredriksson, I.; Bergstrand, S.; Östgren, C.J.; Larsson, M.; Strömberg, T. In vivo characterization of light scattering properties of human skin in the 475- to 850-nm wavelength range in a Swedish cohort. *J. Biomed. Opt.* **2018**, *23*. [CrossRef] [PubMed]
9. Fredriksson, I.; Larsson, M.; Strömberg, T. Machine learning for direct oxygen saturation and hemoglobin concentration assessment using diffuse reflectance spectroscopy. *J. Biomed. Opt.* **2020**, *25*, 1–16. [CrossRef] [PubMed]
10. Hultman, M.; Larsson, M.; Strömberg, T.; Fredriksson, I. Real-time video-rate perfusion imaging using multi-exposure laser speckle contrast imaging and machine learning. *J. Biomed. Opt.* **2020**, *25*, 1–15. [CrossRef] [PubMed]
11. Volkov, M.V.; Margaryants, N.B.; Potemkin, A.V.; Volynsky, M.A.; Gurov, I.P.; Mamontov, O.V.; Kamshilin, A.A. Video capillaroscopy clarifies mechanism of the photoplethysmographic waveform appearance. *Sci. Rep.* **2017**, *7*, 13298. [CrossRef] [PubMed]
12. Dremin, V.; Kozlov, I.; Volkov, M.; Margaryants, N.; Potemkin, A.; Zherebtsov, E.; Dunaev, A.; Gurov, I. Dynamic evaluation of blood flow microcirculation by combined use of the laser Doppler flowmetry and high-speed videocapillaroscopy methods. *J. Biophotonics* **2019**, *12*, e201800317. [CrossRef]
13. de Carlo, T.E.; Romano, A.; Waheed, N.K.; Duker, J.S. A review of optical coherence tomography angiography (OCTA). *Int. J. Retin. Vitr.* **2015**, *1*, 5. [CrossRef]
14. Shu, X.; Beckmann, L.J.; Zhang, H.F. Visible-light optical coherence tomography: A review. *J. Biomed. Opt.* **2017**, *22*, 1–14. [CrossRef] [PubMed]
15. Forrester, A.T. Photoelectric Mixing As a Spectroscopic Tool. *J. Opt. Soc. Am.* **1961**, *51*, 253–259. [CrossRef]
16. Cummins, H.Z.; Swinney, H.L. III light beating spectroscopy. In *Progress in Optics*; Wolf, E., Ed.; Elsevier: Amsterdam, The Netherlands, 1970; Volume 8, pp. 133–200.
17. Humeau-Heurtier, A.; Mahe, G.; Durand, S.; Abraham, P. Skin perfusion evaluation between laser speckle contrast imaging and laser Doppler flowmetry. *Opt. Commun.* **2013**, *291*, 482–487. [CrossRef]
18. Wang, G.; Jia, S.; Liu, M.; Song, X.; Li, H.; Chang, X.; Zhang, W. Impact of local thermal stimulation on the correlation between oxygen saturation and speed-resolved blood perfusion. *Sci. Rep.* **2020**, *10*. [CrossRef]
19. Dzeletovic, B.; Stratimirovic, D.; Stojic, D.; Djukic, L. Linear and nonlinear analysis of dental pulp blood flow oscillations in ageing. *Int. Endod. J.* **2020**, *53*, 1033–1039. [CrossRef]
20. Sorelli, M.; Francia, P.; Bocchi, L.; De Bellis, A.; Anichini, R. Assessment of cutaneous microcirculation by laser Doppler flowmetry in type 1 diabetes. *Microvasc. Res.* **2019**, *124*, 91–96. [CrossRef] [PubMed]
21. Mizeva, I.; Makovik, I.; Dunaev, A.; Krupatkin, A.; Meglinski, I. Analysis of skin blood microflow oscillations in patients with rheumatic diseases. *J. Biomed. Opt.* **2017**, *22*, 1–3. [CrossRef]
22. Berge, S.T.; Safi, N.; Medhus, A.W.; Ånonsen, K.; Sundhagen, J.O.; Hisdal, J.; Kazmi, S.S.H. Gastroscopy assisted laser Doppler flowmetry and visible light spectroscopy in patients with chronic mesenteric ischemia. *Scand. J. Clin. Lab. Investig.* **2019**, *79*, 541–549. [CrossRef]
23. Zherebtsov, E.; Zajnulina, M.; Kandurova, K.; Potapova, E.; Dremin, V.; Mamoshin, A.; Sokolovski, S.; Dunaev, A.; Rafailov, E.U. Machine Learning Aided Photonic Diagnostic System for Minimally Invasive Optically Guided Surgery in the Hepatoduodenal Area. *Diagnostics* **2020**, *10*. [CrossRef] [PubMed]
24. Liao, F.; Jan, Y.K. Nonlinear dynamics of skin blood flow response to mechanical and thermal stresses in the plantar foot of diabetics with peripheral neuropathy. *Clin. Hemorheol. Microcirc.* **2017**, *66*, 197–210. [CrossRef] [PubMed]

25. Sorelli, M.; Perrella, A.; Francia, P.; De Bellis, A.; Anichini, R.; Bocchi, L. Multi-gaussian Decomposition of the Microvascular Pulse Detects Alterations in Type 1 Diabetes BT. In Proceedings of the World Congress on Medical Physics and Biomedical Engineering 2018, Prague, Czech Republic, 3–8 June 2018; Lhotska, L., Sukupova, L., Lacković, I., Ibbott, G.S., Eds.; Springer: Singapore, 2019; pp. 173–176.
26. Vandersee, S.; Erdmenger, U.; Patzelt, A.; Beyer, M.; Meinke, M.; Darvin, M.; Koscielny, J.; Lademann, J. Significance of the follicular pathway for dermal substance penetration quantified by laser Doppler flowmetry. *J. Biophotonics* **2016**, *9*, 276–281. [CrossRef] [PubMed]
27. Yuan, X.; Wu, Q.; Shang, F.; Li, B.; Liu, M.; Wang, B.; Sheng, Y.; Zhang, H.; Xiu, R. A comparison of the cutaneous microvascular properties of the Spontaneously Hypertensive and the Wistar-Kyoto rats by Spectral analysis of Laser Doppler. *Clin. Exp. Hypertens.* **2019**, *41*, 342–352. [CrossRef] [PubMed]
28. Fredriksson, I.; Larsson, M.; Strömberg, T. Model-based quantitative laser Doppler flowmetry in skin. *J. Biomed. Opt.* **2010**, *15*, 57002–57012. [CrossRef]
29. Jonasson, H.; Fredriksson, I.; Larsson, M.; Strömberg, T. Validation of speed-resolved laser Doppler perfusion in a multimodal optical system using a blood-flow phantom. *J. Biomed. Opt.* **2019**, *24*, 1–8. [CrossRef]
30. Wojtkiewicz, S.; Liebert, A.; Rix, H.; Maniewski, R. Evaluation of algorithms for microperfusion assessment by fast simulations of laser Doppler power spectral density. *Phys. Med. Biol.* **2011**, *56*, 7709. [CrossRef]
31. Liebert, A.; Zolek, N.; Wojtkiewicz, S.; Maniewski, R. Estimation of Speed Distribution of Particles Moving in an Optically Turbid Medium Using Decomposition of a Laser-Doppler Spectrum. In Proceedings of the 2007 29th Annual International Conference of the IEEE Engineering in Medicine and Biology Society, Lyon, France, 23–26 August 2007; pp. 4080–4082.
32. Bonner, R.; Nossal, R. Model for laser Doppler measurements of blood flow in tissue. *Appl. Opt.* **1981**, *20*, 2097–2107. [CrossRef]
33. Nilsson, G.E.; Tenland, T.; Oberg, P.A. Evaluation of a Laser Doppler Flowmeter for Measurement of Tissue Blood Flow. *IEEE Trans. Biomed. Eng.* **1980**, *BME-27*, 597–604. [CrossRef]
34. Zherebtsov, E.; Kandurova, K.; Seryogina, E.; Kozlov, I.; Dremin, V.; Zherebtsova, A.; Dunaev, A.; Meglinski, I. The influence of local pressure on evaluation parameters of skin blood perfusion and fluorescence. In *Progress in Biomedical Optics and Imaging—Proceedings of SPIE*; SPIE: Bellingham, WA, USA, 2017; Volume 10336. [CrossRef]
35. Kozlov, I.O.; Zherebtsov, E.A.; Dremin, V.V.; Zherebtsova, A.I.; Zharkikh, E.V.; Dunaev, A.V.; Rafailov, E.U. Laser doppler spectrum decomposition applied in diagnostics of microcirculatory disturbances. In *Biophotonics: Photonic Solutions for Better Health Care VI*; Popp, J., Tuchin, V.V., Pavone, F.S., Eds.; International Society for Optics and Photonics (SPIE): Bellingham, WA, USA, 2018; Volume 10685, pp. 735–738. [CrossRef]
36. Kozlov, I.; Zherebtsov, E.; Zherebtsova, A.; Dremin, V.; Dunaev, A. Investigation of Doppler spectra of laser radiation scattered inside hand skin during occlusion test. *J. Phys. Conf. Ser.* **2017**, *929*, 012063. [CrossRef]
37. Fredriksson, I.; Hultman, M.; Strömberg, T.; Larsson, M. Machine learning in multiexposure laser speckle contrast imaging can replace conventional laser Doppler flowmetry. *J. Biomed. Opt.* **2019**, *24*, 1–11. [CrossRef] [PubMed]
38. Wojtkiewicz, S.; Wojcik-Sosnowska, E.; Jasik, M.; Maniewski, R.; Karnafel, W.; Liebert, A. Assessment of speed distribution of red blood cells in the microvascular network in healthy volunteers and type 1 diabetes using laser Doppler spectra decomposition. *Physiol. Meas.* **2014**, *35*, 283–295. [CrossRef]
39. Qu, X.; Ikawa, M.; Shimauchi, H. Improvement of the detection of human pulpal blood flow using a laser Doppler flowmeter modified for low flow velocity. *Arch. Oral Biol.* **2014**, *59*, 199–206. [CrossRef]
40. Chen, Y.Y.; Lin, Y.H.; Jan, I.C.; Liu, R.S.; Chou, N.K.; Jan, G.J. Adaptive processing bandwidth adjustment for laser Doppler flowmetry. *Med. Biol. Eng. Comput.* **2004**, *42*, 277–281. [CrossRef]
41. Dremin, V.V.; Zherebtsov, E.A.; Makovik, I.N.; Kozlov, I.O.; Sidorov, V.V.; Krupatkin, A.I.; Dunaev, A.V.; Rafailov, I.E.; Litvinova, K.S.; Sokolovski, S.G.; et al. Laser Doppler flowmetry in blood and lymph monitoring, technical aspects and analysis. *Proc. SPIE* **2017**, *10063*, 1006303–1006308.
42. Malanin, K.; Havu, V.K.; Kolari, P.J. Dynamics of Cutaneous Laser Doppler Flux with Concentration of Moving Blood Cells and Blood Cell Velocity in Legs with Venous Ulcers and in Healthy Legs. *Angiology* **2004**, *55*, 37–42. [CrossRef] [PubMed]
43. Karlsson, D.M.G.; Larsson, M.; Stroemberg, T.; Wardell, K. Influence of tissue movements on laser Doppler perfusion imaging. In *Optical Diagnostics and Sensing of Biological Fluids and Glucose and Cholesterol Monitoring II*; Priezzhev, A.V., Cote, G.L., Eds.; International Society for Optics and Photonics (SPIE): Bellingham, WA, USA, 2002; Volume 4624, pp. 106–114. [CrossRef]
44. Bodo, M.; Mahon, R.; Razumovsky, A.; Kouperberg, E.; Crimmins, M.; Armonda, R.; Baruch, M. Comparison of cerebrovascular reactivity tests: A pilot human study. *J. Electr. Bioimpedance* **2019**, *8*, 25–33. [CrossRef]
45. Lenoir, C.; Plaghki, L.; Mouraux, A.; van den Broeke, E.N. Quickly responding C-fibre nociceptors contribute to heat hypersensitivity in the area of secondary hyperalgesia. *J. Physiol.* **2018**, *596*, 4443–4455. [CrossRef]
46. Filina, M.A.; Potapova, E.V.; Makovik, I.N.; Zharkih, E.V.; Dremin, V.V.; Zherebtsov, E.A.; Dunaev, A.V.; Sidorov, V.V.; Krupatkin, A.I.; Alimicheva, E.A.; et al. Functional Changes in Blood Microcirculation in the Skin of the Foot during Heating Tests in Patients with Diabetes Mellitus. *Hum. Physiol.* **2017**, *43*, 693–699. [CrossRef]
47. Zherebtsova, A.I.; Zherebtsov, E.A.; Dunaev, A.V.; Podmasteryev, K.V.; Pilipenko, O.V.; Krupatkin, A.I.; Khakhicheva, L.S.; Muradyan, V.F. Study of the functional state of peripheral vessels in fingers of rheumatological patients by means of laser Doppler flowmetry and cutaneous thermometry measurements. *Proc. SPIE* **2016**, *9917*, 99170M–99170M-7.

48. Nieuwenhoff, M.; Wu, Y.; Huygen, F.; Schouten, A.; van der Helm, F.; Niehof, S. Reproducibility of axon reflex-related vasodilation assessed by dynamic thermal imaging in healthy subjects. *Microvasc. Res.* **2016**, *106*, 1–7. [CrossRef]
49. Liebert, A.; Zołek, N.; Maniewski, R. Decomposition of a laser-Doppler spectrum for estimation of speed distribution of particles moving in an optically turbid medium: Monte Carlo validation study. *Phys. Med. Biol.* **2006**, *51*. [CrossRef] [PubMed]
50. Maldonado, G.; Guerrero, R.; Paredes, C.; Ríos, C. Nailfold capillaroscopy in diabetes mellitus. *Microvasc. Res.* **2017**, *112*. [CrossRef] [PubMed]
51. Shih, T.C.; Zhang, G.; Wu, C.C.; Hsiao, H.D.; Wu, T.H.; Lin, K.P.; Huang, T.C. Hemodynamic analysis of capillary in finger nail-fold using computational fluid dynamics and image estimation. *Microvasc. Res.* **2011**, *81*, 68–72. [CrossRef] [PubMed]
52. Fredriksson, I.; Larsson, M. Vessel packaging effect in laser speckle contrast imaging and laser Doppler imaging. *J. Biomed. Opt.* **2017**, *22*, 1–7. [CrossRef]
53. Chang, C.H.; Tsai, R.K.; Wu, W.C.; Kuo, S.L.; Yu, H.S. Use of dynamic capillaroscopy for studying cutaneous microcirculation in patients with diabetes mellitus. *Microvasc. Res.* **1997**, *53*. [CrossRef]
54. Wang, G.; Jia, S.; Li, H.; Song, X.; Zhang, W. Exploring the relationship between the speed-resolved perfusion of blood flux and HRV following different thermal stimulations using MSE and MFE analyses. *PLoS ONE* **2019**, e0217973. [CrossRef]

diagnostics

MDPI

*Article*

# Optical Diagnostics of the Maxillary Sinuses by Digital Diaphanoscopy Technology

**Ekaterina O. Bryanskaya [1,*], Irina N. Novikova [1], Viktor V. Dremin [1,2], Roman Yu. Gneushev [1], Olga A. Bibikova [3], Andrey V. Dunaev [1] and Viacheslav G. Artyushenko [3]**

[1] R & D Center of Biomedical Photonics, Orel State University, Orel 302026, Russia; irina.makovik@gmail.com (I.N.N.); dremin_viktor@mail.ru (V.V.D.); tef312@yandex.ru (R.Y.G.); dunaev@bmecenter.ru (A.V.D.)
[2] College of Engineering and Physical Sciences, Aston University, Birmingham B4 7ET, UK
[3] Art Photonics GmbH, 12489 Berlin, Germany; olga.a.bibikova@gmail.com (O.A.B.); sa@artphotonics.com (V.G.A.)
* Correspondence: bryanskayae@mail.ru; Tel.: +7-980-366-29-12

**Abstract:** The work is devoted to the development of a scientific and technical basis for instrument implementation of a digital diaphanoscopy technology for the diagnosis of maxillary sinus inflammatory diseases taking into account the anatomical features of patients (differences in skin structure, skull bone thickness, and sinus size), the optical properties of exercised tissues, and the age and gender characteristics of patients. The technology is based on visualization and analysis of scattering patterns of low-intensity radiation as it passes through the maxillary sinuses. The article presents the experimental data obtained using the digital diaphanoscopy method and the results of numerical simulation of the optical radiation passage through the study area. The experimental setup has been modernized through the installation of a a device for controlling the LED applicator brightness. The approach proposed may have considerable promise for creating diagnostic criteria for various pathological changes and can be used to assess the differences in the optical and anatomical features of males and females.

**Keywords:** optical diagnostics; digital diaphanoscopy; magnetic resonance imaging; paranasal sinuses; inflammatory diseases; Monte Carlo simulation



**Citation:** Bryanskaya, E.O.; Novikova, I.N.; Dremin, V.V.; Gneushev, R.Y.; Bibikova, O.A.; Dunaev, A.V.; Artyushenko, V.G. Optical Diagnostics of the Maxillary Sinuses by Digital Diaphanoscopy Technology. *Diagnostics* **2021**, *11*, 77. https://doi.org/10.3390/diagnostics11010077

Received: 19 November 2020
Accepted: 31 December 2020
Published: 6 January 2021



## 1. Introduction

Sinusitis is a common disease with worldwide prevalence and one of the leading causes of antibiotic prescription [1]. In 2018, 28.9 million people in the United States reported a sinusitis diagnosis in the previous 12-month period, which accounted for 11.6% of the adult population [2]. In Europe, sinusitis affects 10.9% of the population [3]. Delay in diagnosis and treatment of sinusitis may cause serious effects such as immune sensitivities to medication, development of different complications, including intracranial complications (50% of deaths). Therefore, an accurate, painless, and timely diagnosis of maxillary sinus pathology is one of the key problems of modern otolaryngology. Diagnostic imaging techniques, such as radiography, computed tomography, magnetic resonance imaging, ultrasound diagnostics (including assessment of stiffness and echogenicity), and rhinoscopy, are important tools to detect this kind of disorder, but they are not recommended for pregnant women and children due to the use of carcinogenic roentgen radiation during the study, painfulness of the diagnostic procedures, and a high level of false-negative results.

Radiography is based on the high penetrating power of radiation and its absorption ability. It allows assessing the general condition of the paranasal sinuses and makes it possible to detect the presence of liquid content (along with formed cysts or polyps) in them, as well as the changes in the mucous membrane. If there is a pathological change in sinus pneumatization, then the resulting image will show significant darkening along the

upper horizontal level, asymmetry of the inflamed sinuses, narrowing of the nasal passages, and mucosal thickening [4]. Despite the advantages of this technique, its application in clinical practice is limited to assessments that help to identify the degree of development of a pathological process which already has pronounced signs to determine further treatment tactics and the need for surgical interventions. It should also be noted that a high dose of radiation exposed to pregnant women raises the risk of hypertension, may slow down the growth of the fetus, and cause the worsening of the health indicators of newborns.

The major contribution of computed tomography (CT) is in providing additional useful information. The CT method, similar to other imaging techniques, uses X-ray radiation and its distribution in tissues depending on their density. CT provides the differentiation of soft tissues and can distinguish between density differences of no more than 0.1%. However, it is also associated with significant radiation exposure [5].

Magnetic resonance imaging (MRI), endoscopy (rhinoscopy), or ultrasound are used as alternative methods. The MRI method consists in registering the excitation of hydrogen atomic nuclei by a certain combination of electromagnetic waves in a constant magnetic field of high intensity [5]. MRI can be useful in assessing lesions in nasal bones, inflammatory processes in the paranasal sinuses, formed cysts or polyps, chronic diseases, and changes in bone structure resulting from injury. However, this method is characterized by a high level of false positive results, poor visualization of bone tissue, and is contraindicated in the presence of implants, prostheses, and obesity. The disadvantages of this method are the cost and high microwave load on the patient.

Rhinoscopy is performed by placing a flexible fiber-optic tube into the nasal passage to assess the color of the mucous membrane, its humidity, the shape of the nasal septum, the caliber of vessels, the condition of the nasal shell, and the size and content of the nasal passages. Although rhinoscopy yields important information and adequate sample collection, it also has some disadvantages which include its high cost and discomfort to the patient.

Ultrasound makes it possible to diagnose inflammatory processes in the sinuses, cysts, polyps, and traumatic damage to the walls of the paranasal sinuses, as well as to detect foreign bodies. Normally, the paranasal sinuses contain air, which serves as an obstacle to the propagation of ultrasonic waves. In the absence of pathological changes, the echo signal from the sinus is not detected due to its complete reflection from the air contained in it. If the walls of the sinuses are thickened, for example, due to edema of the mucosa, or they contain pathological contents, then there occur conditions for the propagation of ultrasound waves. When passing through the sinus, ultrasound waves are reflected from its posterior parts and are fixed by an ultrasound device. The results of ultrasound scanning do not always correspond to reality, which can be attributed to deficiencies in equipment design or incorrect interpretation of the results.

Non-invasive optical technologies are increasingly used in various fields of medicine to diagnose pathological conditions. The digital diaphanoscopy method has the potential to separate normal and pathological conditions (inflammation, cystic, and tumor tissues) of the maxillary sinuses. It is based on the visualization of scattering patterns of low-intensity radiation as it passes through the maxillary sinuses [6–8]. Although the method of diaphanoscopy or transillumination has a long history of usage [9,10], especially in ophthalmology [11] and urology [12], it is of limited use in otolaryngology. First examinations of tissue parameters in the near infrared were performed by Beuthan in 1982. Relying on these tests, infrared transillumination seems to be a promising tool for the rapid diagnosis of sinusitis, but white light spectrum radiation is a limiting factor influencing the application of this approach in otolaryngology [13,14]. White light does not provide a complete diagnostic picture because it is absorbed and dispersed by tissues to a great extent; no informative features and algorithms capable of separating normal and pathological conditions exist. At present, there are no clinically justified classifying features, developed classification models, and diagnostic criteria that can differentiate pathological changes in the maxillary sinuses (inflammation, cysts, and tumor tissues) by digital diaphanoscopy.

The purpose of this study was to develop a scientific and technical basis for instrument implementation of the technology proposed for diagnosing maxillary sinus pathology, taking into account the anatomical features of the study area (skin structure, bone thickness of the facial part of the skull, sinus size, and asymmetry), its optical properties, and age and gender characteristics.

## 2. Materials and Methods

### *2.1. Experimental Setup*

For the realization of this approach, the experimental setup was designed and assembled (Figure 1a). Low-intensity radiation of the visible (650 nm) and NIR (850 nm) ranges was used for translucence of the paranasal sinuses. The CMOS-camera was applied to visualize the light scattering pattern [15]. To minimize the external illumination influence, a protective screen was designed which facilitated research under various external conditions. To suppress movement artifacts, the volunteers were asked to place their head on a chin rest.

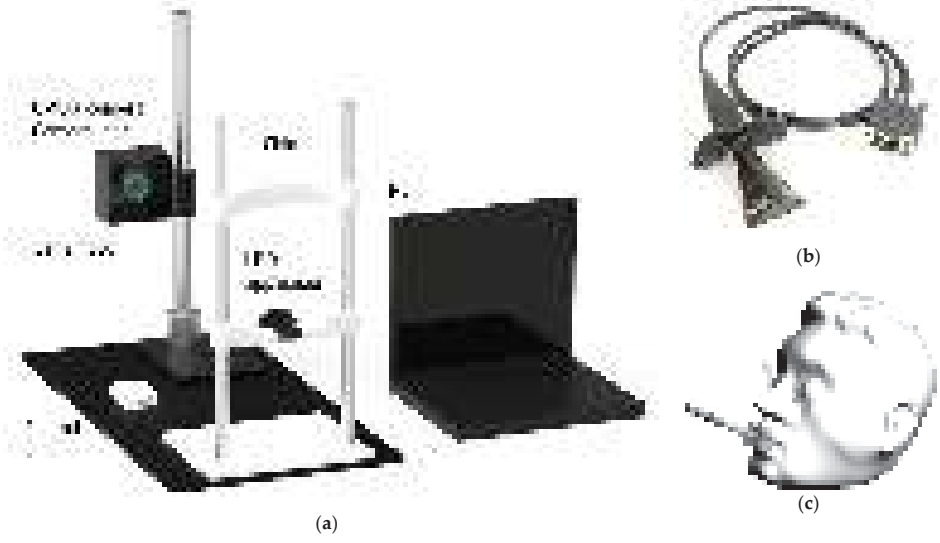

(**a**) (**b**) (**c**)

**Figure 1.** General view of the experimental setup (**a**); the LED applicator (the working part) (**b**); and the position of the applicator during measurement with the propagation of probing rays (3D model) (**c**).

The LED applicator takes into account the anatomical features of the study area, namely, the features of the oral cavity and maxillary sinuses (Figure 1b). During the diagnostic procedure, the applicator was placed in the oral cavity, and then the measurements were performed (Figure 1c). Before each use, the surface of the applicator was cleaned with wipes impregnated with a disinfecting solution. The solution composition included purified water, isopropanol, ethanol, didetsildimetilammonium chloride, and dodecyl dipropylene triamine.

The micro-LEDs OSRAM Opto Semiconductors GmbH (Regensburg, Germany) with wavelengths of 650 (C4L-H12T5) and 850 nm (F3453) and 8 pieces on the right and left sides for each wavelength were used as radiation sources for the applicator. The CMOS-camera UI-3240CP-NIR-GL Rev.2 IDS GmbH (Obersulm, Germany) and the lens Pentax C1614-M (Tokyo, Japan) were applied to register diagnostic information in the prototype device. The camera provides high-speed image acquisition, high quality, and maximum quantum efficiency (light sensitivity) in the selected spectral range. The control unit provides the

LEDs sequential switching on and off at wavelengths of 650 and 850 nm, as well as their performance in the setting mode (LEDs flashing at a wavelength of 650 nm).

The specially designed software assists us in analyzing the obtained scattering pattern. It allows for trial control (selection of a radiation source and a camera operation mode), gathering of personal patient data, and recording of diaphanoscopic images and their quantitative (visualization) and qualitative processing (pseudo-color image segmentation). The software also provides the function of uploading a diaphanoscopic examination report, which contains information about the patient, diaphanoscopic images, diagnostic assessments, and quantitative values (the percentage of light passed through the sinus).

### *2.2. Study Design*

The study groups were formed taking into account the differences in age, gender parameters, and anatomical features of the study area, as well as the existing pathological changes and inflammatory processes of the maxillary sinuses. Preliminary experimental studies were conducted in 20 conditionally healthy volunteers and 15 patients with suspected maxillary sinus inflammation at the medical diagnostic center "MediScan" (Orel, Russia).

The study was approved by the Ethics committee of the Orel State University (record of meeting No. 15 of 21 February 2019) and carried out in accordance with the 2013 Declaration of Helsinki by the World Medical Association. After receiving the description of the protocol, the volunteers signed an informed consent indicating their voluntary willingness to participate in the study.

The experiments were conducted under established protocols. The subjects were in a sitting position. After the pre-disinfected LED-applicator was inserted into the oral cavity of the subject, the subject head was placed in a precision positioning unit and, then, together with the CMOS-camera, it was covered with a protective screen. To account for the effect of the camera exposure time on the light scattering patterns, images were recorded at 40 different camera exposure times in the range from 0 to 40 ms (increment of 1 ms). In the patient study, the measurement results were additionally compared with the T2 weighted images by MRI studies, which were performed using the 1T MRI Scanner of the Magnetom series, Siemens (Munich, Germany).

## 3. Results

### *3.1. Results of Preliminary Experimental Studies*

The data obtained in trials with healthy volunteers showed that changing the camera exposure time does not significantly affect the diagnostic result. Therefore, further analysis of the experimental data was carried out at the camera exposure time of 20.7 ms.

Figures 2 and 3 present the registered and processed images for two conditionally healthy volunteers (a man and a woman of the same age group) with the same camera exposure time of 20.7 ms for probing radiation wavelengths of 650 nm (a) and 850 nm (b).

Preliminary experimental studies using the relevant method MRI have confirmed the sensitivity of the digital diaphanoscopy method in detecting pathological changes in the maxillary sinuses [6]. Figure 4 gives examples of the T2 weighted MRI images (Figure 4a) and the images registered and processed by diaphanoscopy (Figure 4b).

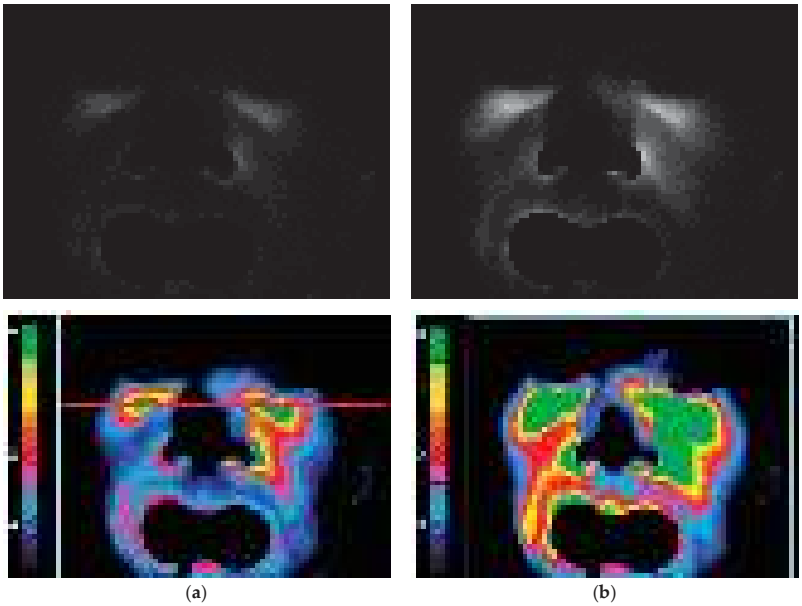

(**a**) (**b**)

**Figure 2.** Registered (**top**) and processed (**bottom**) images for a conditionally healthy volunteer 1 (male) at a camera exposure time of 20.7 ms for probing radiation wavelengths of: 650 nm (**a**); and 850 nm (**b**). The red line is the selection of the area for analyzing the transmitted light.

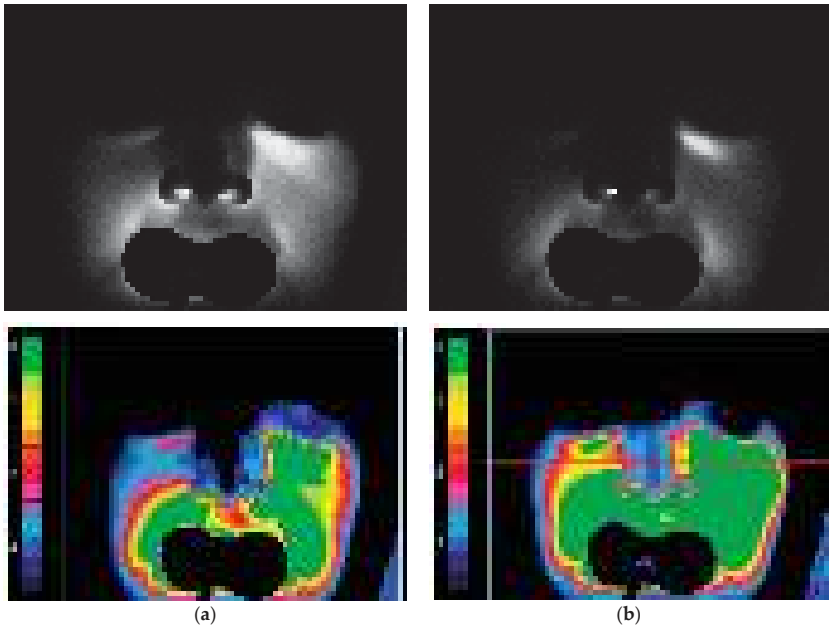

(**a**) (**b**)

**Figure 3.** Registered (**top**) and processed (**bottom**) images for a conditionally healthy volunteer 2 (female) at a camera exposure time of 20.7 ms for probing radiation wavelengths of: 650 nm (**a**); and 850 nm (**b**).

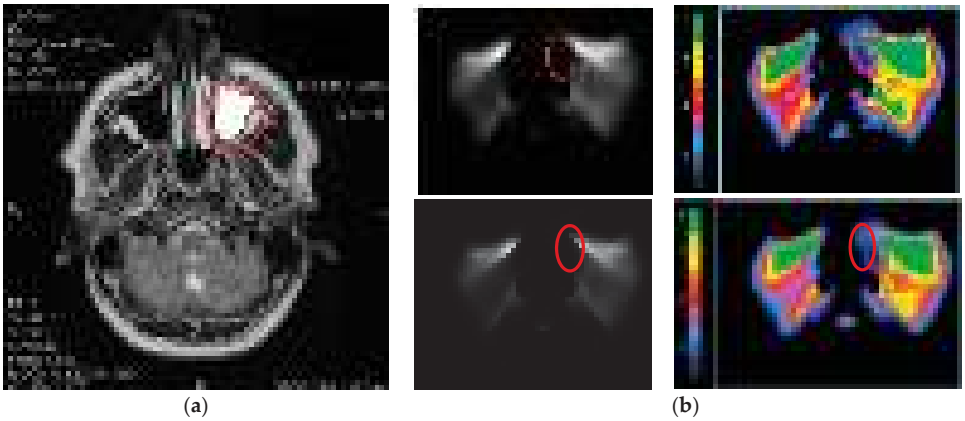

(**a**) (**b**)

**Figure 4.** The T2 weighted MRI image (**a**); and the images registered and processed by diaphanoscopy (**b**) for a patient (male) at radiation wavelengths of 650 nm (**top**) and 850 nm (**bottom**).

Analysis of the registered and processed images obtained by digital diaphanoscopy revealed that the cyst area is characterized by the lowest intensity compared to other structures, which can be explained by the strong absorbing properties of the cystic fluid in the near-infrared range [6]. The results of digital diaphanoscopy are determined by the optical properties of the study area [16–23] and their changes in various anatomical and gender features [24,25]. In our study, we applied Monte Carlo simulation to take into account the effect of the anatomical and gender characteristics of patients on the scattering pattern of light, to justify the medical and technical requirements for the instrument, and to adjust the parameters of the LED applicator.

### *3.2. Monte Carlo Simulation*

Since the object of research has a rather complex organization, a simplified model of the maxillary sinus was developed to establish the regularity of the weakening of the probing signal from the anatomical and gender features of the studied area (differences in the skin structure, the thickness of the skull bone tissue, and the size of the sinuses). The Monte Carlo methodology was used for the construction of the 3D model. This method is one of the most effective simulation tools when dealing with biological tissues [26,27]. Figure 5 shows a scheme of the developed model.

**Figure 5.** Full 3D view of the developed model.

In the model, the environment is represented by 8 main layers, as well as by an additional layer in the form of a pathological change (cystic fluid or tumor). The optical characteristics of the biological tissues used in the simulation are presented in Table 1.

**Table 1.** The optical characteristics of biological tissues.

| Biological Tissue Layer | Wavelength λ, nm | Absorption Coefficient $\mu_a$, $mm^{-1}$ | Scattering Coefficient $\mu_s$, $mm^{-1}$ |
|---|---|---|---|
| Mucous membrane (sinus/palatine bone) [18] | 650 | 0.05 | 0.8 |
| | 850 | 0.075 | 1.2 |
| Zygomatic/Palatine bone [19,20] | 650 | 0.011 | 1.873 |
| | 850 | 0.007 | 2.113 |
| Cystic fluid [16,17] | 650 | 0.022 | 1.34 |
| | 850 | 0.027 | 0.95 |
| Tumor [21] | 650 | 0.0391 | 2.17 |
| | 850 | 0.0522 | 2.67 |
| Hypodermis [22] | 650 | 0.18 | 2 |
| | 850 | 0.1 | 2.7 |
| Epidermis and dermis [23] | 650 | 0.17 | 3 |
| | 850 | 0.2 | 3.7 |

The thickness and size of the layers and their absorption and scattering coefficients were set for both females and males. Since the sizes and thicknesses of the layers depend on gender and age [18,19], the layer thicknesses were averaged within one gender to simplify the developed model. The thicknesses of the simulated layers are given in Table 2.

**Table 2.** The thickness of the simulated layers, mm.

| Layer | Male | Female |
|---|---|---|
| Mucous membrane of a palatine bone [25,28] | 2 | 3 |
| Palatine bone [24,25,29] | 3.1 | 3.1 |
| Mucous membrane of a sinus [17] | 0.5 | 0.5 |
| Sinus [29,30] | 6.7 | 6.2 |
| Zygomatic bone [31,32] | 26 | 23 |
| Hypodermis [33] | 3 | 3 |
| Epidermis and dermis [33] | 1.5–3 | 1–2 |

Analysis of the optical properties of the research area indicates high absorbing properties of the hypodermis at the selected wavelengths of probing radiation. In addition, the results of the preliminary experimental studies demonstrate that the changes in the hypodermis thickness strongly affect the diagnostic result.

The Monte Carlo simulation involving a simplified model of the research area was performed for 650 and 850 nm radiation sources in the TracePro software environment (Lambda Research Corporation) [34–36]. The number of simulated photons was $10^6$. The power of probing radiation in the simulation for the wavelengths of 650 and 850 nm was 8 mW.

Figures 6–8 show the simulation results of the probe radiation propagation (the photons path through the biological tissue and the irradiance map) for the maxillary sinus of female (a) and male (b) without pathology (Figure 6), with cystic fluid (Figure 7) and with tumor (Figure 8).

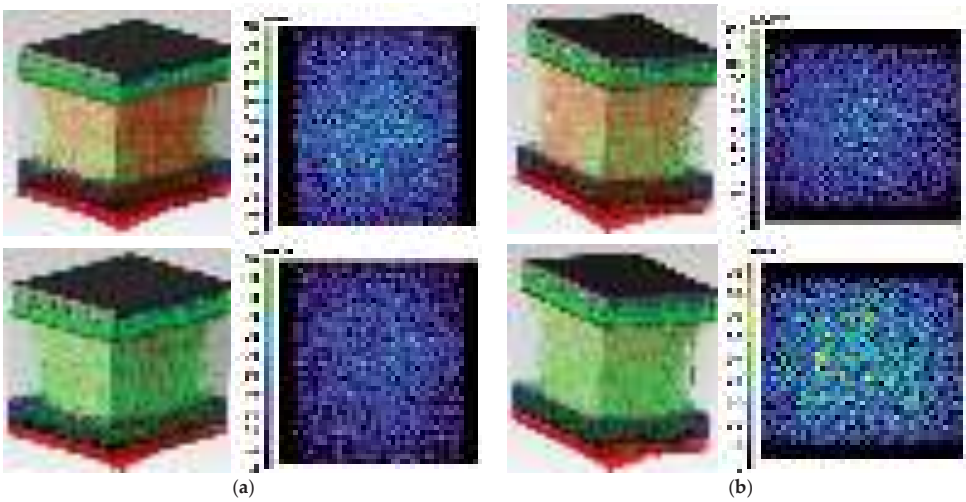

(**a**) (**b**)

**Figure 6.** Simulation results for the probe radiation propagation through the maxillary sinus of female (**a**) and male (**b**) without pathology at a wavelength of 650 nm (**top**) and 850 nm (**bottom**).

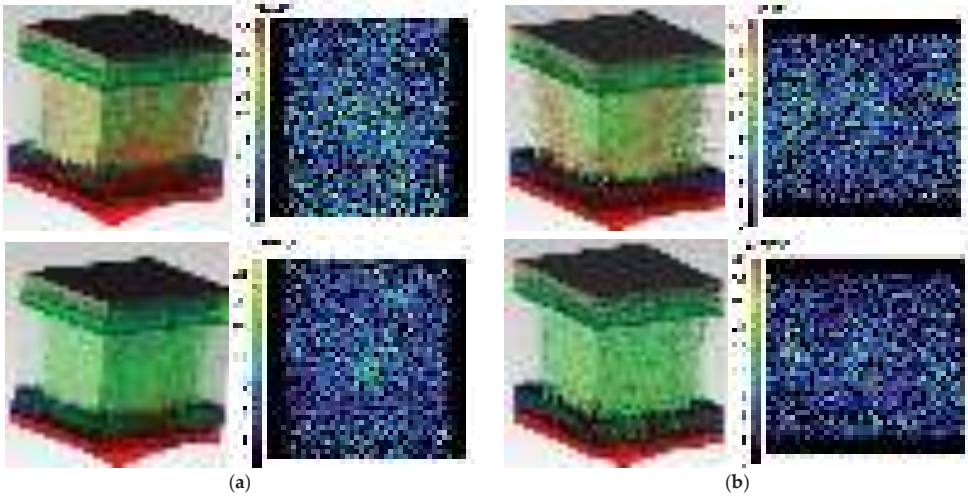

(**a**) (**b**)

**Figure 7.** Simulation results for the probe radiation propagation through the maxillary sinus of female (**a**) and male (**b**) with cystic fluid at a wavelength of 650 nm (**top**) and 850 nm (**bottom**).

Figure 9 illustrates the difference in radiation power (intensity) reduction in males and females. This decrease has a more pronounced character when the pathology in the sinuses is observed in the NIR range (850 nm) and can be attributed to the optical features of pathological tissues, namely, the high absorption properties at selected wavelength [16,17].

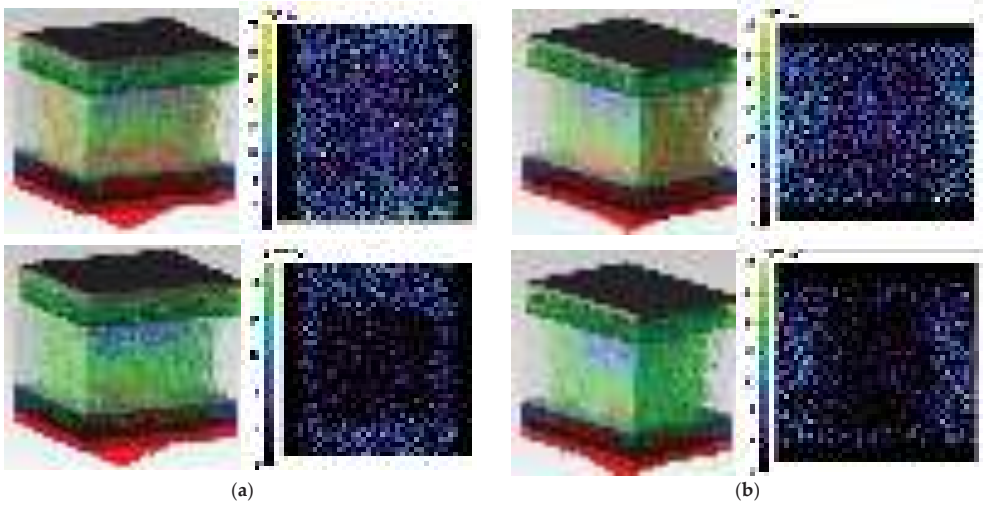

(**a**) (**b**)

**Figure 8.** Simulation results for the probe radiation propagation through the maxillary sinus of female (**a**) and males (**b**) with tumor at a wavelength of 650 nm (**top**) and 850 nm (**bottom**).

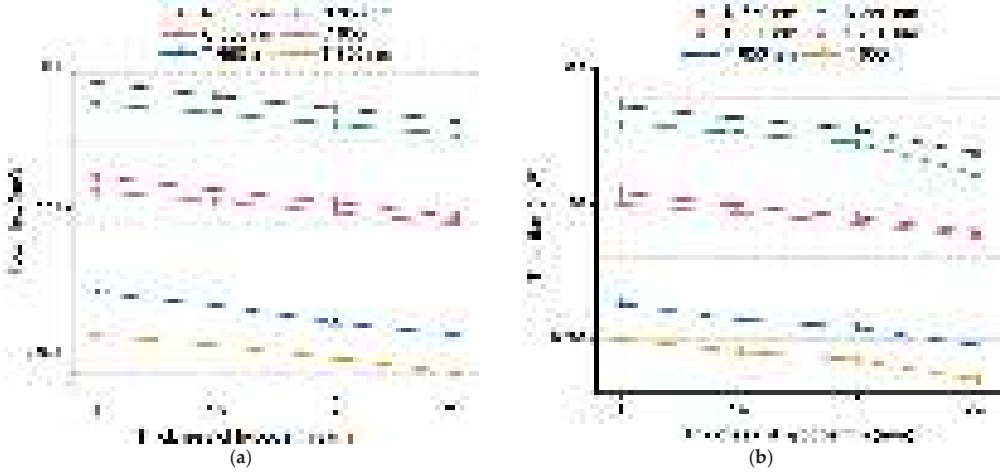

(**a**) (**b**)

**Figure 9.** Dependence of the change in the total flux (power) of radiation coming to the camera detector on the change in the hypodermis thickness and on the presence of pathology in the sinuses of female (**a**) and males (**b**) for wavelengths of 650 and 850 nm. The following labels are used: "N" for healthy tissues, "C" for tissues with cyst, and "T" for tissues with tumor.

Besides, the results demonstrate a decrease in the intensity of radiation at the detector (radiant power) when it passed through the biological tissues at different values of the bone tissue and skin, the sinus size [22,23].

The revealed regularity confirmed the results of the experimental studies. It was also found that the adjustment of the parameters of the probing and measuring parts of the device for implementation of the proposed technology is necessary to ensure similar scattering light patterns for different patients and their further comparison.

*3.3. Upgrade of the Experimental Setup*

Based on the simulation results, the experimental setup was upgraded; the block scheme of the setup is shown in Figure 10.

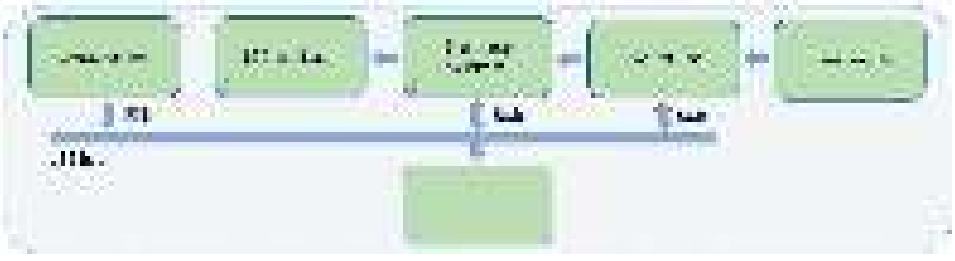

**Figure 10.** The block scheme of a modernized experimental setup.

A controller of the LED applicator brightness was designed and installed in the setup in addition to the unit controlling the output power of the probing applicator. It is positioned in the gap between the LED control unit of the applicator and the LED applicator itself. To control the operation of the controller of the LED applicator, an additional software has been developed, which allows one to change the voltage supplied to the LEDs, as well as to measure the current flow in real time and to calculate the power consumption. The software makes it possible to save many brightness profiles and switch them immediately before starting the measurements, thereby automatically selecting the desired range of radiation power of the applicator for specific volunteers and patients in accordance with their anatomical features.

The experimental studies, which were conducted using the modernized installation, allowed the detection of changes in the power consumption of the LEDs applicator. To identify the values of power consumption specific to each patient based on their gender and anatomical features, the study involved conditionally healthy volunteers; the power consumption of the LEDs applicator varied from 0 to 750 mW in increments of 50 mW. The camera exposure time remained unchanged. It was established that, in healthy male volunteers, the maximum power consumption of the LEDs applicator was insufficient to obtain an adequate scattering pattern of light passing through the sinuses, which is associated with their anatomical features (bone thickness, skin, and size of the sinuses). In female volunteers, the maxillary sinuses were visualized in the range of LEDs power consumption equal to 300–500 mW.

The ranges of changes in the radiation flux for the two radiation sources were also revealed. Thus, it was found that at 850 nm the radiation flux varies in the range from 0 to 200 mW, whereas for the 650 nm radiation source this parameter changes in the range from 0 to 18 mW.

In the future, the elements of the controller of the LED applicator brightness will be adjusted and replaced, and a new applicator will be designed to increase the radiated light power.

## 4. Discussion

In this study, we tested a device designed to implement the digital diaphanoscopy technology, which is based on visualization and analysis of the low-intensity radiation scattering pattern in the maxillary sinuses.

The review and analysis of existing methods (CT and MRI) for the diagnosis of inflammatory diseases of maxillary sinuses diseases showed their limitation either for the repeated conduct of studies due to radiation or microwave exposure or for the conduct of studies in general, for example, for pregnant women or children. In otolaryngology, the standard methods for diagnosing such pathologies (ultrasound and rhinoscopy tech-

niques) sometimes yield false positive results due to complexity in interpreting the results, or due to trauma-related aspects. In comparison with the considered methods, the method of digital diaphanoscopy allows one to overcome these drawbacks.

In addition, the review of the literature in the field of non-invasive optical diagnosis of paranasal pathology demonstrates that our technology has the advantage over the previously published results, as it provides a foundation for the assessement of the condition of the sinuses for all categories of patients, based on their anatomical and gender features. For this purpose, we designed the original brightness controller of the LED applicator and developed a specialized adjustment software for the probing mode, which makes it possible to select an effective radiation dose for each patient.

Currently, further experimental studies are being conducted to form an appropriate database and identify diagnostic criteria for various pathological changes, taking into account the range of the optical power of probing radiation, that have the greatest sensitivity to visualization of pathological changes in the maxillary sinuses in different study groups divided by gender.

## 5. Conclusions

Preliminary trials were conducted in 20 conditionally healthy volunteers and 15 patients with suspected maxillary sinus inflammation. The influence of anatomical and gender features of the study area on the diagnostic results (differences in skin structure, skull bone thickness, and sinus size) was revealed. The sensitivity of the prototype device to detect pathological changes was confirmed by the results of MRI studies.

The simulation results show the regularity of changes in the light scattering and parameters of the probing and measuring parts of the experimental setup. The mathematical model developed via Monte Carlo simulation made it possible to take into account the anatomical and gender features of the study area, as well as the absorption and scattering of optical radiation.

The prototype of the device was upgraded to obtain similar scattering patterns of light for different patients and to ensure their comparison. To adjust the output power of the probing applicator, a device for controlling the LED applicator brightness was designed, and additional software was developed.

The obtained results can be used to create modern diagnostic devices for the diagnosis of maxillary sinus pathology based on visualization and analysis of the low-intensity radiation scattering pattern. The application of the developed digital diaphanoscopy technology will make it possible to conduct timely, reliable, and painless diagnostics of maxillary sinus pathology, assess the dynamics of changes in the pathological processes within the framework of the therapy, and analyze its effectiveness. It is important to note that, due to the portability and simplicity of its instrument implementation, the technology can be used as a screening method for assessing the condition of the maxillary sinuses both in hospital and medical institutions and remotely in the absence of otolaryngologists and diagnosticians.

**Author Contributions:** Original draft preparation and, measurements, E.O.B. and I.N.N.; data acquisition setup, methodology, and numerical simulation, V.V.D.; numerical simulation, R.Y.G.; experiments at the Diagnostic Medical Center "MediScan" (Orel, Russia), E.O.B.; funding acquisition, supervision, and project administration, A.V.D.; and original development of the project idea and supervision, O.A.B. and V.G.A. All authors edited the manuscript. All authors have read and agreed to the published version of the manuscript.

**Funding:** The reported study was funded by RFBR according to the research project No. 20-32-90147 (original draft preparation, measurements, numerical simulation). The work was also supported by the grant of the President of the Russian Federation for state support of young Russian scientists No. MK-2634.2019.8 (development of experimental setup and data acquisition). V.D. kindly acknowledges personal support from the European Union's Horizon 2020 research and innovation programme under the Marie Skłodowska-Curie grant agreement No. 839888.

**Institutional Review Board Statement:** The study was conducted according to the guidelines of the Declaration of Helsinki by the World Medical Association and approved by the Ethics committee of the Orel State University (record of meeting No. 15 of 21 February 2019).

**Informed Consent Statement:** Informed consent was obtained from all subjects involved in the study.

**Data Availability Statement:** The data that support the findings of this study are available upon reasonable request request from the corresponding author.

**Acknowledgments:** Thanks for assistance in project realization are given to Olaf Minet (Charité Universitätsmedizin Berlin, Berlin, Germany) and Urszula Zabarylo (Charité—Universitätsklinikum Berlin, Berlin, Germany). Special thanks are extended to the head doctor of Diagnostic Medical Center "MediScan" (Orel, Russia) Boris Shuraev for assistance in conducting experiments and conceptualization.

**Conflicts of Interest:** The authors declare no conflict of interest. The funders had no role in the design of the study; in the collection, analyses, or interpretation of data; in the writing of the manuscript, or in the decision to publish the results.

## Abbreviations

| | |
|---|---|
| CT | computed tomography |
| MRI | magnetic resonance imaging |
| NIR | near infrared |
| CMOS | complementary metal oxide semiconductor |
| LED | light-emitting diode |

## References

1. Battisti, A.S.; Pangia, J. *Sinusitis. StatPearls—NCBI Bookshelf*; StatPearls Publishing: Treasure Island, FL, USA, 2018.
2. Villarroel, M.; Blackwell, D.; Jen, A. Tables of Summary Health Statistics for U.S. Adults: 2018 National Health Interview Survey. National Center for Health Statistics; NCHS: National Health Interview Survey. 2019. Available online: http://www.cdc.gov/nchs/nhis/SHS/tables.htm (accessed on 19 November 2020).
3. Hastan, D.; Fokkens, W.J.; Bachert, C.; Newson, R.B.; Bislimovska, J.; Bockelbrink, A.; Bousquet, P.J.; Brozek, G.; Bruno, A.; Dahlén, S.E.; et al. Chronic rhinosinusitis in Europe—An underestimated disease. A GA 2LEN study. *Allergy* **2011**, *66*, 1216–1223. [CrossRef] [PubMed]
4. Mafee, M.F.; Farid, N.; Lim, W.Y. Imaging of the Paranasal Sinuses: Plain-Film Radiography, Computed Tomography, and Magnetic Resonance Imaging. In *Diseases of the Sinuses*; Springer Science and Business Media LLC: Berlin/Heidelberg, Germany, 2014; pp. 295–322.
5. Kanwar, S.S.; Mital, M.; Gupta, P.K.; Saran, S.; Parashar, N.; Singh, A. Evaluation of paranasal sinus diseases by computed tomography and its histopathological correlation. *J. Oral Maxillofac. Radiol.* **2017**, *5*, 46–52. [CrossRef]
6. Bryanskaya, E.; Makovik, I.; Bukin, A.; Bibikova, O.; Shuraev, B.M.; Minet, O.; Zabarilo, U.; Dunaev, A.; Artyushenko, V. Diagnosis of inflammatory diseases of the paranasal sinuses using digital diaphanoscopy. In Proceedings of the Clinical and Preclinical Optical Diagnostics II, Munich, Germany, 23–25 June 2019; p. 11073.
7. Bryanskaya, E.O.; Gneushev, R.Y.; Makovik, I.N.; Dremin, V.V.; Bukin, A.G.; Bibikova, O.A.; Shuraev, B.M.; Minet, O.; Zabarilo, U.; Dunaev, A.V.; et al. Monte Carlo simulation of signals in digital diaphanoscopy of the maxillary sinuses. In *Saratov Fall Meeting 2019: Optical and Nano-Technologies for Biology and Medicine*; SPIE: Saratov, Russia, 2020; Volume 11457, p. 114571K.
8. Stölzel, K.; Szczepek, A.J.; Olze, H.; Koß, S.; Minet, O.; Zabarylo, U. Digital diaphanoscopy of the maxillary sinuses: A revival of optical diagnosis for rhinosinusitis. *Am. J. Otolaryngol.* **2020**, *41*, 102444. [CrossRef] [PubMed]
9. Beuthan, J. IR-diaphanoscopy in medicine. *Med Opt. Tomogr. Funct. Imaging Monit.* **1993**, 103110H. [CrossRef]
10. Feldmann, H. Die Geschichte der Diaphanoskopie. *Laryngo-Rhino-Otologie* **1998**, *77*, 297–304. [CrossRef]
11. Koch, F.H.J.; Deuchler, S.; Hessling, M.; Singh, P. Diaphanoskopie am Auge Ophthalmic diaphanoscopy. *Der Ophthalmol.* **2017**, *11*, 331–864. [CrossRef]
12. Schips, L.; Lipsky, K.; Hebel, P.; Hutterer, G.; Gidaro, S.; Petritsch, P.H.; Zigeuner, R.E. Laparoscopic fenestration of lymphoceles after kidney transplantation with diaphanoscopic guidance. *Urology* **2005**, *66*, 185–187. [CrossRef]
13. Linnarz, M.; Hopf, J.U.G.; Prapavat, V.; Beuthan, J. *Die IR-Diaphanoskopie—Eine Neue Methode in der Diagnostik der Nasennebenhöhlen-Erkrankungen*; Springer Science and Business Media LLC: Berlin/Heidelberg, Germany, 1994; p. 252.
14. Hopf, M.; Hopf, J.U. Near Infrared Transillumination in Acute Maxillary Sinusitis: Theoretical Background—Clinical Application—Diagnostic Potential—Limitations. *Med. Laser Appl.* **2003**, *18*, 217–231. [CrossRef]
15. Bellemann, V. Digitale Diaphanoskopie der Nasennebenhöhlen. *Med. Bildgeb. Master* **2012**, *1*, 30–31.
16. Jacques, S.L. Optical properties of biological tissues: A review. *Phys. Med. Biol.* **2013**, *58*, R37–R61. [CrossRef]
17. Peters, V.G.; Wymant, D.R.; Patterson, M.S.; Frank, G.L. Optical properties of normal and diseased human breast tissues in the visible and near infrared in the visible and near infrared. *Phys. Med. Biol. Relat. Content* **1990**, *35*, 1317–1334. [CrossRef] [PubMed]

18. Bashkatov, A.N.; Genina, É.A.; Kochubey, V.I.; Tuchin, V.V.; Chikina, E.É.; Knyazev, A.B.; Mareev, O.V. Optical properties of mucous membrane in the spectral range 350–2000 nm. *Opt. Spectrosc.* **2004**, *97*, 978–983. [CrossRef]
19. Bashkatov, A.N.; Genina, E.A.; Kochubey, V.I.; Tuchin, V.V. Optical properties of human cranial bone in the spectral range from 800 to 2000 nm. *SPIE Proc.* **2006**, 616310. [CrossRef]
20. Genina, E.A.; Bashkatov, A.N.; Tuchin, V.V. Optical Clearing of Cranial Bone. *Adv. Opt. Technol.* **2008**, *2008*, 1–8. [CrossRef] [PubMed]
21. Van Veen, R.L.P.; Sterenborg, H.J.C.M.; Marinelli, A.W.K.S.; Menke-Pluymers, M. Intraoperatively assessed optical properties of malignant and healthy breast tissue used to determine the optimum wavelength of contrast for optical mammography. *J. Biomed. Opt.* **2004**, *9*, 1129–1136. [CrossRef]
22. Bashkatov, A.N.; Genina, E.A.; Tuchin, V.V. Optical properties of skin, subcutaneous, and muscle tissues: A review. *J. Innov. Opt. Health Sci.* **2011**, *4*, 9–38. [CrossRef]
23. Teke, H.Y.; Duran, S.; Canturk, N.; Canturk, G. Determination of gender by measuring the size of the maxillary sinuses in computerized tomography scans. *Surg. Radiol. Anat.* **2006**, *29*, 9–13. [CrossRef]
24. Gracco, A.; Lombardo, L.; Cozzani, M.; Siciliani, G. Quantitative evaluation with CBCT of palatal bone thickness in growing patients. *Prog. Orthod.* **2006**, *7*, 164–174.
25. Kang, S.; Lee, S.-J.; Ahn, S.-J.; Heo, M.-S.; Kim, T.-W. Bone thickness of the palate for orthodontic mini-implant anchorage in adults. *Am. J. Orthod. Dentofac. Orthop.* **2007**, *131*, S74–S81. [CrossRef]
26. Dremin, V.; Zherebtsov, E.; Bykov, A.; Popov, A.; Doronin, A.; Meglinski, I. Influence of blood pulsation on diagnostic volume in pulse oximetry and photoplethysmography measurements. *Appl. Opt.* **2019**, *58*, 9398–9405. [CrossRef]
27. Zherebtsov, E.; Dremin, V.; Popov, A.; Doronin, A.; Kurakina, D.; Kirillin, M.Y.; Meglinski, I.; Bykov, A. Hyperspectral imaging of human skin aided by artificial neural networks. *Biomed. Opt. Express* **2019**, *10*, 3545–3559. [CrossRef] [PubMed]
28. Wara-Aswapati, N.; Pitiphat, W.; Chandrapho, N.; Rattanayatikul, C.; Karimbux, N. Thickness of Palatal Masticatory Mucosa Associated With Age. *J. Periodontol.* **2001**, *72*, 1407–1412. [CrossRef] [PubMed]
29. Genina, E.A.; Zubkova, E.A.; Korobko, A.A.; Yanina, I.Y.; Bashkatov, A.N.; Kamenskikh, T.G.; Galanzha, V.A.; Tuchin, V.V. Diffusion of Cortexin and Retinalamin in eye sclera. In Proceedings of the Saratov Fall Meeting 2006: Optical Technologies in Biophysics and Medicine VIII, Saratov, Russia, 26–29 September 2006; Volume 65351.
30. Barghouth, G.; Prior, J.; Lepori, D.; Duvoisin, B.; Schnyder, P.; Gudinchet, F. Paranasal sinuses in children: Size evaluation of maxillary, sphenoid, and frontal sinuses by magnetic resonance imaging and proposal of volume index percentile curves. *Eur. Radiol.* **2002**, *12*, 1451–1458. [CrossRef] [PubMed]
31. Uchida, Y.; Goto, M.; Katsuki, T.; Akiyoshi, T. Measurement of the maxilla and zygoma as an aid in installing zygomatic implants. *J. Oral Maxillofac. Surg.* **2001**, *59*, 1193–1198. [CrossRef] [PubMed]
32. Xu, X.; Zhao, S.; Liu, H.; Sun, Z.; Wang, J.; Zhang, W. An Anatomical Study of Maxillary-Zygomatic Complex Using Three-Dimensional Computerized Tomography-Based Zygomatic Implantation. *BioMed Res. Int.* **2017**, *2017*, 1–8. [CrossRef] [PubMed]
33. De Greef, S.; Claes, P.; Vandermeulen, D.; Mollemans, W.; Suetens, P.; Willems, G. Large-scale in-vivo Caucasian facial soft tissue thickness database for craniofacial reconstruction. *Forensic Sci. Int.* **2006**, *159*, S126–S146. [CrossRef] [PubMed]
34. Dremin, V.; Dunaev, A. How the melanin concentration in the skin affects the fluorescence-spectroscopy signal formation. *J. Opt. Technol.* **2016**, *83*, 43. [CrossRef]
35. Rafailov, I.E.; Dremin, V.V.; Litvinova, K.S.; Dunaev, A.V.; Sokolovski, S.G.; Rafailov, E.U. Computational model of bladder tissue based on its measured optical properties. *J. Biomed. Opt.* **2016**, *21*, 025006. [CrossRef]
36. Rafailov, I.; Palmer, S.; Litvinova, K.; Dremin, V.; Dunaev, A.; Nabi, G. A novel excitation-emission wavelength model to facilitate the diagnosis of urinary bladder diseases. *Photonic Ther. Diagn. XI* **2015**, *9303*, 93030W. [CrossRef]

diagnostics

MDPI

*Article*

# Multimodal Diagnostics of Microrheologic Alterations in Blood of Coronary Heart Disease and Diabetic Patients

**Anastasia Maslianitsyna [1,*], Petr Ermolinskiy [1], Andrei Lugovtsov [1,2], Alexandra Pigurenko [3], Maria Sasonko [4], Yury Gurfinkel [5] and Alexander Priezzhev [1,2]**

[1] Physics Department, Lomonosov Moscow State University, 119991 Moscow, Russia; peter.ermolinskiy@biomedphotonics.ru (P.E.); anlug@biomedphotonics.ru (A.L.); avp@biomedphotonics.ru (A.P.)
[2] International Laser Center, Lomonosov Moscow State University, 119991 Moscow, Russia
[3] Faculty of Fundamental Medicine, Lomonosov Moscow State University, 119991 Moscow, Russia; pigurenko-alexandra-101-16-17@yandex.ru
[4] Research Clinical Center of JSC "Russian Railways", 123567 Moscow, Russia; msasonko@yandex.ru
[5] Medical Research and Educational Center, Lomonosov Moscow State University, 119991 Moscow, Russia; yugurf@yandex.ru
* Correspondence: stasyazavr2000@biomedphotonics.ru

**Abstract:** Coronary heart disease (CHD) has serious implications for human health and needs to be diagnosed as early as possible. In this article in vivo and in vitro optical methods are used to study blood properties related to the aggregation of red blood cells in patients with CHD and comorbidities such as type 2 diabetes mellitus (T2DM). The results show not only a significant difference of the aggregation in patients compared to healthy people, but also a correspondence between in vivo and in vitro parameters. Red blood cells aggregate in CHD patients faster and more numerously; in particular the aggregation index increases by 20 ± 7%. The presence of T2DM also significantly elevates aggregation in CHD patients. This work demonstrates multimodal diagnostics and monitoring of patients with socially significant pathologies.

**Keywords:** blood rheology; red blood cell aggregation; laser tweezers; laser aggregometry; digital capillaroscopy; coronary heart disease; diabetes mellitus



**Citation:** Maslianitsyna, A.; Ermolinskiy, P.; Lugovtsov, A.; Pigurenko, A.; Sasonko, M.; Gurfinkel, Y.; Priezzhev, A. Multimodal Diagnostics of Microrheologic Alterations in Blood of Coronary Heart Disease and Diabetic Patients. *Diagnostics* **2021**, *11*, 76. https://doi.org/10.3390/diagnostics11010076

Received: 4 November 2020
Accepted: 30 December 2020
Published: 6 January 2021



## 1. Introduction

Blood flow and circulation inside vessels in vivo are defined by many interconnected parameters, such as blood viscosity, hematocrit, and plasma protein composition, so to properly study them a complex approach is required [1]. There are many methods allowing for in vivo and in vitro measurements of different blood properties [1,2].

The main focus of this study is the aggregation of red blood cells (RBCs), which significantly influences the viscosity of blood [3]. RBC aggregation is the reversible process of the formation of linear and more complex structures of RBCs. It promotes the formation of peripheral cell-poor fluid layer that lowers the hydrodynamic vessel resistance to blood flow [3]. The process of in vitro as well as in vivo RBC aggregation can be described in several ways: by the number of cells aggregating during a given time interval, by how many aggregates are observed, by how fast a couple of RBCs can form a doublet, etc. [3]. These parameters require specialized tools in order to be measured, so they are not used widely in clinical conditions. RBC aggregation depends on many internal and external factors. For example, blood plasma composition, temperature, RBC shapes, and the age, state of health of an individual, and his or her medicine intake determine in part the aggregation parameters of RBCs [3–5].

Many methods can be applied to studying RBCs, including micropipette aspiration [6], etc., but among all methods it would be worth highlighting the optical techniques as far as they have several advantages: non-invasiveness and lack of direct mechanical contact with

the cells, the option to study both individual cells and their ensembles, and the possibility of in vivo and in vitro application [4,7]. The last point can pose a challenge in terms of comparing results for these different conditions—in vitro measurements require anticoagulants for stabilizing the blood samples and storing blood during sample preparation, which can influence the measured parameters, whereas in vivo methods allow for measuring a different set of parameters that may be difficult to correlate with those measured in vitro.

The aim of this work was to find correspondence between in vivo and in vitro optical methods by studying patients with cardiovascular and associated pathologies. Understanding the link between RBC aggregation and widespread cardiovascular diseases is vital to create new methods of diagnosis and treatment. In this article, we look at coronary heart disease (CHD) and type 2 diabetes mellitus (T2DM), which are known to have a significant effect on microvasculature [8].

## 2. Materials and Methods

### 2.1. Patients

The study enrolled 81 adults, including 25 healthy volunteers and 56 patients with CHD and arterial hypertension (Table 1). The patients with CHD were divided into two groups depending on the presence of T2DM. The first group included 42 CHD patients without T2DM, and second group included 14 CHD patients with T2DM. We did not find any statistically significant differences in the clinical background for these two groups of patients. The study was conducted during the period from July 2015 to July 2020.

**Table 1.** The clinical backgrounds for each group of patients, mean ± standard deviation or number (%).

| Parameter | Overall Patient Data ($n$ = 56) | Patients with CHD and without T2DM ($n$ = 42) | Patients with CHD and T2DM ($n$ = 14) |
|---|---|---|---|
| Number (percentage) of males | 38 (68%) | 29 (69%) | 9 (64%) |
| Number (percentage) of females | 18 (32%) | 13 (31%) | 5 (36%) |
| Mean age (range), years | 69.2 (51–92) | 70.5 (51–92) | 65.3 (52–81) |
| Number (percentage) of smokers | 10 (18%) | 6 (14%) | 4 (29%) |
| Body mass index, kg/m$^2$ | 29 ± 5 | 28 ± 5 | 31 ± 5 |
| Systolic blood pressure, mm Hg | 139 ± 27 | 142 ± 22 | 137 ± 20 |
| Diastolic blood pressure, mm Hg | 82 ± 12 | 82 ± 13 | 83 ± 9 |
| Heart rate, bpm | 71 ± 9 | 72 ± 9 | 69 ± 10 |
| LV ejection fraction, % | 57 ± 7 | 56 ± 6 | 58 ± 8 |
| Previous myocardial infarction | 22 (39%) | 18 (43%) | 4 (29%) |
| Angina pectoris | 48 (86%) | 36 (86%) | 12 (86%) |
| Bypass grafts | 5 (9%) | 4 (9%) | 1 (7%) |
| Stents | 17 (30%) | 12 (29%) | 4 (31%) |
| Antiaggregants | 39 (70%) | 29 (69%) | 10 (71%) |
| Anticoagulants | 12 (23%) | 10 (24%) | 3 (21%) |
| Diuretics | 28 (50%) | 19 (45%) | 9 (64%) |

CHD—coronary heart disease; T2DM—type 2 diabetes mellitus; LV ejection fraction—left ventricular ejection fraction.

Criteria for exclusion from the study were the following: chronic heart disease insufficiency, heart rhythm and conduction disorders, renal and hepatic insufficiency, type 1 diabetes mellitus, vascular or other pathology of the brain, or oncological diseases in the medical history.

The study included several procedures for the patients. The measurements of blood pressure and heart rate were conducted for each patient between 8:00 and 8:30 a.m. before their medicine intake on the day following their hospitalization in the cardiological unit. In addition to the standard medical check-up, all patients underwent a non-invasive study of microcirculatory parameters in the nail bed capillaries using the method of digital capillaroscopy. For the in vitro study, the blood was drawn from the patients' cubital veins on an empty stomach, stabilized with EDTA K2 anticoagulant and was used for the experiments within the first three hours.

Twenty-five healthy volunteers (16 males and 9 females) had an average age 27.5 and body mass index (BMI) of 22.1, were non-smokers, and had not taken any medication. These people were divided into two control groups ($n$ = 10 (4 males and 6 females) and 15 (12 males and 3 females)) that were studied independently at different time intervals with different parameters measured.

The study design was approved by the local ethics committee of medical research and educational center of M.V. Lomonosov Moscow State University, Moscow, Russia (protocol code: 1/19, date of approval: 18 February 2019). The experiment design took into account the latest recommendations for laboratories made by the international expert team for the standardization of hemorheological methods [9]. The patients and healthy volunteers participating in the research were informed on the purpose of the study and gave written informed consent in accordance with the Declaration of Helsinki.

### *2.2. Laser Aggregometry Method*

The laser aggregometry method implemented in a microchip stirring type RheoScan aggregometer (RheoMedTech, Seoul, Korea) was used to measure the aggregation parameters of RBCs in vitro in whole blood samples [10]. Laser aggregometry is based on the diffused light scattering of a laser beam by the blood sample [11]. To perform the measurements 8 μL of whole blood were placed inside a flat reservoir and heated up to 37 °C. Then the sample was illuminated by a laser beam (633 nm, 2.5 mW), which was scattered by the RBCs and their aggregates mostly in the forward direction—the scattering particles were much larger than the light wavelength. The larger the size of the scattering particle the more intensity was scattered forward [12,13].

The time course of measured intensity of light scattered forward is presented in Figure 1. In the beginning of the measurement the RBCs were in a state of maximum aggregation and therefore the scattered intensity was also at its maximum. Then, a small magnetic bar inside the reservoir started stirring the sample, causing shear stress-induced destruction of the aggregates. After the stirring process ($t$ = 0 in Figure 1), all aggregates were dispersed and none of the RBCs were in the aggregated state and therefore the scattered intensity was at its minimum; the cells themselves suffered no permanent damage from this. The stirring stopped and so the RBCs started to aggregate again, the average size of a scattering particle in the sample grew, and the scattered intensity increased. The aggregation process lasted approximately two minutes; after that the intensity reached its maximum, indicating that the cells were in a state of complete aggregation.

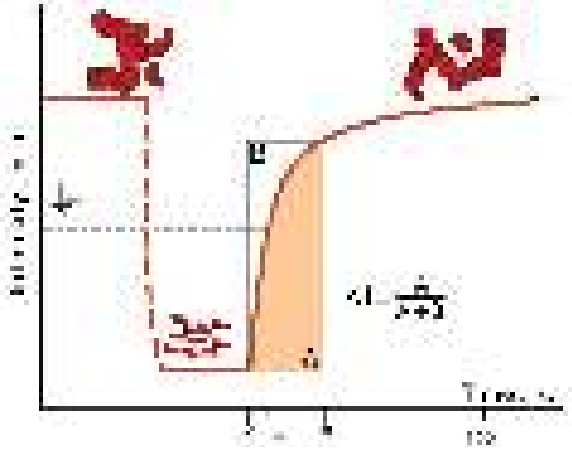

**Figure 1.** The kinetics of the RheoScan aggregometer output signal (intensity of light scattered forward as a function of time). The meaning of $T_{1/2}$ and AI is indicated. 'A' is the area below the intensity curve inside the rectangle; 'B' is the area above the intensity curve inside the rectangle.

The aggregation kinetics were reflected in the dependence of the scattered intensity on time and several parameters were calculated based on it. Firstly, the characteristic time of aggregate formation ($T_{1/2}$) characterized the time interval, during which the signal (scattered light intensity) reached half of the maximum value (see Figure 1). A smaller $T_{1/2}$ indicated greater curve slope and faster aggregation of the cells. Secondly, the aggregation index (AI) characterized the fraction of cells aggregated during the first 10 s of measurement. It was calculated as a ratio between the area under the intensity curve to the total area above and below it (see Figure 1). Higher AI values corresponded to more numerous RBC aggregation in the sample.

### *2.3. Laser Tweezers*

Laser tweezers (LT) are scientific tools that allow for the trapping and manipulation of microobjects (such as living cells, etc.) using a highly focused laser beam [14]. LT are essential instruments in single-cell studies. The physical principle of optical trapping is described in more detail in [15].

In our study, LT were used to measure the duration of the process of spontaneous aggregation of two individual RBCs [16]. Two beams from the Nd:YAG lasers (1064 nm, 200 mW) propagated through a system of lenses and polarizers and reached the dichroic mirror where they were split in two parts: The first one was directed to the aperture of the Olympus objective (×100, NA = 1.00, water immersion) and into the sample, and the second one to the photodetector in order to evaluate its power. One laser beam was always stationary whereas the other one could be moved by rotating the movable mirror—this allowed for two laser traps in the sample to be obtained: one stationary and one movable.

The measurements were carried out at room temperature (22 °C) in a highly diluted blood suspension inside a glass microcuvette with a 100 µm gap [17]. Patients' autological platelet-poor plasma was used as the suspension medium. The plasma was acquired by centrifuging all the blood for 10 min at 170 g, removing the platelet-rich plasma, then centrifuging the platelet-rich plasma for 10 min at 3000 g and removing the buffy coat. Lastly, the RBCs were added to the plasma to achieve the final hematocrit of about 0.1%. Due to such a high dilution of the suspension the hematocrit did not affect the measurements.

In LT the trapped RBCs oriented themselves vertically, so the cells were observed edge-on [18]. The time of doublet aggregate formation $T_{agg}$ was measured by orienting two trapped RBCs parallel to each other and creating a single point of contact between their membranes using the movable laser trap (see Figure 2a) [16]. Then, the laser traps were disabled and the time of the doublet formation as a result of spontaneous aggregation was measured (see Figure 2b,c). Smaller values of $T_{agg}$ corresponded to faster aggregate formation.

(**a**) (**b**) (**c**)

**Figure 2.** Three steps of $T_{agg}$ measurement. Red crosses indicate the laser traps. (**a**) Two separate RBCs are brought together until the state of a "point contact"; (**b**,**c**) RBCs start to aggregate (overlap) after the laser beams are shut off.

For the interpretation of the results, it needs to be emphasized that the $T_{agg}$ parameter corresponds to the initial stage of the aggregation process, whereas the laser aggregometry parameters ($T_{1/2}$ and AI) represent the whole aggregation process, including the later formation of complex 3D aggregate structures.

### *2.4. Digital Capillaroscopy*

Digital capillaroscopy was used to evaluate capillary blood flow parameters in vivo. Using the Kapillaroskan-1 device (AET, Moscow, Russia) a quantitative assessment of the blood flow characteristics was carried out in the nail bed capillaries. This method is described in more detail in [19,20]. Several nail bed capillaries of each patient were recorded at the high frame rate and then used to assess the average capillary blood flow velocity (CBV), which was calculated by frame-by-frame analysis.

Before the start of the measurements, the temperature of the skin of the studied finger was measured using an AND DT-635 skin thermometer (A&D, Tokyo, Japan). On average, the temperature of the skin of the finger in the patients included in the study was 33.6 ± 1.3 °C. There were no statistically significant differences between the groups considering the finger temperature.

### *2.5. Statistical Analysis*

For each blood sample, the parameters AI $T_{1/2}$, and $T_{agg}$ were measured 5 times. The calculation of the CBV and the presence of aggregates for the DC method was carried out using original software that analyzed recordings of the nail bed capillaries. Videos of at least 6 good reading capillaries were used for calculations with a video duration of 3 to 5 s (at a recording rate of 100 frames per second, i.e., from 1800 to 3000 frames per patient). In the Results section the averaged values and the standard errors of the mean are presented. They were chosen over the standard deviations because they show the precision of the mean value. Statistical difference was calculated with a two-tailed Student *t*-test with unequal variance. The difference between the two values was considered statistically significant if the *p*-value according to the *t*-test was less than 0.05.

## 3. Results

### *3.1. Comparison of CHD Patients and Healthy Volunteers*

The parameters assessed with the methods described above for all the CHD patients were different from the control values (Table 2). The first and second control group did not show statistically significant differences between themselves.

**Table 2.** The comparison of CHD patients and the control groups. The averaged values and the standard errors are presented. The *p*-value was calculated by a two-tailed *t*-test with unequal variance.

| Parameter/Group | Control Group A ($n$ = 15) | Control Group B ($n$ = 10) | CHD Patients ($n$ = 56) |
|---|---|---|---|
| AI, % | 41.0 ± 1.3 | 44 ± 3 | 49.0 ± 1.2 * |
| $T_{1/2}$, s | 5.9 ± 0.4 | 5.6 ± 1.0 | 4.2 ± 0.4 * |
| $T_{agg}$, s | 6.6 ± 0.4 | - | 4.8 ± 0.2 * |
| CBV, mcm/s | - | 1290 ± 230 | 850 ± 100 |

CHD—coronary heart disease; AI—aggregation index; CBV—capillary blood velocity; * $p < 0.05$ for control group A.

The values for control groups A and B did not show statistically significant differences for AI and $T_{1/2}$ (see Table 2), which proves the consistency of the laser aggregometry method. Unfortunately, other parameters ($T_{agg}$ and CBV) could not be measured for both control groups, but they were consistent with our previous work [11]. Control group A was studied more recently and had a greater number of subjects than group B, so we used it in the analysis.

In CHD patients compared to the control group A, AI was higher by 20 ± 7% ($p < 0.05$), meaning more numerous aggregation, $T_{1/2}$ was lower by 14 ± 9% ($p < 0.05$), meaning faster

aggregation, and $T_{agg}$ was lower by 27 ± 7% ($p < 0.05$), showing faster doublet formation. As for CBV, it was smaller than the control, but significant only at $p = 0.1$ level due to high variation from person to person.

The CHD patients were divided into two groups by the presence of T2DM and they showed significant ($p < 0.05$) differences in some parameters (Table 3).

**Table 3.** The comparison of CHD patients with and without T2DM. The averaged values and the standard errors of the sample mean are presented. The *p*-value was calculated by a two-tailed *t*-test with unequal variance.

| Parameter/Group | CHD Patients ($n$ = 42) | CHD + T2DM Patients ($n$ = 14) |
|---|---|---|
| AI, % | 48.6 ± 1.0 | 53.0 ± 1.1 * |
| $T_{1/2}$, s | 4.1 ± 0.2 | 3.1 ± 0.2 * |
| $T_{agg}$, s | 5.0 ± 1.2 | 4.6 ± 0.4 |
| CBV, mcm/s | 750 ± 90 | 1150 ± 300 |

CHD—coronary heart disease; T2DM—type 2 diabetes mellitus; AI—aggregation index; CBV—capillary blood velocity; * $p < 0.05$.

### *3.2. Digital Capillaroscopy Results Matched with In Vitro Parameters*

Figure 3a–c shows the RBC aggregation parameters plotted as functions of CBV and the Pearson's r coefficient for each trend. AI for all the presented groups decreased with the increase of CBV, as indicated by the negative r. $T_{1/2}$, on the other hand, increased and had positive r values. $T_{agg}$ remained constant for the whole CBV range. These results show that for patients with high CBV the aggregation process in vitro was weaker compared to the patients with low CBV: The aggregation was less numerous and the doublet formation took longer.

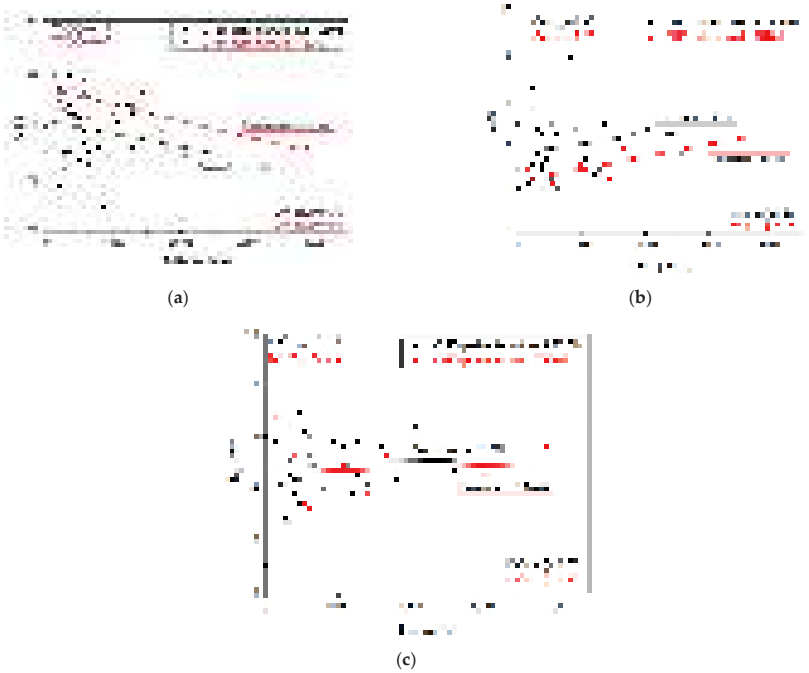


**Figure 3.** The individual values of AI (**a**), $T_{1/2}$ (**b**), and $T_{agg}$ (**c**) for groups of patients with and without T2DM versus the CBV. The linear fit and the Pearson's r coefficient are shown. CHD—coronary heart disease; T2DM—type 2 diabetes mellitus; CBV—capillary blood velocity.

No statistically significant difference in aggregation was found between several patient subgroups, including the division by gender and smoking habits. AI weakly correlated with BMI (Pearson's r = 0.29) and did not correlate with age (r = −0.05).

## 4. Discussion

In vitro and in vivo aggregation conditions are, of course, different due to the channel shape, presence, or absence of an endothelium layer, surrounding medium, etc. [21]. Moreover, in vivo aggregation in big vessels differs from the aggregation in capillaries [3]. In this study, we investigated in vivo RBC aggregation in nailfold capillaries, therefore excluding effects that can be observed in big vessels, such as axial migration of RBC, etc. [3]. Hemorheological parameters (including blood flow in capillaries) show alterations in pathophysiological processes in a complex way [22]. That is why our data could have provided contradictory results if we had not used criteria for exclusion (mentioned above in Section 2. Materials and Methods 2.1. Patients).

We found correlations between blood flow parameters measured in vitro and in vivo, as well as significant differences between the control group and CHD patients with and without T2DM. Firstly, the RBC aggregation in CHD patients was enhanced compared to the healthy volunteers (see Table 2). The increase in RBC aggregation has already been linked to cardiovascular diseases, including CHD and arterial hypertension using different techniques [23–25]. However, the relationship between aggregation and pathologies is yet to be established—article [26] suggests that aggregation and pathologies are not linked directly but rather share the same factors, such as obesity and cigarette smoking, among others. We found only a weak correlation for these factors and aggregation in CHD patients.

Secondly, the presence of T2DM had a significant effect on aggregation properties: Both AI and $T_{1/2}$ were higher ($p < 0.05$) compared to the patients without it (see Table 3). Of course, the effect of T2DM on RBC aggregation is already established [27], but being able to detect it specifically for CHD patients opens many doors in terms of diagnostics and monitoring the discussed pathologies. Two other parameters ($T_{agg}$ and CBV) did not show significant differences; this could be in part due to the methodology. Both LT and capillaroscopy study a limited number of RBCs, whereas laser aggregometry analyzes ensembles of tens of thousands. A high uncertainty in $T_{agg}$ and CBV demonstrated a great variation of RBC properties for each individual patient, which could have been caused by his or her health status. It could also mean that the effect of elevated aggregation was clearer during the later stages of aggregate formation (3D aggregate structures) than in the initial doublet formation.

Higher CBV means lower friction in the vessels and therefore weaker RBC aggregation [2]. This was clearly manifested for patients with T2DM in Figure 3 by the negative correlation with AI (r = −0.81) and positive correlation of $T_{1/2}$ (r = 0.82). For patients with a high CBV it was more likely that their RBC aggregation be more numerous and take less time for a large ensemble. $T_{agg}$ measured with LT did not correlate with CBV for all groups.

Additionally, it is important to mention the differences of blood temperature during measurement of different in vitro parameters. RheoScan parameters (AI and $T_{1/2}$) were measured at 37 °C, whereas the LT parameter ($T_{agg}$) was measured at room temperature at 22 °C. Because the aggregation depends on the temperature, these different conditions might have influenced the obtained data [3,28]. For example, RheoScan parameters (AI and $T_{1/2}$) greatly depend on temperature [28]. However, in our previous work [29] it was shown that for LT measurements the temperature-dependent change of the RBC aggregation was nearly absent for the temperatures of 20 °C and 38 °C. This means that we could compare all in vitro parameters between each other as if they were measured at the same temperatures.

The novelty of the presented work consists of a complex analysis of in vitro and in vivo parameters for different pathologies. The results of studies performed by alternative methods do not contradict our conclusions and show increased aggregation of RBCs in patients with CHD (including various complications) compared to healthy donors [3,30–32].

One of the limitations of the study is the small number of patients with both CHD and T2DM; in the future, we plan to increase this number. This will allow for grouping the patients by specific medication used, such as antiaggregants and anticoagulants. Another point that can be improved is the observation of additional factors that influence the blood flow, for example plasma components [3,33]. In addition, BMI and other factors influence platelet activation and aggregation [34], which can indirectly affect the aggregation of RBCs; this was not accounted for in this article.

## 5. Conclusions

In this work, the aggregation of red blood cells was studied using different optical in vivo and in vitro measurement techniques. The aggregation for patients with coronary heart disease was statistically significantly enhanced compared to the control group. In vivo and in vitro methods yielded correlated results: The faster the cells moved in the capillaries, the less cells aggregated in vitro. Type 2 diabetes mellitus had an additional significant effect on the aggregation properties of coronary heart disease patients. These findings are prominent for diagnosing and monitoring the state of patients with pathologies that affect blood properties.

**Author Contributions:** This paper is a result of the cooperation and contribution of all authors. Conceptualization, A.P. (Alexander Priezzhev), and Y.G.; investigation, P.E., A.M., and Y.G.; methodology, M.S., supervision, A.P. (Alexandra Pigurenko) and A.L. All authors have read and approved the published version of the manuscript.

**Funding:** This research was funded by RFBR, grant number 19-52-51015.

**Institutional Review Board Statement:** The study was conducted according to the guidelines of the Declaration of Helsinki, and approved by the Ethics Committee of the medical research and educational center of M.V. Lomonosov Moscow State University, Moscow, Russia (protocol code: 1/19, date of approval: 18 February 2019).

**Informed Consent Statement:** Informed consent was obtained from all subjects involved in the study.

**Data Availability Statement:** The data presented in this study are available on request from the corresponding author. The data are not publicly available due to the ethical and privacy issues.

**Acknowledgments:** The authors would like to extend thanks for the financial support provided to this study by RFBR (19-52-51015).

**Conflicts of Interest:** The authors declare no conflict of interest. The funders had no role in the design of the study; in the collection, analyses, or interpretation of data; in the writing of the manuscript, or in the decision to publish the results.

## References

1. Tuchin, V. (Ed.) *Handbook of Optical Biomedical Diagnostics*; SPIE: Bellingham, WA, USA, 2016; Volume 2.
2. Patrícia, S.; Fernando, P.; Manuel, A.; Mónica, O. A review of hemorheology: Measuring techniques and recent advances. *Korea-Aust. Rheol. J.* **2016**, *28*, 1–22. [CrossRef]
3. Baskurt, O.; Neu, B.; Meiselman, H. *Red Blood Cell Aggregation*; CRC Press: Boca Raton, FL, USA, 2012.
4. Priezzhev, A.; Lee, K.; Firsov, N.; Lademann, J. Optical Study of RBC Aggregation in Whole Blood Samples and Single Cells. In *Handbook on Optical Biomedical Diagnostics*, 2nd ed.; Tuchin, V., Ed.; SPIE Press: Bellingham, WA, USA, 2016; pp. 5–36.
5. Muravyov, A.; Tikhomirova, I.; Maimistova, A.; Bulaeva, S.; Mikhailov, P.; Kislov, N. Red blood cell aggregation changes are dependent on its initial value: Effect of long-term drug treatment and short-term cell incubation with drug. *Clin. Hemorheol. Microcirc.* **2011**, *48*, 231–240. [CrossRef] [PubMed]
6. Hochmuth, R. Micropipette aspiration of living cells. *J. Biomech.* **2000**, *33*, 15–22. [CrossRef]
7. Kyriacou, P.; Budidha, K.; Abay, T.Y. Optical Techniques for Blood and Tissue Oxygenation. *Ref. Modul. Biomed. Sci.* **2019**, *3*, 461–472. [CrossRef]
8. Gurfinkel, Y.; Suchkova, O.; Sasonko, M.; Priezzhev, A. Implementation of digital optical capillaroscopy for quantifying and estimating the microvascular abnormalities in diabetes mellitus. *Proc. SPIE SFM 2015* **2015**, *9917*, 991703. [CrossRef]
9. Baskurt, O.; Boynard, M.; Cokelet, G.; Connes, P.; Cooke, B.; Forconi, S.; Liao, F.; Hardeman, M.; Jung, F.; Meiselman, H.; et al. New guidelines for hemorheological laboratory techniques. *Clin. Hemorheol. Microcirc.* **2009**, *42*, 75–97. [CrossRef] [PubMed]

10. Shin, S.; Yang, Y.; Suh, J. Measurement of erythrocyte aggregation in a microchip stirring system by light transmission. *Clin. Hemorheol. Microcirc.* **2009**, *41*, 197–207. [CrossRef]
11. Lopatin, V.V.; Priezzhev, A.V. Multiple light scattering by suspensions of erythrocytes in geometrical optics approximation. *Proc. SPIE* **2002**, *4749*, 267–274. [CrossRef]
12. Lopatin, V.N.; Priezzhev, A.V.; Aponasenko, A.D.; Shepelevich, N.V.; Lopatin, V.V.; Pozhilenkova, P.V.; Prostakova, I.V. *Metody Svetorassejanija v Analize Dispersnykh Biologicheskikh Sred*; Fizmatlit: Moscow, Russia, 2004. (In Russian)
13. Mauer, J.; Peltomäki, M.; Poblete, S.; Gompper, G.; Fedosov, D.A. Static and dynamic light scattering by red blood cells: A numerical study. *PLoS ONE* **2017**, *12*, e0176799. [CrossRef]
14. Ashkin, A.; Dziedzic, J. Optical trapping and manipulation of single living cells using infra-red laser beams. *Berichte der Bunsen-Gesellschaft für Physikalische Chemie* **1989**, *98*, 254–260. [CrossRef]
15. Arne, G. (Ed.) *Optical Tweezers. Methods and Protocols*; Humana Press: New York, NY, USA, 2017.
16. Ermolinskiy, P.; Lugovtsov, A.; Maslyanitsina, A.; Semenov, A.; Dyachuk, L.; Priezzhev, A. Interaction of erythrocytes in the process of pair aggregation in blood samples from patients with arterial hypertension and healthy donors: Measurements with laser tweezers. *J. Biomed. Photonics Eng.* **2018**, *4*, 030303. [CrossRef]
17. Lee, K.; Kinnunen, M.; Khokhlova, M.; Lyubin, E.; Priezzhev, A.; Meglinski, I.; Fedyanin, A. Optical tweezers study of red blood cell aggregation and disaggregation in plasma and protein solutions. *J. Biomed. Opt.* **2016**, *21*, 035001. [CrossRef] [PubMed]
18. Grover, S.; Gauthier, P.; Skirtach, A. Analysis of the behaviour of erythrocytes in an optical trapping system. *Opt. Express* **2000**, *7*, 533–539. [CrossRef]
19. Gurfinkel, Y.; Sasonko, M. Potentialities of Digital Capillaroscopy in the Diagnostics of Oedema Syndrome. *J. Biomed. Photonics Eng.* **2017**, *3*, 030401. [CrossRef]
20. Parker, M.J.S.; McGill, N.W. *The Established and Evolving Role of Nailfold Capillaroscopy in Connective-Tissue Disease. Chapter in book Connective-Tissue Disease, Connective Tissue Disease—Current State of the Art, Akira Takeda*; IntechOpen: Rijeka, Croatia, 2018.
21. Baskurt, O.K. In vivo correlates of altered blood rheology. *Biorheology* **2008**, *45*, 629–638. [CrossRef] [PubMed]
22. Nemeth, N.; Deak, A.; Szentkereszty, Z.; Peto, K. Effects and influencing factors on hemorheological variables taken into consideration in surgical pathophysiology research. *Clin. Hemorheol. Microcirc.* **2018**, *69*, 133–140. [CrossRef] [PubMed]
23. Hahn, R.; Müller-Seydlitz, P.M.; Jöckel, K.H.; Hubert, H.; Heimburg, P. Viscoelasticity and red blood cell aggregation in patients with coronary heart disease. *Angiology* **1989**, *40*, 914–920. [CrossRef]
24. Cicco, G.; Pirrelli, A. Red Blood Cell (RBC) Deformability, RBC Aggregability and Tissue Oxygenation in Hypertension. *Clin. Hemorheol. Microcirc.* **1999**, *21*, 169–177.
25. Arbel, Y.; Banai, S.; Benhorin, J.; Finkelstein, A.; Herz, I.; Halkin, A.; Keren, G.; Yedgar, S.; Barshtein, G.; Berliner, S. Erythrocyte aggregation as a cause of slow flow in patients of acute coronary syndromes. *Int. J. Cardiol.* **2011**, *154*, 322–327. [CrossRef]
26. Bogar, L. Hemorheology and hypertension: Not "chicken or egg" but two chickens from similar eggs. *Clin. Hemorheol. Microcirc.* **2002**, *26*, 81–83.
27. Li, Q.; Li, L.; Li, Y. Enhanced RBC Aggregation in Type 2 Diabetes Patients. *J. Clin. Lab. Anal.* **2015**, *29*, 387–389. [CrossRef] [PubMed]
28. Ermolinkiy, P.B.; Semenov, A.N.; Lugovtsov, A.E.; Poeschl, C.; Windberger, U.; Kaliviotis, E.; Priezzhev, A.V. Effect of different macromolecules on viscous and microrheologic properties of blood at various temperatures. *Proc. SPIE* **2019**, *11065*, 1106507.
29. Lee, K.; Priezzhev, A.; Shin, S.; Yaya, F.; Meglinsky, I. Characterization of shear stress preventing red blood cells aggregation at the individual cell level: The temperature dependence. *Clin. Hemorheol. Microcirc.* **2016**, *64*, 853–857. [CrossRef] [PubMed]
30. Yang, Q.; Wang, J.H.; Huang, D.D.; Li, D.G.; Chen, B.; Zhang, L.M.; Yuan, C.L.; Cai, L.J. Clinical significance of analysis of the level of blood fat, CRP and hemorheological indicators in the diagnosis of elder coronary heart disease. *Saudi J. Biol. Sci.* **2018**, *25*, 1812–1816. [CrossRef] [PubMed]
31. Brun, J.F.; Varlet-Marie, E.; Raynaud de Mauverger, E.; Mercier, J. Both overall adiposity and abdominal adiposity increase blood viscosity by separate mechanisms. *Clin. Hemorheol. Microcirc.* **2011**, *48*, 257–263. [CrossRef] [PubMed]
32. Koscielny, J.; Jung, E.M.; Mrowietz, C.; Kiesewetter, H.; Latza, R. Blood fluidity, fibrinogen, and cardiovascular risk factors of occlusive arterial disease: Results of the Aachen study. *Clin. Hemorheol. Microcirc.* **2004**, *31*, 185–195.
33. Kwaan, H.C. Role of plasma proteins in whole blood viscosity: A brief clinical review. *Clin. Hemorheol. Microcirc.* **2010**, *44*, 167–176. [CrossRef]
34. Haszon, I.; Papp, F.; Kovács, J.; Bors, M.; Németh, I.; Bereczki, C.; Túri, S. Platelet aggregation, blood viscosity and serum lipids in hypertensive and obese children. *Eur. J. Pediatr.* **2003**, *162*, 385–390. [CrossRef]

diagnostics

MDPI

Article

# Diagnostic Accuracy of Cross-Polarization OCT and OCT-Elastography for Differentiation of Breast Cancer Subtypes: Comparative Study

**Ekaterina V. Gubarkova [1,*], Elena B. Kiseleva [1], Marina A. Sirotkina [1], Dmitry A. Vorontsov [2], Ksenia A. Achkasova [1], Sergey S. Kuznetsov [3], Konstantin S. Yashin [4], Aleksander L. Matveyev [5], Aleksander A. Sovetsky [6], Lev A. Matveev [6], Anton A. Plekhanov [1], Alexey Y. Vorontsov [2], Vladimir Y. Zaitsev [6] and Natalia D. Gladkova [1]**

1 Institute of Experimental Oncology and Biomedical Technologies, Privolzhsky Research Medical University, 603950 Nizhny Novgorod, Russia; kiseleva84@gmail.com (E.B.K.); sirotkina_m@mail.ru (M.A.S.); achkasova.k@bk.ru (K.A.A.); strike_gor@mail.ru (A.A.P.); natalia.gladkova@gmail.com (N.D.G.)
2 Department of Oncology, Nizhny Novgorod Regional Oncologic Hospital, 603126 Nizhny Novgorod, Russia; dr.vorontsovdmitriy@rambler.ru (D.A.V.); doctorvorontsov@mail.ru (A.Y.V.)
3 Department of Pathology, Privolzhsky Research Medical University, 603950 Nizhny Novgorod, Russia; zunek@mail.ru
4 University Clinic, Privolzhsky Research Medical University, 603950 Nizhny Novgorod, Russia; jashinmed@gmail.com
5 Laboratory of Multidimensional Signal Processing, Institute of Applied Physics of the Russian Academy of Sciences, 603950 Nizhny Novgorod, Russia; matveyev@appl.sci-nnov.ru
6 Laboratory of Wave Methods for Studying Structurally Inhomogeneous Media, Institute of Applied Physics of the Russian Academy of Sciences, 603950 Nizhny Novgorod, Russia; alex.sovetsky@mail.ru (A.A.S.); lionnn52rus@mail.ru (L.A.M.); vyuzai@ipfran.ru (V.Y.Z.)
* Correspondence: kgybarkova@mail.ru

Received: 1 October 2020; Accepted: 19 November 2020; Published: 24 November 2020

**Abstract:** The possibility to assess molecular-biological and morphological features of particular breast cancer types can improve the precision of resection margin detection and enable accurate determining of the tumor aggressiveness, which is important for treatment selection. To enable reliable differentiation of breast-cancer subtypes and evaluation of resection margin, without performing conventional histological procedures, here we apply cross-polarization optical coherence tomography (CP-OCT) and compare it with a novel variant of compressional optical coherence elastography (C-OCE) in terms of the diagnostic accuracy (Ac) with histological verification. The study used 70 excised breast cancer specimens with different morphological structure and molecular status (Luminal A, Luminal B, Her2/Neo+, non-luminal and triple-negative cancer). Our first aim was to formulate convenient criteria of visual assessment of CP-OCT and C-OCE images intended (i) to differentiate tumorous and non-tumorous tissues and (ii) to enable more precise differentiation among different malignant states. We identified such criteria based on the presence of heterogeneities and characteristics of signal attenuation in CP-OCT images, as well as the presence of inclusions/mosaic structures combined with visually feasible assessment of several stiffness grades in C-OCE images. Secondly, we performed a blinded reader study of the Ac of C-OCE versus CP-OCT, for delineation of tumorous versus non-tumorous tissues followed by identification of breast cancer subtypes. For tumor detection, C-OCE showed higher specificity than CP-OCT (97.5% versus 93.3%) and higher Ac (96.0 versus 92.4%). For the first time, the Ac of C-OCE and CP-OCT were evaluated for differentiation between non-invasive and invasive breast cancer (90.4% and 82.5%, respectively). Furthermore, for invasive cancers, the difference between invasive but low-aggressive and highly-aggressive subtypes can be detected. For differentiation between non-tumorous tissue and low-aggressive breast-cancer subtypes, Ac was 95.7% for C-OCE and 88.1% for CP-OCT. For differentiation between non-tumorous tissue and highly-aggressive breast cancers, Ac was found to be 98.3% for C-OCE and

97.2% for CP-OCT. In all cases C-OCE showed better diagnostic parameters independently of the tumor type. These findings confirm the high potential of OCT-based examinations for rapid and accurate diagnostics during breast conservation surgery.

**Keywords:** breast cancer; cross-polarization optical coherence tomography (CP-OCT); compressional optical coherence elastography (C-OCE); image assessment

## 1. Introduction

Intraoperative detection of breast malignancy margins would allow minimization of the risk of tumor recurrence in patients undergoing breast conservation surgery (BCS). Intraoperative pathological estimation can be performed through frozen section analysis and imprint cytology [1]; however, these techniques are characterized by several restrictions such as resource intensity, sampling only a small percentage of the surgical margins and limited efficacy, especially for ductal carcinoma in situ (DCIS) [2]. Consequently, these methods have not been widely adopted [3]. Fluorescent techniques that utilize molecular contrast, potentially affording surgeons to visualize tumor in the cavity, are currently in the development [4,5]. Ultrasound elastography has been developed for a number of applications, and specifically for preoperative diagnosis of breast lesions [6–8]. However, its relatively low spatial resolution makes it inappropriate to use this method for intraoperative tumor margin assessment.

Optical coherence tomography (OCT) presents a very promising method for surgical tasks solving due to the clear benefits of this method such as: safety (using a near infrared light source does not risk tissue damage); accuracy (high resolution ~10–15 micron); there being no need for contrast agents; and the short duration of image attainment. OCT can be used both in the resected specimen of tumor and in the surgical cavity. OCT can be added to biopsy needle probes and can be used to guide correct sampling of tumor biopsies [9–11]. OCT is a promising method for intraoperative guidance during the resection of breast cancer and for identifying positive margins in specimens from BCS [12–15]. Recently, OCT has been proposed for intraoperative use in distinguishing tumorous and non-tumorous tissues using handheld probes [16,17]. To overcome the limited imaging depth ~2 mm typical for OCT (which usually requires sufficiently close approaching of the OCT probe towards the studied tissue), utilization of endoscopic and/or needle OCT probes are considered [11]. Moreover, it is known that structural OCT scans exhibit low contrast between tumor and uninvolved dense stromal tissue, which makes it challenging to accurately assess margin status [18]. In view of this, improvements in several aspects of OCT attract much attention, in particular, the development of functional OCT extensions based on polarization effects and stiffness analysis as considered below.

Based on the birefringence of the tissue structure, polarization-sensitive (PS) OCT provides advanced imaging of collagen fibers in the breast tissue and enhances intraoperative differentiation of breast cancer [19–21]. Stroma state assessment is fundamentally important, because tumor collagen matrix plays a crucial role in breast cancer invasion and metastatic spreading [22]. Several studies have developed quantitative diagnosis algorithms for intraoperative assessing breast cancer margins and validated them against OCT, both alone and in combination with other modalities [23]. Cross-polarization OCT (CP-OCT) is a variant of PS OCT that allows imaging of the initial polarization state changes due to both birefringence and cross-scattering in biological tissues [24]. Only orthogonally polarized backscattered light, which is mutually coherent with the incident wave, contributes to the cross-polarized (CP) OCT image. CP-OCT is a promising method for differentiating tumorous from non-tumorous tissues in human breast tissues [25], human brain tissues [26,27], as well as for diagnosis of bladder cancer [28–31]. OCT can also measure attenuation, which can be helpful for improving contrast of breast imaging research [32,33].

Attention to the problem of determining tissue stiffness (elastographic mapping) by optical coherence elastography (OCE) methods has been increasing in recent years [34–37]. Sufficiently high

resolution of quantitative stiffness maps enabled by compressional OCE opened the possibility to perform morphological segmentations of tumor tissue constituents very similar to morphological segmentation of conventional histological images [25,38,39]. In these studies of experimental tumor models on animals, this technique allowed in vivo monitoring of morphological variation in tumor tissue during tumor growth and response to therapies. In studies [25,40–42], application of compressional OCE (C-OCE) for characterization of mechanical properties of excised human breast cancer specimens was demonstrated. New possibilities for intraoperative assessment of the breast cancer borders by means of optical coherence micro-elastography (OCME) were reported in a recent study [43,44]. It has been demonstrated that OCME provides additional contrast of tumor compared to OCT alone. Additionally, the potential of OCME images for evaluation of tumor margins in specimens excised during BCS was demonstrated in [41,43]. In our previous paper it was shown that CP-OCT and C-OCE can be helpful in breast cancer margin identification, as well as for grading breast cancer subtypes [25].

For more accurate evaluation of the resection margin, it is advantageous to take into account the genetic heterogeneity of breast cancer, as well as the variety of molecular-biological and morphological features influencing prognosis of the disease course (degree of aggressiveness) and treatment selection [45,46]. Indeed, it was demonstrated that probability of tumor recurrence mainly depends on molecular-biological characteristic of the tumor [47,48], while an increase in the size of the removed tissue, free of cancer cells, is not associated with a decrease in the recurrence rate [49].

Various molecular-biological and morphological features of breast cancer are anticipated to differently influence the polarizing and elastic tumor and peritumoral tissue qualities. This stimulates interest in evaluation of the clinical potential of polarization-sensitive and elastographic OCT techniques for determining breast cancer subtypes (malignancy grade) and improving tumor boundary detection based on the ability of these methods to identify different tumor subtypes. In this way, surgeons are expected to be provided with essential information that can improve reliability of the positive resection margin detection during BCS, at least for some breast cancer subtypes.

The goals of this research are (1) to define the visual assessment criteria required for the CP-OCT and C-OCE images in order to enable differentiation among various breast cancer subtypes; (2) to determine the diagnostic accuracy (sensitivity and specificity) of C-OCE in comparison with CP-OCT, for delineation of tumorous and non-tumorous breast tissues and subsequent identification of breast cancer subtypes in a blinded reader study.

## 2. Materials and Methods

### *2.1. Human Breast Specimens*

This study was approved by the institutional review board of the Privolzhsky Research Medical University (Protocol #10 from 28 September 2018). All of the patients included in the study provided written informed consent. A total of 70 breast tumor tissue specimens were taken from 50 patients post partial ($n$ = 35) or complete ($n$ = 15) mastectomy with different diagnosis (Table 1). To minimize the effect tissue degrading, the excised specimens were immediately placed in gauze saturated with phosphate buffer and closed to prevent dehydration. CP-OCT and C-OCE images of the fresh, un-fixed breast tissue were acquired within 2 h after surgical excision. The studies were done on specimens with sizes from 0.5 × 1 cm to 1 × 2 cm. Specimens were taken from central zone of tumors for diagnostics of breast cancer subtypes and in the peritumoral area for visualization of normal (non-tumorous) breast tissue. A special motorized table for convenient positioning the specimen under the OCT probe was used. The entire CP-OCT and C-OCE study of each specimen was no longer than 20 min (including preliminary sample preparation and orientation).

**Table 1.** Clinical specimens' characteristics and number of imaged specimens.

| Diagnosis | Number of Specimens | Age of Patients (Range) | Tumor Size |
|---|---|---|---|
| **Benign breast conditions** | | | |
| Non-tumorous breast tissue | 20 | 43–68 | - |
| Fibroadenoma/fibroadenomatosis | 4 | 35–48 | ≤1 cm |
| **Malignant breast lesions** | | | |
| Ductal carcinoma in situ (DCIS) | 5 | 44–63 | ≤1 cm |
| Invasive ductal carcinoma (IDC) of scirrhous structure | 24 | 41–82 | ≤2 cm |
| Invasive ductal carcinoma (IDC) of solid structure | 10 | 41–82 | ≤2 cm |
| Invasive lobular carcinoma (ILC) of solid structure | 7 | 48–72 | ≤2 cm |

### *2.2. Multimodal OCT Device*

This study used a common path spectral domain multimodal OCT system with a central wavelength of 1310 nm and spectral width of 100 nm, with an axial resolution of 10 μm, lateral resolution is 15 μm, a scanning depth of 2 mm in air, a scanning speed of 20,000 A-scans per second. The OCT-system acquired 3D blocks of OCT data, 2 mm in depth (in air) over 2.4 × 2.4 $mm^2$ area and 2D lateral scanning with a similar field of view were acquired in 26 s. The CP-OCT and C-OCE images were generated in real time during the acquisition process. For living tissues, real-time angiographic imaging was also possible by processing the same data [50]. For the described OCT studies, the total scanning time along a 1–2 cm trajectory on a biopsy sample was 3–5 min depending on the number of stitched images.

Structural 2D (cross-sectional images) CP-OCT images were constructed in two virtual channels, one of which was co-polarized with the incident polarization (co-polarization channel) and the other one was orthogonal (cross-polarization channel) to the incident polarization, respectively [24]. CP-OCT aims to obtain the information contained in the cross-polarization channel, which allows one to form cross-polarization images caused by birefringence of the tissue from optically anisotropic structures (evaluate the state of connective tissue component), as well as due to contribution of coherent cross-polarization backscattering on non-spherical particles and particles with dimensions much larger than the wavelength. In view of low informativity of the co-polarization images (as found in previous studies [25]), only cross-polarization images were used for diagnostic conclusions in this study.

An advanced variant of phase-sensitive compression OCE [37,39,51–55] was used to visualize inter-frame strains in the tissue and subsequently map the Young modulus. The probe was slightly pressed onto the studied sample surface, and strain distribution in the probe vicinity was reconstructed. Strain mapping was based on estimation of axial gradients of interframe phase variations of the OCT signal using the "vector" method [51,53]. The name "vector" is due to the fact that, without explicitly singling out amplitude and phase, the complex-valued OCT signals in this method are considered as vectors in the complex plane, and the phase is singled out at the very last step of the processing. Such vector representation allows one to perform flexibly-tuned amplitude-weighted averaging over the processing-window area. As a result, noisy contributions of small-amplitude pixels and, at the same time, especially strong phase errors (by ~π rad.) are very efficiently suppressed. This allows obtaining strain maps with fairly high quality even without periodic averaging (which is very important for the one-directional single-step loading of the tissue used in the described studies). In addition to the exceptionally high tolerance to various measurement noises, the vector method is very efficient computationally, so that the elastographic processing of the acquired sequence of several hundreds of OCT scans requires ~5–10 s using a "typical" PC without the necessity of GPU computations.

Another important point is that the estimated interframe phase-variation gradient is averaged over a processing window, the dimensions of which being the main factor determining the resolution of the resultant OCE scans. For a rectangular processing window with comparable axial and lateral

sizes, the resolution in strain maps is also comparable in these directions and corresponds to ~$\frac{1}{2}$ of the window size. For the described system, the window size was ~90–100 μm, which defined the strain-mapping resolution ~45–50 μm. Such a window size was chosen empirically as a compromise between worse quality of the OCE-images for smaller windows (because of insufficiently averaged noise) and too-strong smoothing of spatial inhomogeneities for larger windows.

The next important point is quantification of the tissue Young's modulus, to enable which a reference silicone layer with preliminary calibrated stiffness (with the Young's modulus in the range 50–100 kPa) was used as described in [42,54–56]. Of key importance in the used variant of C-OCE technique is that all OCE images are formed using a pre-selected pressure level (4 kPa in the described study) standardized over the entire image area, despite the fact that for real OCE scans, the local pressure over the lateral coordinate usually varies several times because of the non-ideally planar boundary of the sample, its mechanical inhomogeneity, etc. The pressure standardization technique is based on the usage of the reference silicone layer as a sensor of local pressure as described in detail in [55]. To synthesize such a single "standardized OCE image", a series of initial structural OCT-scans acquired during monotonic compression of the sample was first processed to obtain a series of cumulative-strain maps as described in [54,57,58]. Then vertical A-scans corresponding to the selected pressure were picked up from the initial series of cumulative-strain maps and reassembled to synthesize a single cumulative-strain image in which all A-scans now correspond to the same preselected pressure onto the tissue [55]. To be sure that the strain in silicone can be considered linearly proportional to stress (pressure), high linearity of silicone was specially verified as described in [42,54,55]. Real biological tissues usually demonstrate a pronouncedly nonlinear stress–strain law. The described C-OCE method allows one to determine this law by plotting the strain in the linear precalibrated silicone against strain in any region of interest in the tissue beneath the silicone. The elasticity of the tissue can then be estimated as the tangent Young's modulus (the slope of the stress-strain curve) corresponding to the desired pre-selected pressure. It was empirically found that for breast-cancer tissue the sought tangent modulus could be conveniently estimated as the slope of the chorde corresponding to the pressure range 4 ± 1 kPa. At lower pressures, very small strain of stiffer regions was difficult to estimate, whereas at higher pressures, the elasticity contrast among various tumor components became worse because of strong nonlinearity-induced stiffening of the initially softer components of the tumor (see examples in [55]). Without such standardization the intrinsic elastic nonlinearity of breast-cancer tissues may result in uncontrollable variability of the estimated elastic modulus in different measurements and even different parts of the same image. This unpredictable variability may be rather significant (several times and greater) even for apparently moderate strains within a few percent [42,55]. Thus, the developed pressure-standardization procedures were critically important for enabling meaningful quantitative comparisons of elastographic data obtained from different measurements.

The so-obtained OCE-images were represented in the color-coded form, such that stiffer areas (those with weaker strain) are shown in blue, and soft areas, where deformation is greater, are shown in red.

### *2.3. Histological Study*

After CP-OCT and C-OCE imaging of the freshly-excised sample with yet non-modified optical and biomechanical properties, the scanned area was marked on the specimen with histological ink. Then the specimen was fixed in 10% formalin for 48 h and resectioned through the marked area, so that the plane of the histological sections coincided to the cross-sectional CP-OCT and C-OCE images. For the histological evaluation, haematoxylin and eosin (H&E) staining was used. Two independent histopathologists interpreted the histological slices photographed in transmitted light with a Leica DM2500 DFC (Leica Microsystems, Wetzlar, Germany) microscope, equipped with a digital camera. Based on histopathological analysis, all samples were classified into tumorous and non-tumorous breast tissues. The revealed histological types of breast tissue include: adipose tissue with streaks of

connective tissue (number of specimens $n = 20$); fibroadenomatosis/fibroadenoma ($n = 4$); DCIS ($n = 5$); invasive lobular carcinoma (ILC) ($n = 7$); invasive ductal carcinoma (IDC) of scirrhous ($n = 24$) and solid ($n = 10$) structure (Table 1). In addition, to assess tumor aggressiveness (prognosis of the disease course) immunohistochemistry (for $n = 46$ samples) was performed, identifying five molecular subtypes of the tumors: Luminal A, Luminal B (Her2/Neo-), Her2/Neo+, Non-luminal, Triple-negative cancer (TNC). Luminal A and Luminal B (Her2/Neo-) are reported to be low-aggressive tumors characterized by predominantly favorable prognosis of disease course and treatment in comparison with Her2/Neo+, Non-luminal and TNC [24]. Furthermore, it should be noted that Luminal A and Luminal B subtypes were characterized by scirrhous architectonics, while Her2/Neo+, Non-luminal, TNC had solid structure.

The results of histopathology were compared with the corresponding CP-OCT-based and C-OCE-based findings. For the blinded reader study, all images were divided into 4 groups: adipose and normal stromal breast tissue, benign breast tissue (fibroadenoma/fibroadenomatosis), non-invasive DCIS, and images portraying cancerous features of invasive low and highly-aggressive breast cancer.

### 2.4. Reader Analysis of CP-OCT and C-OCE Images

A blinded reader study was performed to evaluate the statistical performance of assessing tumorous and non-tumorous breast tissues based on the CP-OCT imaging (first test) and C-OCE visualization (second test). In the study, 115 CP-OCT and 115 C-OCE images from 50 patients were interpreted by 6 readers specially trained for this OCT-based assessment (2 biologists experienced in optical imaging, but unskilled in recognizing breast cancer pathology; 2 post-graduate students of the Medical University unexperienced both in optical imaging and in recognizing breast cancer pathology; 2 surgeons skilled in detecting breast cancer pathology, but without work experience in optical imaging) who were unaware whether the image contained cancer or not. The readers were given a training set of sample CP-OCT and C-OCE images (3 images of each histological type of breast tissue).

The criteria evaluated by the readers are summarized in Tables 2 and 3. Each image group had its own set of visual criteria. The reader's goal was to distinguish between tumorous and non-tumorous breast tissues. If an image was considered to represent non-tumorous breast tissue, the reader indicated a score of "0" whether it was normal breast tissue or fibroadenoma. If the reader identified malignant lesion marks, a score from "1" to "3" was assigned to the sample depending on the estimated tumor aggressiveness. The score of "1" means that the reader thinks that the image represents non-invasive DCIS; a score of "2" means that the reader considers the cancer to be invasive, but less aggressive; a score of "3" means that the reader thinks that invasive cancer is more aggressive.

The first test was based on assessment of signal architecture in cross- polarization images (Table 2). The cross-polarization channel enables more contrast visualization of the presence and state of connective tissue in comparison with the co-polarization OCT images.

Structural features in the CP-OCT images were distinguished by the following features of the scattering intensity and lateral uniformity of the signal attenuation (Table 2):

(i) the average level of the CP-OCT signal throughout the image is visually estimated as "low" like in Figure 1(b5) or "high" for the used 0–50 dB signal range, where "low" corresponded to intensities below 25 dB, i.e., the noise range in the used scale, and "high" related to the level above 25 dB on the used scale like in Figure 1(b2);

(ii) the presence of structures with a sharp boundary between contrasting-in-brightness regions with well-circumscribed boundary architecture like in Figure 1(b3) (which was graded as "yes"/"no");

(iii) the attenuation rate as estimated by the penetration depth of the probing radiation ("high" attenuation like in Figure 1(b5) and "low" like in Figure 1(b2));

(iv) the uniformity of attenuation along the interior border of the structural CP-OCT image ("uniform" like in Figure 1(b2)/"non-uniform" like in Figure 1(b4)).

**Table 2.** Visual assessment criteria of cross-polarization optical coherence tomography (CP-OCT) images for distinguishing between non-tumorous and tumorous breast tissue.

| | **Normal (Non-Tumorous) Breast Tissue (*n* = 20)** | **Fibroadenoma/ Fibroadenomatosis (*n* = 13)** | **DCIS (*n* = 10)** | **Low-Aggressive Invasive Breast Cancer (*n* = 47)** | **Highly-Aggressive Invasive Breast Cancer (*n* = 25)** |
|---|---|---|---|---|---|
| **Main criterion:** | | | | | |
| Typical architecture | honeycomb structure, areas of high intensity signal | predominance of areas with high signal intensity | alternating signal of high, medium and low intensity; the presence of structures with no signal with clear boundaries (ducts) | alternating signal of medium and low intensity | homogenous low intensity signal |
| **Additional criteria:** | | | | | |
| Signal penetration depth | high | high | high | high | low |
| Structures with clear (contrasting) boundaries | no | no | yes | no | no |
| Uniformity of the OCT signal attenuation along the inferior border of the image | uniform | uniform | highly uneven | non-uniform | uniform |
| Final score | 0 | 0 | 1 | 2 | 3 |

*n*—number of images.

**Table 3.** Visual assessment criteria of compressional optical coherence elastography (C-OCE) images for distinguishing between non-tumorous and tumorous breast tissue.

| | **Normal (Non-Tumorous) Breast Tissue (*n* = 20)** | **Fibroadenoma/ Fibroadenomatosis (*n* = 13)** | **DCIS (*n* = 10)** | **Low-Aggressive Invasive Breast Cancer (*n* = 47)** | **Highly-Aggressive Invasive Breast Cancer (*n* = 25)** |
|---|---|---|---|---|---|
| **Main criterion:** | | | | | |
| Typical stiffness pattern | uniform low stiffness level over the C-OCE image | | low stiffness level of the stiffness throughout the image with high-contrast zones with strongly increased stiffness | non-uniform high stiffness level over the C-OCE image | |
| **Additional criteria:** | | | | | |
| Predominance of uniform distribution of high stiffness values (>500 kPa) | no | no | no | no | yes |
| Presence of multiple moderately contrast inclusions of high stiffness (Mosaic structure) | no | no | no | yes | no |
| Final score | 0 | 0 | 1 | 2 | 3 |

*n*—number of images.

The second test was based on the analysis of stiffness values distributions on C-OCE images. Stiffness maps are presented in a color palette, where hard areas (blue—above 500 kPa) indicate the presence of tumor cells, and soft regions (red—below 100 kPa) represent adipose and connective tissues. At the same time, tissues with intermediate stiffness (the predominance of orange and yellow colors corresponding to ~200–400 kPa) correspond to the presence of such degenerative changes of breast-tissue stroma as fibrosis or hyalinosis of collagen fibers. The threshold values for stiffness (Table 3) of the main types of breast-tissue components were identified as described in detail in our previous work [25], in which accurate comparison of histological and OCE images was performed.

Main and additional criteria of subsuming the images to one or another group were formulated for cross-polarization and C-OCE images, the additional criteria of visual assessment being needed for more precise differentiation among different malignant states (Tables 2 and 3).

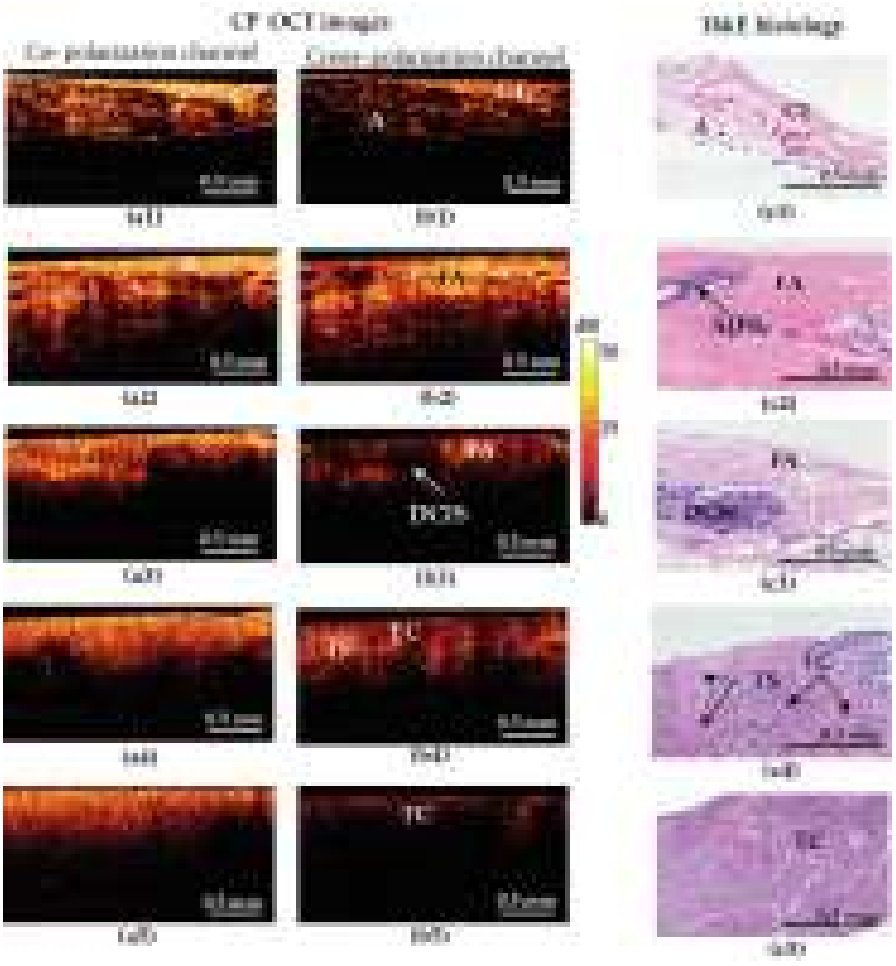


**Figure 1.** Representative depth-wise co- and cross-polarization OCT images (**a**,**b**) of non-tumorous and tumorous breast tissue with the corresponding histology (**c**). (**a1**–**c1**) Adipose tissue with streaks of connective tissue; (**a2**–**c2**) fibroadenomatosis/fibroadenoma; (**a3**–**c3**) DCIS; (**a4**–**c4**) invasive ductal carcinoma (IDC) of scirrhous structure (low-aggressive breast cancer subtype); (**a5**–**c5**) IDC of solid structure (highly-aggressive breast cancer subtype). (**a1**–**a5**) OCT images in co-polarization channel; (**b1**–**b5**) OCT images in cross-polarization channel; (**c1**–**c5**) histological images, haematoxylin and eosin (H&E) staining. Abbreviations: A—adipose, CT—connective tissue, FA—fibroadenomatosis, ADH—atypical ductal hyperplasia, DCIS—ductal carcinoma in situ, TS—tumor stroma, TC—cluster of tumor cells.

### *2.5. Statistical Analysis*

The results of the blinded reader study of CP-OCT and C-OCE images analysis were collected for determining the diagnostic accuracy for distinguishing: (1) non-tumorous breast tissues ($n$ = 33) from tumor ($n$ = 82); (2) non-invasive DCIS ($n$ = 10)) from invasive breast cancer ($n$ = 72); (3) low-aggressive invasive tumors (Luminal A, Luminal B (Her2/Neo-)) ($n$ = 47) with favorable prognosis from highly aggressive invasive tumors (Her2/Neo+, Non-luminal, TNC) ($n$ = 25) with unfavorable prognosis;

(4) non-tumorous breast tissues ($n$ = 33) from low-aggressive invasive tumors ($n$ = 47), and (5) non-tumorous breast tissues ($n$ = 33) from highly-aggressive invasive tumors ($n$ = 25).

The statistical analysis was performed using Statistica 10.0 and IBM SPSS Statistics software.

The assessment of the informative value and diagnostic capabilities of the studied methods (CP-OCT and C-OCE) was carried out with an estimation of their sensitivity (Se), specificity (Sp), and diagnostic accuracy (Ac). Based on the sensitivity and specificity values, Receiver operating characteristic (ROC) curves were constructed, which show the dependence of the number of true positive rate (TP) on the number of false positive rate (FN). For quantitative characterization of the ROC curves, we evaluated the area under the ROC curve (AUC), i.e., the area bounded by the ROC curve and the axis of the false positive rate [59]. The higher the AUC, the better the classifier is.

The inter-reader agreement was calculated using Cohen's kappa coefficient (k): $k \geq 0.81$—perfect agreement; $0.61 \leq k < 0.80$—substantial agreement; $k < 0.6$—poor agreement [60].

## 3. Results

### *3.1. Visual Assessment of the CP-OCT and C-OCE Images for Distinguishing between Non-Tumorous and Tumorous Breast Tissue*

The results based on the CP-OCT and C-OCE images for representative cases of the non-tumorous and tumorous breast tissue and differentiation among highly-aggressive breast-cancer subtypes are shown in Figures 1 and 2.

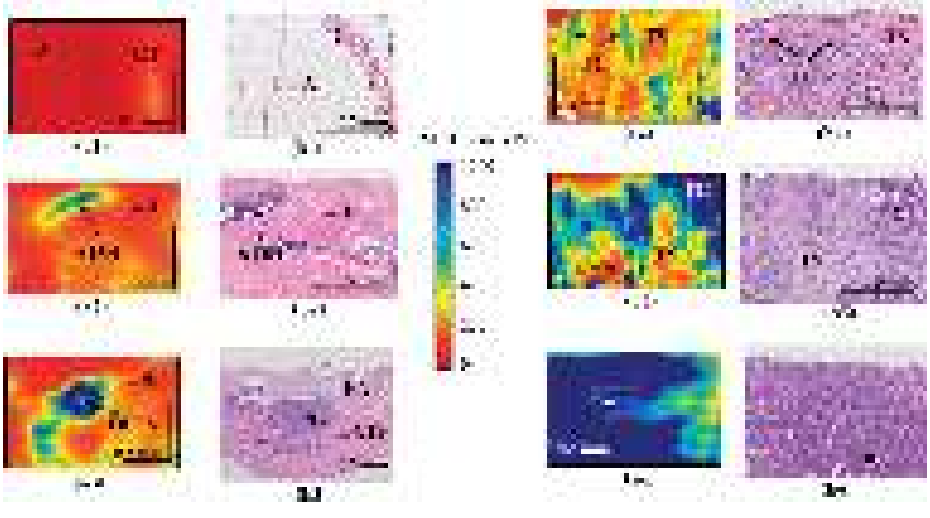

**Figure 2.** Representative depth-wise C-OCE images (**a1**–**a6**) of non-tumorous and tumorous breast tissue with corresponding histological images (**b1**–**b6**). (**a1**–**b1**) Adipose tissue with streaks of connective tissue; (**a2**–**b2**) fibroadenomatosis/fibroadenoma; (**a3**–**b3**) DCIS; (**a4**,**a5**–**b4**,**b5**) IDC of scirrhous structure (low-aggressive breast cancer subtypes); (**a6**–**b6**) IDC of solid structure (highly-aggressive breast cancer subtype). Abbreviations: A—adipose, CT—connective tissue, ADH—atypical ductal hyperplasia, FA—fibroadenomatosis, DCIS—ductal carcinoma in situ, TS—tumor stroma, TC—cluster of tumor cells.

Figure 1 shows five types of representative CP-OCT and histological images: "adipose tissue with streaks of connective tissue" (a1–c1)/"fibroadenomatosis/fibroadenoma" (a2–c2)/"DCIS" (a3–c3)/invasive low-aggressive breast cancer of scirrhous structure (a4–c4)/invasive highly-aggressive breast cancer of solid structure (a5–c5).

Benign breast tissue states are characterized by high signal-penetration depth and uniformity of the signal attenuation along the inferior border in co- and cross-polarized structural OCT images (Figure 1). The hallmark of normal adipose (fatty) tissue is a "honeycomb" structure with low sparse scattering, while fibrous structures are characterized by high uniform scattering in co- and cross-polarized structural OCT images (Figure 1(a1–c1)). Fibroadenoma is characterized by a predominance of high-intensity OCT signal in co- and cross-polarization channels (Figure 1(a2–c2)) in comparison with normal breast tissue that has a dense structure due to the presence of large fibrous collagen fibers (Figure 1(c2)).

Cases suspicious for malignancy are characterized by general reduction in signal intensity and its penetration depth, irregular inferior border. All these features cause heterogeneity of the image. In particular, DCIS (Figure 1(c3)) is characterized by the presence of localized structures with low signal intensity and clear boundaries in the surrounding fibrous stroma with a high signal intensity in the cross-polarization channel (Figure 1(b3)). In co-polarization channels DCIS is not detectable (Figure 1(a3)).

In case of invasive breast cancer, the OCT signal in the cross-polarization channel for highly-aggressive (Figure 1(b5)) and less-aggressive (Figure 1(b4)) cancer subtypes is greatly different. IDC of solid structure (highly-aggressive) demonstrates a uniform low-level OCT signal, which is associated with an increased density of tumor cells and an almost total absence of anisotropic (fibrous) structures in this tumor subtype (Figure 1(b5)). For IDC of scirrhous structure (less-aggressive subtype), the heterogeneity of the OCT signal was observed: an alternating signal of medium and low intensity was revealed (Figure 1(b4)). On the corresponding histological images, there were clusters of tumor cells surrounded by connective tissue in a state of fibrosis and hyalinosis (Figure 1(c4)), which clearly leads to an increase in the level of OCT signal in these areas. It should be noted that in these cases, there is no pronounced contrast between low-aggressive (Figure 1(a4)) and highly-aggressive (Figure 1(a5)) breast cancer subtypes in the co-polarization channel.

Thus, in the structural OCT images, the most informative is the cross- polarization channel showing both regions with fairly high cross-polarization backscattering and (corresponding to the presence of connective tissue) and regions with a reduced cross-polarization signal (corresponding to the clusters of tumor cells), see Figure 1(b1–b5)). Therefore, in view of low informativity of the co-polarization images, only cross- polarization images were used for diagnostic accuracy analysis in this study.

The C-OCE image of the normal mammary gland (normal connective tissue and adipose tissue) is characterized by the lowest stiffness (Figure 2(a1)). However, fibroadenomatosis/fibroadenoma is characterized by a slight overall increase in stiffness (Figure 2(a2)) and the presence of well-localized areas with an increased elastic modulus in the regions of atypical ductal hyperplasia (ADH).

C-OCE images of malignancy demonstrate the appearance of regions with pronouncedly increased stiffness. Moreover, for IDC of solid structure (highly-aggressive), these areas occupy up to 90% of the entire image, which sharply distinguishes this breast cancer subtype (Figure 2(a6)). The ducts filled with tumor cells for DCIS are visualized as high-contrast zones with strongly increased stiffness (Figure 2(a3)) which coincide well with the histological image. The surrounding fibrous tissue is characterized by fairly low stiffness values (Figure 2(a3)). The OCE images of IDC of scirrhous structure demonstrate an increased stiffness in the regions of the clusters of tumor cells and significantly lower stiffness in the regions of the tumor stroma, causing multiple moderately contrast inclusions with elevated stiffness, which represents a feature of low-aggressive tumor subtype (Figure 2(a4–a5)).

In addition, it is necessary to mention that images of IDC of scirrhous structure and fibroadenoma may have similar patterns that may be challenging to differentiate for the reader. To solve this problem an additional criteria (Table 3) of "presence the numerous and less contrasting inclusions of increased stiffness" was included in cases of IDC (Figure 2(a4)) in contrast to single inclusions in cases of fibroadenoma (Figure 2(a2)) and DCIS (Figure 2(a3)).

### *3.2. Diagnostic Accuracy of CP-OCT and C-OCE Based on Visual Assessment of Images*

The results of the two tests, using the identified main and additional criteria, separately in CP-OCT images and C-OCE images demonstrate their great agreement among the readers. The concordance coefficient in the determination of tumorous or non-tumorous breast tissue in the analysis of CP-OCT images between two researchers was k = 0.68, between two post-graduate students k = 0.93, between the two surgeons k = 0.80. The concordance coefficient in the detection of tissue type in the analysis of C-OCE images between two researchers was k = 0.86, between two post-graduate students k = 0.93, between the two surgeons k = 0.82.

To demonstrate the variability of the test results, ROC-curves were presented for each reader (Figures 3 and 4). ROC-curves analysis confirmed that visual assessment of CP-OCT and C-OCE images has a high diagnostic value for differentiating non-tumorous and tumorous breast tissue (AUC values for all readers were 0.90–0.97 and 0.93–0.99, respectively) and also for distinguishing between low- and highly-aggressive invasive breast-cancer subtypes (AUC values for all readers were 0.84–0.90 and 0.80–1.00, respectively) (Figure 3c, Figure 4c). Slightly lower values were obtained for differentiation between non-invasive breast lession and invasive breast cancer (AUC values for all readers were 0.74–0.93 and 0.86–0.95, respectively) (Figure 3b, Figure 4b). The ROC-curves show that the best results were demonstrated by the researches experienced in optical imaging.

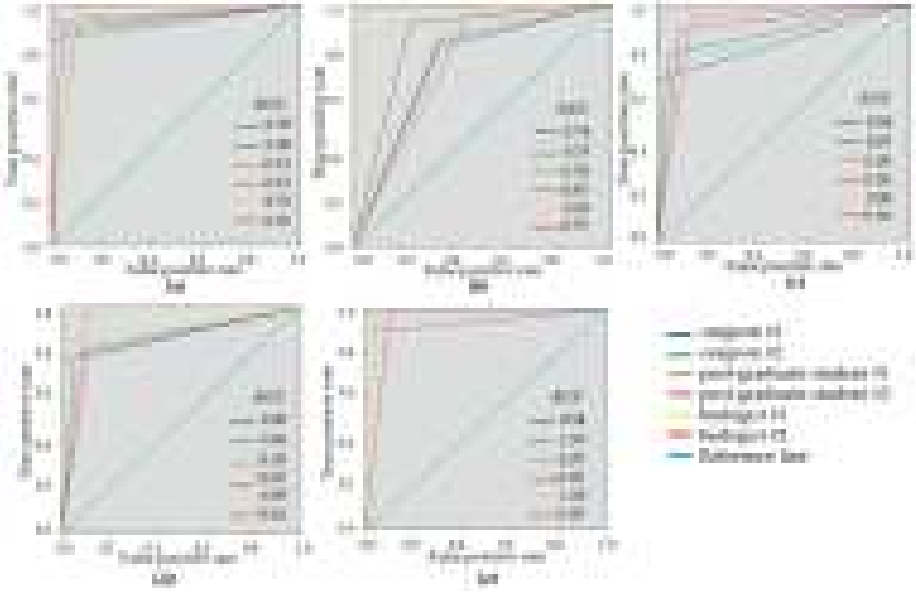

**Figure 3.** Receiver operating characteristic (ROC)-curves showing the results of visual assessment CP-OCT images for distinguishing non-tumorous breast tissue from tumor (**a**), DCIS from invasive breast cancer (**b**), low-aggressive invasive breast cancer from highly aggressive (**c**), non-tumorous breast tissue from low-aggressive breast cancer (**d**), non-tumorous breast tissue from highly aggressive breast cancer (**e**) for six "blinded" readers.

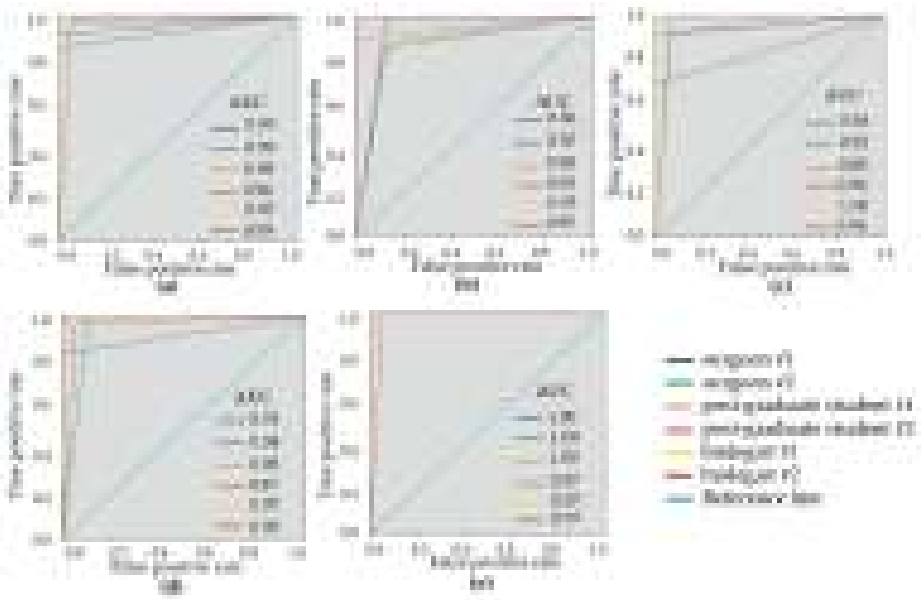

**Figure 4.** ROC-curves showing the results of visual assessment of C-OCE images for distinguishing non-tumorous from tumorous breast tissue (**a**), DCIS from invasive breast cancer (**b**), low-aggressive invasive breast cancer from highly-aggressive (**c**), non-tumorous breast tissue from low-aggressive breast cancer (**d**), non-tumorous breast tissue from highly-aggressive breast cancer (**e**) for six "blinded" readers.

The results of the blinded reader analysis are summarized in Table 4, showing the sensitivity, specificity and diagnostic accuracy. Each diagnostic index was averaged among all six readers. High diagnostic values were obtained for the differential diagnosis of all analyzed groups. The diagnostic accuracy of distinguishing non-tumorous tissue from tumor was 92.4 ± 2.3% for CP-OCT and 96.0 ± 3.3% for OCE, which determines the OCE method as more specific for detecting tumorous tissue.

For the first time, the diagnostic efficiency of CP-OCT and C-OCE methods for the differential diagnosis of non-invasive from invasive breast cancer was established (Se = 90.1 ± 5.7%, Sp = 70.6 ± 11.3%, Ac = 82.5 ± 7.1% and Se = 90.5 ± 5.3%, Sp = 92.0 ± 6.1%, Ac = 90.4 ± 2.7%, respectively). Furthermore, we demonstrated the possibility to differentiate invasive low-aggressive breast cancer subtypez with a favorable prognosis from highly-aggressive breast cancer subtypes with a poor prognosis for treatment and the course of the disease (Se-83.5 ± 10.5%, Sp-93.5 ± 6.0%, Ac-87.8 ± 6.5% and Se-87.3 ± 13.8 ± 6.5%, Sp-98.0 ± 3.1%, Ac-89.5 ± 10.0%, respectively). In both cases, it was demonstrated that C-OCE showed the best diagnostic indicators (Table 4).

Additionally, we performed a diagnostic analysis of the possibility to distinguish non-tumorous breast tissue from low- and highly-aggressive breast cancer subtypes. It has been shown that the diagnostic accuracy of the difference between non-tumorous breast tissue and a low-aggressive subtype of cancer is 88.1 ± 6.0% for CP-OCT and 95.7 ± 4.1% for C-OCE. The diagnostic accuracy of the difference between non-tumorous breast tissue and highly-aggressive cancer is 97.2 ± 2.8% for CP-OCT and for C-OCE—98.3 ± 2.2%.

Thus, we demonstrated the possibility to use CP-OCT and C-OCE methods for detecting different breast cancer subtypes on the resection margin which would minimize the risk of recurrence and reoperations.

**Table 4.** The results of diagnostic test for visual assessment of the CP-OCT and C-OCE images.

| | AUC (Range) | Sensitivity (Se), % | Specificity (Sp), % | Diagnostic Accuracy (Ac), % |
|---|---|---|---|---|
| **CP-OCT imaging** | | | | |
| Non-tumorous versus tumorous breast tissue | 0.90–0.97 | 92.0 ± 4.0 | 93.3 ± 6.0 | 92.4 ± 2.3 |
| DCIS versus invasive breast cancer | 0.74–0.93 | 90.1 ± 5.7 | 70.6 ± 11.3 | 82.5 ± 7.1 |
| Low-aggressive versus highly-aggressive breast cancer | 0.84–0.90 | 83.5 ± 10.5 | 93.5 ± 6.0 | 87.8 ± 6.5 |
| Non-tumorous breast tissue versus low-aggressive breast cancer | 0.85–0.95 | 85.1 ± 8.8 | 95.8 ± 4.9 | 88.1 ± 6.0 |
| Non-tumorous breast tissue versus highly-aggressive breast cancer | 0.94–1.00 | 98.1 ± 4.4 | 95.8 ± 4.9 | 97.2 ± 2.8 |
| **C-OCE imaging** | | | | |
| Non-tumorous versus tumorous breast tissue | 0.93–0.99 | 95.0 ± 5.1 | 97.5 ± 2.7 | 96.0 ± 3.3 |
| DCIS versus invasive breast cancer | 0.86–0.95 | 90.5 ± 5.3 | 92.0 ± 6.1 | 90.4 ± 2.7 |
| Low-aggressive versus highly-aggressive breast cancer | 0.80–1.00 | 87.3 ± 13.8 | 98.0 ± 3.1 | 89.5 ± 10.0 |
| Non-tumorous breast tissue versus low-aggressive breast cancer | 0.91–0.98 | 95.8 ± 6.5 | 95.8 ± 3.7 | 95.7 ± 4.1 |
| Non-tumorous breast tissue versus highly-aggressive breast cancer | 0.97–1.00 | 98.6 ± 3.2 | 97.5 ± 2.7 | 98.3 ± 2.2 |

### *3.3. Assessment of Human Breast Cancer Margins*

The tests performed in this study demonstrated that, in distinguishing the norm from low-aggressive cancers (and, moreover, highly aggressive ones), the analysis of both CP-OCT and C-OCE images the both methods enable high diagnostic accuracy. However, when searching for the transition between IDC of scirrhous structure and non-cancerous tissue, the C-OCE-based stiffness mapping (Figure 5c) visualizes the tumor margin much more clearly in comparison with the cross-polarization images (Figure 5b).

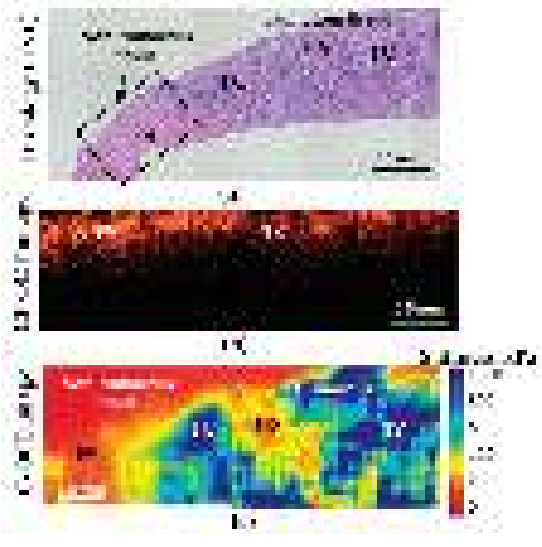

**Figure 5.** Histological image (**a**) demonstrating transition between non-tumorous (fibrous stroma—FS) and tumorous breast tissues (low-aggressive IDC of scirrhous structure); (**b**) is the corresponding CP-OCT image in the cross-polarization channel and (**c**) is the C-OCE images of the same area. HS denotes hyalinized stroma, and TC—clusters of tumor cells.

## 4. Discussion

The results presented here show the high diagnostic value and efficiency of CP-OCT and C-OCE methods for differential diagnosis of non-tumorous and tumorous breast tissue, with the further prospect of intraoperative determination of the "positive" margin of tumor resection during breast-conserving surgery in real time. In addition, the diagnostic efficiency of CP-OCT and C-OCE methods for differentiation between non-invasive and invasive breast cancers, as well as between invasive low-aggressive breast cancer subtype with a favorable prognosis (Luminal A, Luminal B (Her2/Neo-)) and highly aggressive breast cancer subtypes with a poor prognosis for course of the disease (Her2/Neo+, Non-luminal, TNC).

In previous studies, only standard visual imaging criteria, such as signal intensity and high/low stiffness, were used for differentiation between tumorous and non-tumorous breast tissues. In this study, additional analysis criteria were proposed, which made it possible to increase the diagnostic sensitivity and specificity, significantly reducing the number of erroneous diagnoses. We identified such additional analysis criteria as the presence of structures and the characteristics of signal attenuation in depth on cross-polarization images, as well as the presence of inclusions and mosaic structure on C-OCE images with visually feasible assessment of several stiffness grades.

Previous works have demonstrated that conventional, intensity-based OCT can provide differentiation between tumorous and non-tumorous breast tissues through both quantitative [18,61–63] and qualitative [32,61,63] assessment of the OCT signal. Several studies demonstrated that OCE has the high potential to delineate tumor in breast tissue based on elevated elasticity on a microscale [33,40,41,44]. A recent study [16] demonstrated the ability of structural OCT to identify positive margins in specimens from BCS. The qualitative assessment of OCT images showed the high diagnostic accuracy of structural OCT for distinguishing normal and cancerous tissue within the resection bed following wide local excision of the human breast: sensitivity of 91.7% and specificity of 92.1% [16]. Additionally, visual assessment of C-OCE images for evaluation of tumor margins in specimens excised during breast-conserving surgery also provides high sensitivity of (92.9%) and specificity (96.4%) [43].

Breast cancer is a highly heterogeneous disease, both morphologically and genetically. The surgical approach and the amount of resection depend on the subtype of breast cancer, which, as this study has shown, can be determined in rapid OCT-based tests, including the possibility of intraoperative use. The C-OCE and CP-OCT images provide additional contrast between tumor and normal tissue in comparison with structural OCT. C-OCE and CP-OCT analysis of excised tissue specimens can distinguish between normal and cancerous tissues by identifying the heterogeneous and disorganized connective tissue structures indicative for malignancy. We have demonstrated that differences in the microstructural features of cross-polarization and stiffness images enable differentiation between highly and low-aggressive breast cancer subtypes confirmed by histopathology. For this purpose, the main and additional criteria for assigning an image to a particular group were formulated, which are necessary for a more accurate differentiation of malignant conditions among themselves. For example, a uniform low-intensity in CP-OCT images and a uniform high level of stiffness in C-OCE images characterize tumor of a solid structure, while tumor tissue of a scirrhous structure in the immediate vicinity of non-tumorous breast tissue can also retain homogeneity, or it can lose it and may be represented by different levels of signal intensity and stiffness.

ROC curves were constructed as a measure of overall accuracy for each reader when non-cancerous tissue was distinguished from tumor by CP-OCT and C-OCE methods (Figure 3). In this case, C-OCE showed higher specificity (97.5 ± 2.7% vs. 93.3 ± 6.0%) and diagnostic accuracy (96.0 ± 3.3% vs. 92.4 ± 2.3%) compared to cross-polarized images. This fact may be caused by the difficulty in interpreting qualitative OCT criteria based on signal intensity by readers, in comparison with the criteria for interpreting quantitative OCE images that usually have more contrast and visually easier assessable differences. Overall, for differentiation between tumorous and non-tumorous tissues, the C-OCE method has proved to be more efficient.

Additionally, for more specific differentiation between non-invasive breast cancer and invasive breast cancer, the following diagnostic parameters were determined for CP-OCT and C-OCE methods: Se = 90.1 ± 5.7%, Sp = 70.6 ± 11.3%, Ac = 82.5 ± 7.1% and Se = 90.5 ± 5.3%, Sp = 92.0 ± 6.1%, Ac = 90.4 ± 2.7%, respectively. For distinguishing between invasive low-aggressive and highly-aggressive breast cancer subtypes, the CP-OCT and C-OCE gave the following results: Se = 83.5 ± 10.5%, Sp = 93.5 ± 6.0%, Ac = 87.8 ± 6.5% and Se = 87.3 ± 13.8 ± 6.5%, Sp = 98.0 ± 3.1%, Ac = 89.5 ± 10.0%, respectively. Therefore, in both cases, C-OCE showed better diagnostic indicators (Table 4).

The diagnostic accuracy of the difference between non-tumorous breast tissue and low-aggressive breast cancer for CP-OCT and C-OCE was found to be fairly high, 88.1 ± 6.0% and 95.7 ± 4.1%, respectively. Even higher was the Ac of CP-OCT and C-OCE for the difference between non-tumorous breast tissue and highly-aggressive breast cancer (97.2 ± 2.8% and 98.3 ± 2.2%, respectively).

Accurate determining of the boundaries of tumor resection is more feasible for tumors of a solid structure in comparison with tumors of scirrhous structure that may resemble fibroadenomas in OCT-based images. However, the performed targeted histological examination has given a clue for better understanding of the causes of stiffness increase or decrease and made it possible to define additional criteria that improved the diagnostic accuracy of C-OCE for various breast cancer subtypes detection, including non-invasive and low-aggressive tumors.

Thus, the formulated additional (clarifying) criteria for visual assessment of CP-OCT and C-OCE images provided a higher diagnostic accuracy in differentiation between tumorous and non-tumorous breast tissues with various grades of aggressiveness. In the future, this will increase the value of these OCT-based methods in detecting the boundaries of tumor resection during BCS.

## 5. Conclusions

Both CP-OCT and C-OCE data may be helpful to a surgeon–oncologist for more accurate detection of a "clean" resection margin during breast-conserving surgery. The test based on assessment of C-OCE images has shown higher diagnostic accuracy (96%) and sensitivity (95%) in comparison with CP-OCT images (Se—92%, Ac—92.4%) for breast cancer detection. Furthermore, the preformed study demonstrated high potential of CP-OCT and C-OCE for differentiating particular molecular-biological and morphological subtypes of breast cancer with assessment of the tumor aggressiveness, which is important for subsequent treatment selection.

**Author Contributions:** Conceptualization, N.D.G. and M.A.S.; images analysis, M.A.S., E.B.K., K.A.A., A.A.P., K.S.Y. and D.A.V.; C-OCE methodology and software, A.L.M., L.A.M., A.A.S. and V.Y.Z.; histological analysis, S.S.K., D.A.V.; data curation, E.V.G., E.B.K.; writing—original draft preparation, E.V.G.; writing—review and editing, N.D.G., A.Y.V. and V.Y.Z.; visualization, E.V.G.; supervision, N.D.G. All authors have read and agreed to the published version of the manuscript.

**Funding:** The study was funded by the Russian Science Foundation under grant No. 18-75-10068. The development of software for plotting OCE scans was supported by RFBR grant No. 19-32-90110.

**Conflicts of Interest:** The authors declare no conflict of interest. The funders/sponsors had no role in the design of the study; in the collection, analyses, or interpretation of data; in the writing of the manuscript, or in the decision to publish the results.

## References

1. Esbona, K.; Li, Z.; Wilke, L.G. Intraoperative imprint cytology and frozen section pathology for margin assessment in breast conservation surgery: A systematic review. *Ann. Surg. Oncol.* **2012**, *19*, 3236–3245. [CrossRef] [PubMed]
2. Decker, M.R.; Trentham-Dietz, A.; Loconte, N.K.; Neuman, H.B.; Smith, M.A.; Punglia, R.S.; Greenberg, C.C.; Wilke, L.G. The Role of Intraoperative Pathologic Assessment in the Surgical Management of Ductal Carcinoma In Situ. *Ann. Surg. Oncol.* **2016**, *23*, 2788–2794. [CrossRef] [PubMed]
3. Harness, J.K.; Giuliano, A.E.; Pockaj, B.A.; Downs-Kelly, E. Margins: A status report from the Annual Meeting of the American Society of Breast Surgeons. *Ann Surg Oncol Ann. Surg. Oncol.* **2014**, *21*, 3192–3197. [CrossRef] [PubMed]

4. Lamberts, L.E.; Koch, M.; de Jong, J.S.; Adams, A.L.L.; Glatz, J.; Kranendonk, M.E.G.; van Scheltinga, A.G.T.T.; Jansen, L.; de Vries, J.; Lub-de Hooge, M.N.; et al. Tumor-Specific Uptake of Fluorescent Bevacizumab-IRDye800CW Microdosing in Patients with Primary Breast Cancer: A Phase I Feasibility Study. *Clin. Cancer Res.* **2017**, *23*, 2730–2741. [CrossRef]
5. Tummers, Q.R.; Verbeek, F.P.; Schaafsma, B.E.; Boonstra, M.C.; van der Vorst, J.R.; Liefers, G.J.; van de Velde, C.J.; Frangioni, J.V.; Vahrmeijer, A.L. Real-time intraoperative detection of breast cancer using near-infrared fluorescence imaging and Methylene Blue. *Eur. J. Surg. Oncol.* **2014**, *40*, 850–858. [CrossRef]
6. Wojcinski, S.; Farrokh, A.; Weber, S.; Thomas, A.; Fischer, T.; Slowinski, T.; Schmidt, W.; Degenhardt, F. Multicenter study of ultrasound real-time tissue elastography in 779 cases for the assessment of breast lesions: Improved diagnostic performance by combining the BI-RADS®-US classification system with sonoelastography. *Ultraschall. Med.* **2010**, *31*, 484–491. [CrossRef]
7. Dua, S.M.; Gray, R.J.; Keshtgar, M. Strategies for localisation of impalpable breast lesions. *Breast* **2011**, *20*, 246–253. [CrossRef]
8. Xu, H.; Varghese, T.; Jiang, J.; Zagzebski, J.A. In vivo classification of breast masses using features derived from axial-strain and axial-shear images. *Ultrason. Imaging* **2012**, *4*, 222–236. [CrossRef]
9. Wang, J.; Xu, Y.; Boppart, S.A. Review of optical coherence tomography in oncology. *J. Biomed. Opt.* **2017**, *22*, 1–23. [CrossRef]
10. Curatolo, A.; McLaughlin, R.A.; Quirk, B.C.; Kirk, R.W.; Bourke, A.G.; Wood, B.A.; Robbins, P.D.; Saunders, C.M.; Sampson, D.D. Ultrasound-guided optical coherence tomography needle probe for the assessment of breast cancer tumor margins. *AJR Am. J. Roentgenol.* **2012**, *199*, W520–W522. [CrossRef]
11. Kennedy, K.M.; McLaughlin, R.A.; Kennedy, B.F.; Tien, A.; Latham, B.; Saunders, C.M.; Sampson, D.D. Needle optical coherence elastography for the measurement of microscale mechanical contrast deep within human breast tissues. *J. Biomed. Opt.* **2013**, *18*, 121510. [CrossRef] [PubMed]
12. Nguyen, F.T.; Zysk, A.M.; Chaney, E.J.; Kotynek, J.G.; Oliphant, U.J.; Bellafiore, F.J.; Rowland, K.M.; Johnson, P.A.; Boppart, S.A. Intraoperative evaluation of breast tumor margins with optical coherence tomography. *Cancer Res.* **2009**, *69*, 8790–8796. [CrossRef] [PubMed]
13. Ha, R.; Friedlander, L.C.; Hibshoosh, H.; Hendon, C.; Feldman, S.; Ahn, S.; Schmidt, H.; Akens, M.K.; Fitzmaurice, M.; Wilson, B.C.; et al. Optical Coherence Tomography: A Novel Imaging Method for Post-lumpectomy Breast Margin Assessment-A Multi-reader Study. *Acad. Radiol.* **2018**, *25*, 279–287. [CrossRef] [PubMed]
14. Schmidt, H.; Connolly, C.; Jaffer, S.; Oza, T.; Weltz, C.R.; Port, E.R.; Corben, A. Evaluation of surgically excised breast tissue microstructure using wide-field optical coherence tomography. *Breast J.* **2020**, *26*, 917–923. [CrossRef] [PubMed]
15. Savastru, D.; Chang, E.W.; Miclos, S.; Pitman, M.B.; Patel, A.; Iftimia, N. Detection of breast surgical margins with optical coherence tomography imaging: A concept evaluation study. *J. Biomed. Opt.* **2014**, *19*, 056001. [CrossRef]
16. Erickson-Bhatt, S.J.; Nolan, R.M.; Shemonski, N.D.; Adie, S.G.; Putney, J.; Darga, D.; McCormick, D.T.; Cittadine, A.J.; Zysk, A.M.; Marjanovic, M.; et al. Real-time Imaging of the Resection Bed Using a Handheld Probe to Reduce Incidence of Microscopic Positive Margins in Cancer Surgery. *Cancer Res.* **2015**, *75*, 3706–3712. [CrossRef]
17. Zysk, A.M.; Chen, K.; Gabrielson, E.; Tafra, L.; May Gonzalez, E.A.; Canner, J.K.; Schneider, E.B.; Cittadine, A.J.; Scott Carney, P.; Boppart, S.A.; et al. Intraoperative Assessment of Final Margins with a Handheld Optical Imaging Probe During Breast-Conserving Surgery May Reduce the Reoperation Rate: Results of a Multicenter Study. *Ann. Surg. Oncol.* **2015**, *22*, 3356–3362. [CrossRef]
18. Zhou, C.; Cohen, D.W.; Wang, Y.; Lee, H.C.; Mondelblatt, A.E.; Tsai, T.H.; Aguirre, A.D.; Fujimoto, J.G.; Connolly, J.L. Integrated optical coherence tomography and microscopy for ex vivo multiscale evaluation of human breast tissues. *Cancer Res.* **2010**, *70*, 10071–10079. [CrossRef]
19. de Boer, J.F.; Hitzenberger, C.K.; Yasuno, Y. Polarization sensitive optical coherence tomography—A review [Invited]. *Biomed. Opt. Express* **2017**, *8*, 1838–1873. [CrossRef]
20. Wang, J.; Xu, Y.; Mesa, K.J.; South, F.A.; Chaney, E.J.; Spillman, D.R.; Barkalifa, R., Jr.; Marjanovic, M.; Carney, P.S.; Higham, A.M.; et al. Complementary use of polarization-sensitive and standard OCT metrics for enhanced intraoperative differentiation of breast cancer. *Biomed. Opt. Express* **2018**, *9*, 6519–6528. [CrossRef]

21. South, F.A.; Chaney, E.J.; Marjanovic, M.; Adie, S.G.; Boppart, S.A. Differentiation of ex vivo human breast tissue using polarization-sensitive optical coherence tomography. *Biomed. Opt. Express* **2014**, *5*, 3417–3426. [CrossRef]
22. Provenzano, P.P.; Eliceiri, K.W.; Campbell, J.M.; Inman, D.R.; White, J.G.; Keely, P.J. Collagen reorganization at the tumor-stromal interface facilitates local invasion. *BMC Med.* **2006**, *4*, 1741–7015. [CrossRef]
23. Patel, R.; Khan, A.; Quinlan, R.; Yaroslavsky, A.N. Polarization-sensitive multimodal imaging for detecting breast cancer. *Cancer Res.* **2014**, *74*, 4685–4693. [CrossRef] [PubMed]
24. Gelikonov, V.M.; Romashov, V.N.; Shabanov, D.V.; Ksenofontov, S.Y.; Terpelov, D.A.; Shilyagin, P.A.; Gelikonov, G.V.; Vitkin, I.A. Cross-polarization optical coherence tomography with active maintenance of the circular polarization of a sounding wave in a common path system. *Radiophys. Quantum Electron.* **2018**, *60*, 897–911. [CrossRef]
25. Gubarkova, E.V.; Sovetsky, A.A.; Zaitsev, V.Y.; Matveyev, A.L.; Vorontsov, D.A.; Sirotkina, M.A.; Matveev, L.A.; Plekhanov, A.A.; Pavlova, N.P.; Kuznetsov, S.S.; et al. OCT-elastography-based optical biopsy for breast cancer delineation and express assessment of morphological/molecular subtypes. *Biomed. Opt. Express* **2019**, *10*, 2244–2263. [CrossRef] [PubMed]
26. Yashin, K.S.; Kiseleva, E.B.; Gubarkova, E.V.; Moiseev, A.A.; Kuznetsov, S.S.; Shilyagin, P.A.; Gelikonov, G.V.; Medyanik, I.A.; Kravets, L.Y.; Potapov, A.A.; et al. Cross-Polarization Optical Coherence Tomography for Brain Tumor Imaging. *Front. Oncol.* **2019**, *9*, 201. [CrossRef] [PubMed]
27. Yashin, K.S.; Kiseleva, E.B.; Moiseev, A.A.; Kuznetsov, S.S.; Timofeeva, L.B.; Pavlova, N.P.; Gelikonov, G.V.; Medyanik, I.A.; Kravets, L.Y.; Zagaynova, E.V.; et al. Quantitative nontumorous and tumorous human brain tissue assessment using microstructural co- and cross-polarized optical coherence tomography. *Sci. Rep.* **2019**, *9*, 2024. [CrossRef] [PubMed]
28. Kiseleva, E.; Kirillin, M.; Feldchtein, F.; Vitkin, A.; Sergeeva, E.; Zagaynova, E.; Streltzova, O.; Shakhov, B.; Gubarkova, E.; Gladkova, N. Differential diagnosis of human bladder mucosa pathologies in vivo with cross-polarization optical coherence tomography. *Biomed. Opt. Express* **2015**, *6*, 1464–1476. [CrossRef]
29. Gladkova, N.; Kiseleva, E.; Streltsova, O.; Prodanets, N.; Snopova, L.; Karabut, M.; Gubarkova, E.; Zagaynova, E. Combined use of fluorescence cystoscopy and cross-polarization OCT for diagnosis of bladder cancer and correlation with immunohistochemical markers. *J. Biophotonics* **2013**, *6*, 687–698. [CrossRef]
30. Gladkova, N.; Streltsova, O.; Zagaynova, E.; Kiseleva, E.; Gelikonov, V.; Gelikonov, G.; Karabut, M.; Yunusova, K.; Evdokimova, O. Cross-polarization optical coherence tomography for early bladder-cancer detection: Statistical study. *J. Biophotonics* **2011**, *4*, 519–532. [CrossRef]
31. Gladkova, N.; Kiseleva, E.; Robakidze, N.; Balalaeva, I.; Karabut, M.; Gubarkova, E.; Feldchtein, F. Evaluation of oral mucosa collagen condition with cross-polarization optical coherence tomography. *J. Biophotonics* **2013**, *6*, 321–329. [CrossRef] [PubMed]
32. Foo, K.Y.; Chin, L.; Zilkens, R.; Lakhiani, D.D.; Fang, Q.; Sanderson, R.; Dessauvagie, B.F.; Latham, B.; McLaren, S.; Saunders, C.M.; et al. Three-dimensional mapping of the attenuation coefficient in optical coherence tomography to enhance breast tissue microarchitecture contrast. *J. Biophotonics* **2020**, *13*, e201960201. [CrossRef]
33. Gubarkova, E.V.; Moiseev, A.A.; Kiseleva, E.B.; Vorontsov, D.A.; Kuznetsov, S.S.; Vorontsov, A.Y.; Gelikonov, G.V.; Sirotkina, M.A.; Gladkova, N.D. Tissue optical properties estimation from cross-polarization OCT data for breast cancer margin assessment. *Laser Phys. Lett.* **2020**, *17*, 075602. [CrossRef]
34. Kennedy, K.M.; Chin, L.; McLaughlin, R.A.; Latham, B.; Saunders, C.M.; Sampson, D.D.; Kennedy, B.F. Quantitative micro-elastography: Imaging of tissue elasticity using compression optical coherence elastography. *Sci. Rep.* **2015**, *5*, 15538. [CrossRef] [PubMed]
35. Kennedy, B.F.; Wijesinghe, P.; Sampson, D.D. The emergence of optical elastography in biomedicine. *Nat. Photonics* **2017**, *11*, 215–221. [CrossRef]
36. Larin, K.V.; Sampson, D.D. Optical coherence elastography—OCT at work in tissue biomechanics [Invited]. *Biomed. Opt. Express* **2017**, *8*, 1172–1202. [CrossRef]
37. Zaitsev, V.Y.; Matveyev, A.L.; Matveev, L.A.; Sovetsky, A.A.; Hepburn, M.S.; Mowla, A.; Kennedy, B.F. Strain and elasticity imaging in compression optical coherence elastography: The two-decade perspective and recent advances. *J. Biophotonics* **2020**, e202000257. [CrossRef] [PubMed]

38. Sirotkina, M.A.; Gubarkova, E.V.; Plekhanov, A.A.; Sovetsky, A.A.; Elagin, V.V.; Matveyev, A.L.; Matveev, L.A.; Kuznetsov, S.S.; Zagaynova, E.V.; Gladkova, N.D.; et al. In vivo assessment of functional and morphological alterations in tumors under treatment using OCT-angiography combined with OCT-elastography. *Biomed. Opt. Express* **2020**, *11*, 1365–1382. [CrossRef]
39. Plekhanov, A.A.; Sirotkina, M.A.; Sovetsky, A.A.; Gubarkova, E.V.; Kuznetsov, S.S.; Matveyev, A.L.; Matveev, L.A.; Zagaynova, E.V.; Gladkova, N.D.; Zaitsev, V.Y. Histological validation of in vivo assessment of cancer tissue inhomogeneity and automated morphological segmentation enabled by Optical Coherence Elastography. *Sci. Rep.* **2020**, *10*, 11781. [CrossRef]
40. Kennedy, B.F.; McLaughlin, R.A.; Kennedy, K.M.; Chin, L.; Wijesinghe, P.; Curatolo, A.; Tien, A.; Ronald, M.; Latham, B.; Saunders, C.M.; et al. Investigation of Optical Coherence Microelastography as a Method to Visualize Cancers in Human Breast Tissue. *Cancer Res.* **2015**, *75*, 3236–3245. [CrossRef]
41. Allen, W.M.; Foo, K.Y.; Zilkens, R.; Kennedy, K.M.; Fang, Q.; Chin, L.; Dessauvagie, B.F.; Latham, B.; Saunders, C.M.; Kennedy, B.F. Clinical feasibility of optical coherence micro-elastography for imaging tumor margins in breast-conserving surgery. *Biomed. Opt. Express* **2018**, *9*, 6331–6349. [CrossRef] [PubMed]
42. Zaitsev, V.Y.; Matveyev, A.L.; Matveev, L.A.; Gubarkova, E.V.; Sovetsky, A.A.; Sirotkina, M.A.; Gelikonov, G.V.; Zagaynova, E.V.; Gladkova, N.D.; Vitkin, A. Practical obstacles and their mitigation strategies in compressional optical coherence elastography of biological tissues *J. Innovative Opt. Health Sci.* **2017**, *10*, 1742006. [CrossRef]
43. Kennedy, K.M.; Zilkens, R.; Allen, W.M.; Foo, K.Y.; Fang, Q.; Chin, L.; Sanderson, R.W.; Anstie, J.; Wijesinghe, P.; Curatolo, A.; et al. Diagnostic Accuracy of Quantitative Micro-Elastography for Margin Assessment in Breast-Conserving Surgery. *Cancer Res.* **2020**, *80*, 1773–1783. [CrossRef] [PubMed]
44. Allen, W.M.; Kennedy, K.M.; Fang, Q.; Chin, L.; Curatolo, A.; Watts, L.; Zilkens, R.; Chin, S.L.; Dessauvagie, B.F.; Latham, B.; et al. Wide-field quantitative micro-elastography of human breast tissue. *Biomed. Opt. Express.* **2018**, *9*, 1082–1096. [CrossRef]
45. Aleskandarany, M.A.; Vandenberghe, M.E.; Marchiò, C.; Ellis, I.O.; Sapino, A.; Rakha, E.A. Tumour Heterogeneity of Breast Cancer: From Morphology to Personalised Medicine. *Pathobiology* **2018**, *85*, 23–34. [CrossRef]
46. Iwao, K.; Matoba, R.; Ueno, N.; Ando, A.; Miyoshi, Y.; Matsubara, K.; Noguchi, S.; Kato, K. Molecular classification of primary breast tumors possessing distinct prognostic properties. *Hum. Mol. Genet.* **2002**, *11*, 199–206. [CrossRef]
47. Lowery, A.J.; Kell, M.R.; Glynn, R.W.; Kerin, M.J.; Sweeney, K.J. Locoregional recurrence after breast cancer surgery: A systematic review by receptor phenotype. *Breast Cancer Res. Treat.* **2012**, *133*, 831–841. [CrossRef]
48. Cancello, G.; Maisonneuve, P.; Rotmensz, N.; Viale, G.; Mastropasqua, M.G.; Pruneri, G.; Montagna, E.; Dellapasqua, S.; Iorfida, M.; Cardillo, A.; et al. Prognosis in women with small (T1mic,T1a,T1b) node-negative operable breast cancer by immunohistochemically selected subtypes. *Breast Cancer Res. Treat.* **2011**, *127*, 713–720. [CrossRef]
49. Houssami, N.; Macaskill, P.; Marinovich, M.L.; Morrow, M. The association of surgical margins and local recurrence in women with early-stage invasive breast cancer treated with breast-conserving therapy: A meta-analysis. *Ann. Surg. Oncol.* **2014**, *21*, 717–730. [CrossRef]
50. Moiseev, A.; Ksenofontov, S.; Sirotkina, M.; Kiseleva, E.; Gorozhantseva, M.; Shakhova, N.; Matveev, L.; Zaitsev, V.; Matveyev, A.; Zagaynova, E.; et al. Optical coherence tomography-based angiography device with real-time angiography B-scans visualization and hand-held probe for everyday clinical use. *J. Biophotonics* **2018**, *11*, e201700292. [CrossRef]
51. Zaitsev, V.Y.; Matveyev, A.L.; Matveev, L.A.; Gelikonov, G.V.; Sovetsky, A.A.; Vitkin, A. Optimized phase gradient measurements and phase-amplitude interplay in optical coherence elastography. *J. Biomed. Opt.* **2016**, *21*, 116005. [CrossRef] [PubMed]
52. Zaitsev, V.Y.; Matveyev, A.L.; Matveev, L.A.; Gelikonov, G.V.; Gubarkova, E.V.; Gladkova, N.D.; Vitkin, A. Hybrid method of strain estimation in optical coherence elastography using combined sub-wavelength phase measurements and supra-pixel displacement tracking. *J. Biophotonics* **2016**, *9*, 499–509. [CrossRef] [PubMed]
53. Matveyev, A.L.; Matveev, L.A.; Sovetsky, A.A.; Gelikonov, G.V.; Moiseev, A.A.; Zaitsev, V.Y. Vector method for strain estimation in phase-sensitive optical coherence elastography. *Laser Phys. Lett.* **2018**, *15*, 065603. [CrossRef]

54. Sovetsky, A.A.; Matveyev, A.L.; Matveev, L.A.; Shabanov, D.V.; Zaitsev, V.Y. Manually-operated compressional optical coherence elastography with effective aperiodic averaging: Demonstrations for corneal and cartilaginous tissues. *Laser Phys. Lett.* **2018**, *15*, 85602. [CrossRef]
55. Sovetsky, A.A.; Matveyev, A.L.; Matveev, L.A.; Gubarkova, E.V.; Plekhanov, A.A.; Sirotkina, M.A.; Gladkova, N.D.; Zaitsev, V.Y. Full-optical method of local stress standardization to exclude nonlinearity-related ambiguity of elasticity estimation in compressional optical coherence elastography. *Laser Phys. Lett.* **2020**, *17*, 065601. [CrossRef]
56. Sovetsky, A.A.; Matveev, L.A.; Gubarkova, E.V.; Matveyev, A.L.; Gladkova, N.D.; Zaitsev, V.Y. Characterization of elastic nonlinear properties of the tissues using compressional optical coherence elastography. *Proc. SPIE* **2020**, *11359*, 113590H. [CrossRef]
57. Zaitsev, V.Y.; Matveyev, A.L.; Matveev, L.A.; Gelikonov, G.V.; Omelchenko, A.I.; Shabanov, D.V.; Baum, O.I.; Svistushkin, V.M.; Sobol, E.N. Optical coherence tomography for visualizing transient strains and measuring large deformations in laser-induced tissue reshaping. *Laser Phys. Lett.* **2016**, *13*, 115603. [CrossRef]
58. Zaitsev, V.Y.; Matveyev, A.L.; Matveev, L.A.; Gelikonov, G.V.; Omelchenko, A.I.; Baum, O.I.; Avetisov, S.E.; Bolshunov, A.V.; Siplivy, V.I.; Shabanov, D.V.; et al. Optical coherence elastography for strain dynamics measurements in laser correction of cornea shape. *J. Biophotonics* **2017**, *10*, 1450–1463. [CrossRef]
59. Feuerman, M.; Miller, A.R. Relationships between statistical measures of agreement: Sensitivity, specificity and kappa. *J. Eval. Clin. Pract.* **2008**, *14*, 930–933. [CrossRef]
60. Viera, A.J.; Garrett, J.M. Understanding interobserver agreement: The kappa statistic. *Fam. Med.* **2005**, *37*, 360–363.
61. Yao, X.; Gan, Y.; Chang, E.; Hibshoosh, H.; Feldman, S.; Hendon, C. Visualization and tissue classification of human breast cancer images using ultrahigh-resolution OCT. *Lasers Surg. Med.* **2017**, *49*, 258–269. [CrossRef] [PubMed]
62. Assayag, O.; Antoine, M.; Sigal-Zafrani, B.; Riben, M.; Harms, F.; Burcheri, A.; Grieve, K.; Dalimier, E.; Le Conte de Poly, B.; Boccara, C. Large field, high resolution full-field optical coherence tomography: A pre-clinical study of human breast tissue and cancer assessment. *Technol. Cancer Res. Treat.* **2014**, *13*, 455–468. [CrossRef] [PubMed]
63. Zysk, A.M.; Boppart, S.A. Computational methods for analysis of human breast tumor tissue in optical coherence tomography images. *J. Biomed. Opt.* **2006**, *11*, 054015. [CrossRef] [PubMed]